Quantum and Coherence Enhanced Imaging

Osian Wolley

Submitted in fulfilment of the requirements for the

Degree of Doctor of Philosophy

School of Physics and Astronomy

College of Science and Engineering

University of Glasgow

July 2025

Contents

Acknowledgements

Completion of this thesis would not have been possible without many people who I have met over my time in Glasgow, and that I would like to thank. First of all, I would like to thank my supervisor, Miles Padgett, for his enthusiasm, guidance and support during the course of my PhD studies. One time, whilst struggling to recall an equation, Miles told me he doesn't want me to remember, he wants me to *understand*. It is this approach which has helped me learn so much over my time in Glasgow. Next is my second supervisor Dr Simon (Peter) Mekhail. Peter has been maybe a slightly unconventional second supervisor, for example reading over my second-year progression review between sets of bench presses in the gym, but has been a great friend and mentor, and is one of the best physicists I have met.

Next I would like to thank others within the Optics Group who I worked with over the years who became good friends. Firstly Tom, who, whil streluctant to mentor new PhD students, was actually very good at it, and taught me everything I know about alignment of optics and imaging with downconversion sources. I am lucky, however, not to have picked up his attitude towards IT equipment. Next, Graham, whose knowledge, electronic wizardry, lab management and healthy cynicism keep the Optics Group running. Robert, for being a great friend and sharing my love of a certain Sauchiehall Street establishment. Thank you to Grant for putting up with me, providing a lot of laughs and being a good friend over long days in the lab. Hao-Wei for introducing me to Taiwanese vodka and basketball - I hope the climbing is going well! Mark, for reliably keeping me company on late evenings and weekends in the lab. Sara, for providing distracting chats and Italian treats. Akhil, for being a great climbing partner and friend. Kieran for his love of the pub. Joe for the Stoke-on-Trent jokes. There are too many more to mention - but thank you all for the guidance, support and entertainment you provided. You made for a very fun PhD.

Also I would like to thank everyone on the team at QuantIC, for supporting me throughout the PhD and providing lots of opportunities to travel to conferences and meet other academics within the field. I always enjoyed the many QuantIC events and I wish everyone the best of luck for the upcoming hub.

A big thank you also to all the friends who I made over the four years I spent in Glasgow, especially my flatmates when I first moved up. Moving during Covid could have been challenging, however the fun we had in our flat helped me settle in to the PhD and Glasgow. Also a thank you to all my friends down in England, for visiting and still staying as close despite only seeing me a handful of times a year.

Thank you to my family as well of course, for letting me not get a real job and who are a constant source of support in my life, even when I move far away. Mum and Dad, you can now tell people I am a doctor, even if it's not the medical kind.

Finally, thank you to Keerthi. I don't need to say any more than meeting you was the best thing about this PhD.

Declaration of Authorship

I hereby declare that this thesis is the result of my own work, except where explicit reference is made to the work of others, and has not been presented in any previous application for a degree at this or any other institution.

Osian Wolley

Publications

During the course of my PhD studies a number of peer-reviewed papers were co-authored with colleagues in the Optics group at the University of Glasgow under the supervision of Miles J. Padgett and Simon P. Mekhail.

1. T. Gregory, P.-A. Moreau, S. Mekhail, O. Wolley, and M.J. Padgett, "Noise rejection through an improved quantum illumination protocol". *Scientific Reports* **11** (1), 21841, (2021).

2. O. Wolley, T. Gregory, S. Beer, T. Higuchi, and M.J. Padgett, "Quantum imaging with a photon counting camera". *Scientific Reports* **12** (1), 8286, (2022).

3. O. Wolley, P.-A. Moreau, S. Mekhail, T. Gregory, G. Gibson, G. Leuchs, and M.J. Padgett, "Near single photon imaging in the shortwave infrared using homodyne detection". *Proceedings of the National Academy of Sciences* **120**, 10, (2023).

4. K. Roberts, O. Wolley, T. Gregory and M.J. Padgett "A comparison between the measurement of quantum spatial correlations using qCMOS photon-number resolving and Electron Multiplying CCD camera technologies" *Scientific Reports* **14** (1), 14687, (2024).

5. E. Pearce, O. Wolley, S.P. Mekhail, T. Gregory, N.R. Gemmell, R.F. Oulton, A.S. Clark, C.C. Phillips and M.J. Padgett, "Single-frame transmission and phase imaging using off-axis holography with undetected photons" *Scientific Reports* **14** (1), 16008 (2024).

6. H.-W. Hu, S.P. Mekhail, R. Archibald, O. Wolley and M.J. Padgett, "The speckled output of a multi-mode optical fibre and sensitivity to fibre perturbations" *Optics Continuum* **3** (9), 1602-1611 (2024).

7. O. Wolley, T. Gregory, S.P. Mekhail, R. Archibald, M.J. Padgett, "Low photon-number stand-off speckle holography at kHz frame rates" *Optics Continuum* **3** (9), 1732-1740 (2024).

Conference Proceedings and Presentations

1. O. Wolley, P.-A. Moreau, S. Mekhail, T. Gregory, G. Leuchs, and M.J. Padgett, "Imaging at the camera noise floor". Presented at CLEO 2022.

2. O. Wolley, P.-A. Moreau, S. Mekhail, T. Gregory, G. Leuchs, and M.J. Padgett, "Enabling single photon imaging with digital holography". Presented at Photonex 2023.

3. O. Wolley, P.-A. Moreau, S. Mekhail, T. Gregory, G. Leuchs, and M.J. Padgett, "Enabling single photon imaging at kHz frame rates with digital holography". Presented at Photonics West 2024.

Chapter 1

Introduction

Light is probably our most powerful source of understanding the physical world. As sight has evolved to be our primary sense, we rely on light to transmit information from our environment, and process this as an image formed on our retinas. Light conveniently also turns out to be an ideal medium for the transfer of information. It has comparatively low interactivity with its physical environment, meaning that information transfer over long distances is possible with little loss. The wavelike nature of light also offers many advantages; the degrees of freedom provided by an oscillating field allow for information to be encoded both in time and spatially. Light has a broad frequency spectrum, with differing interaction properties allowing for the probing of different media and encoding of information at different frequencies. Furthermore, the oscillation of the field leads to light having phase, which can be measured to provide information on the optical path length of the light. As such, it is an exceptionally powerful tool for the gain and transfer of information.

It is unsurprising, then, that imaging has become crucial to measurement science. With applications from astronomy, biological imaging, and industrial control processes, the ability to accurately image an object as close to the ground truth as possible is key. One of the barriers to accurate imaging is noise in the imaging signal. All detector technology has a certain amount of noise characteristic to the readout circuitry on the sensor. This is known as readout noise. When imaging with an illumination flux within or below the level of the readout noise on the sensor, images become grainy and contrast is lost. This can make it difficult or impossible

to distinguish the object and its features. Environmental or background light can also have a similar effect, where the signal can become lost in the excess light. Furthermore, even when sensitive detector technology is available, noise from the fundamental nature of light itself may limit imaging precision.

The typical response to this problem is to simply increase the illumination flux, such that the image signal is increased over the noise. However, in some cases, this is not always possible. For example in some biological imaging applications, illuminating a live sample with a high probe power may alter cell processes and a high probe power can lead to cell death [1–3]. Also, in absorption measurements, increasing the probe power can lead to saturation of the sample [4]. Other applications demand eye-safe illumination at long ranges, such as light detection and ranging (LIDAR) for autonomous vehicles or covert imaging applications [5]. Further, some applications require imaging through a scattering media, resulting in vastly reduced photon flux at the detector [6, 7]. There are also applications requiring high-speed video cameras, where operating at kHz frame rates demands short exposure times returning low photon counts [8]. In these cases, it is not possible to simply increase illumination flux, and other techniques to increase the sensitivity of detection must be employed.

One of the themes of research within the Optics Group at the University of Glasgow has been the question ‘How many photons does it take to form an image?’, in an effort to find the minimum number of photons possible to transmit image information [9]. The ability to suppress sources of noise is key to this question; clearly more noise will require more detected photons to transmit image information. Much research has been done within the group and elsewhere to develop imaging schemes that are capable of suppressing the different sources of noise in imaging. The work presented here is a continuation of that research, with three different approaches investigated over the course of this thesis. The first of which is a quantum imaging scheme which uses the quantum correlations of photon pairs produced from a non-linear optic crystal, and builds on the research of colleagues and previous members of the Optics Group. The second is a classical homodyne technique which utilises an amplification effect inherent in homodyne and heterodyne detection. In this thesis these two methods will be presented along with work on applications on these methods. The final chapter presents work which is a culmination of

the knowledge gained in quantum imaging and holography, applying a holography techniques to imaging with undetected photons, a quantum interference imaging technique.

The remainder of this introduction aims to introduce some concepts which are common to the chapters within this thesis. The effects of different sources of noise in imaging is a central theme in this thesis and is discussed first. Quantum optics, and quantum correlation and entanglement are important to the work presented in Chapters 2 and 4 so some background to these topics is presented. Finally, the generation of light through spontaneous parametric downconversion (SPDC) is similarly an important part of the work presented in Chapters 2 and 4 so some brief background theory is discussed.

1.1 Noise Sources in Imaging

In order to understand the performance and limits of an imaging system it is necessary to be able to quantify the noise level of a system, and what the source of the noise is. Any imaging system will usually have various different sources of noise contributing to its overall noise level. Here, typical sources of noise will be discussed.

The most fundamental sources of noise in imaging are those which result from the quantum nature of light itself. The quantisation of the electromagnetic field means that the emission of light is a discrete process, and therefore subject to the statistical fluctuations that any random independent events are subject to. The photon number statistics of a source of light are a helpful way to categorise the amount of noise that can be expected and the corresponding limits on imaging performance. A source can be characterised in terms of its mean photon number $\langle N \rangle$ and its variance $\langle (\Delta N)^2 \rangle$ when considering a single spatial mode [10]. The photon number distribution of a classical state of light, is described by a super-Poissonian distribution with $\langle (\Delta N)^2 \rangle > \langle N \rangle$. For example, the photon number distribution of thermal radiation from a light bulb is described as $\langle (\Delta N)^2 \rangle = \langle N \rangle + \langle N \rangle^2$. The variance of the photon number puts a limit on the best possible noise precision when imaging. A coherent state, which best approximates laser radiation, has a Poissonian distribution $\langle (\Delta N)^2 \rangle = \langle N \rangle$. The variance of Poissonian distributed light forms the well-known shot noise or standard quantum limit, which represents the best

possible precision when imaging with classical or semi-classical states of light.

It is possible to generate states with a lower variance in photon number than Poissonian distributed light $\langle(\Delta N)^2\rangle < \langle N\rangle$. These sub-Poissonian states of light are strictly non-classical, for example the Fock or definite photon number state, whose variance $\langle(\Delta N)^2\rangle = 0$ [11]. The sub-Poissonian nature of the photon-number statistics of these states can allow for enhancements in imaging over classical super-Poissonian or Poissonian states, for example enhancements in signal-to-noise ratio [12]. If an optimal measurement scheme is chosen, sub-Poissonian states may reach the Heisenberg limit, which is defined by the minimum uncertainty allowed between two commuting observables in the Heisenberg Uncertainty Principle [13].

Another source of noise present in imaging is noise originating from the electronics of the detector. There are many sources of this noise, varying based on the architecture of the sensor, for example silicon CMOS, CCD and EMCCD as some examples [14]. As the architectures used in the work are mainly standard, such as CMOS and InGaAs, the main types of noise present in these types of sensor are discussed without a discussion of electron multiplying or intensified architectures. The main types of noise are read noise and dark current.

To explain these sources of noise we must understand how a typical sensor works. Each pixel contains a P-N junction photodiode, which when exposed to photons accumulates a charge of photoelectrons proportional to the number of photons incident on each pixel. This charge is then converted to a voltage by an amplifier, and a switching circuit then passes the voltages on each pixel to the output amplifier sequentially, where gain may be applied. The analogue signal is then converted to a digital value by the analogue-digital-converter (ADC) [15]. The first type of noise, dark current arises from the random generation of electrons and holes in the semiconductor used for the sensor. This effect is temperature and time dependent, with higher temperatures and longer exposures leading to higher dark current noises. The amount of noise is also dependent on the bandgap of the material used in the sensor. Silicon CMOS and InGaAs sensors have relatively low dark currents, and as such if they are cooled, and operated at video frame rates, the dark current will likely be small when compared to other noise sources. However, cameras operating in the mid-IR range or terahertz will have high dark currents, and typically need to be cooled to very low temperatures [16].

The other type of noise arising from the circuitry is readout noise. This is the noise that is created when the charge accumulated in the pixel is converted to a voltage by the readout amplifier. On average this process will give the correct value, but there will be random noise associated with the process depending on the quality of the readout circuitry. The amount of readout noise can be quantified by measuring bias frames, which are dark frames taken with a zero exposure, such that any variation in the numbers readout from the sensor is due to readout noise. Modern CMOS cameras typically have very low readout noises, with some as low as 0.2 photoelectrons per pixel [17]. However, other sensor architectures have much higher readout noises, for example this is usually at least two orders of magnitude higher from InGaAs sensors [18].

The last type of noise is environmental noise. This is any unwanted stray light that reaches the detector adds noise to the desired signal. This can be in the form of ambient lighting in a room or sunlight. It is not usually a problem in many applications as optical filters will be used to filter out unwanted wavelengths and if the signal is large enough will be negligible. However in some low-light applications environmental noise can become an issue as even a few stray photons per pixel can obscure the signal.

1.2 Quantum and Non-linear Optics

With the development of the laser the field of quantum optics was born. The need to understand the underlying quantum mechanical principles of laser physics meant much work was done in the 1950's and 1960's to apply quantum theory to the electromagnetic field. This would lead to greater understanding of the statistical nature of light and its detection, which could not be described by classical wave theories of light. Further, it would describe new quantum states of light which arise from the quantisation of the electromagnetic field, such as coherent states and Fock number states. The demonstration of the laser in 1960 would also provide an experimental means to test these new theories of quantum optics [19].

The introduction of the laser also allowed for developments in another emerging field of optics. The access to high-intensity light sources allowed for non-linear effects within different

materials to be explored, where the polarisation density **P** responds non-linearly to the electric field **E**. Shortly after the introduction of the laser various non-linear effects were demonstrated, with some of these proving useful for the generation of quantum states of light needed for quantum optics experiments.

Since access to quantum states of light in the lab, quantum optics experiments have been discovered various quantum optical phenomena and been used to test the fundamentals of quantum theory. Recently, there has also been a drive within the field to find technological applications of quantum states of light which could provide an advantage over classical technology, such as within areas of microscopy, communications and computing. It is here where the field of quantum imaging sits, with research to find how quantum of states of light can be used to image in advantageous ways to classical imaging methods.

1.2.1 Quantum Correlation and Entanglement

Many quantum optics and imaging experiments explore effects related to quantum correlation and entanglement. Broadly speaking, these are a result of the non-local effects of quantum mechanics, deliberated upon since the Einstein-Podolsky-Rosen paper (EPR paradox) [20]. Without wishing to repeat an extensively written about topic, a brief summary is as follows. EPR were concerned that quantum mechanics predicted that when two particles A and B are prepared in an entangled state, it was possible to predict the exact values of two non-commuting observable, e.g position and momentum, of particle B through measurements of particle A, even if the two were spatially separated. They concluded that particle B must have an exact value for each observable defined prior to measurement, which would violate Heisenberg's Uncertainty Principle. In their view this meant quantum mechanics could not be a complete description of reality, and they proposed a model of hidden local variables which determined the values of the observables.

Whilst EPR was contentious even at the time of its publication [21], the matter of local hidden variables would wait until the insights of John Bell. Bell came up with a statistical test which could determine whether a theory of local hidden variables was possible [22]. In essence, it places statistical bounds on the outcomes of an experiment, say the measurement

of spins on entangled photon pairs, that a model of local hidden variables could reproduce. If this bound is violated, it means that no theory of local hidden variables can reproduce the predictions of quantum mechanics. Since the conception of the Bell test, many experimentalists have implemented experimental Bell tests, which demonstrate the concepts of correlation and entanglement [23–27]. To date all experimental implementations have shown that the local hidden variable model is inconsistent with quantum mechanics, including more recent loophole free Bell tests [28, 29].

1.2.2 Spontaneous Parametric Down Conversion

With experimentalists beginning to test theories of quantum optics, sources of entangled photons or single photon states were needed. As mentioned access to high intensity laser sources allowed for the discovery of non-linear optical processes. Considering the polarisation density of a non-linear dielectric material **P**, the application of a strong electric field will result in the presence of higher order susceptibility terms $\chi^{(n)}$ [30]

$$\mathbf{P} = \varepsilon_0(\chi^{(1)}\mathbf{E}^{(1)} + \chi^{(2)}\mathbf{E}^{(2)} + \chi^{(3)}\mathbf{E}^{(3)} + ...). \tag{1.1}$$

One of these second order non-linear process ($\chi^{(2)}$) or three-wave mixing effects was observed to be useful in the generation of photon-pairs [31]. Spontaneous parametric downconversion is the process of a pump photon of frequency ω_p decaying into two photons, termed signal and idler, of lower frequency ω_s and ω_i [32]. As the process is parametric, energy is conserved and therefore [33]

$$\omega_p = \omega_s + \omega_i. \tag{1.2}$$

The signal and idler photons generated can either have the same frequency (degenerate down-conversion) or differing frequencies (non-degenerate downconversion). The emission of down-converted photons is greatest when the phase of the pump, signal and idler photons remain in phase through the length of the crystal and conservation of linear momentum is achieved

$$\mathbf{k_p} = \mathbf{k_s} + \mathbf{k_i}. \tag{1.3}$$

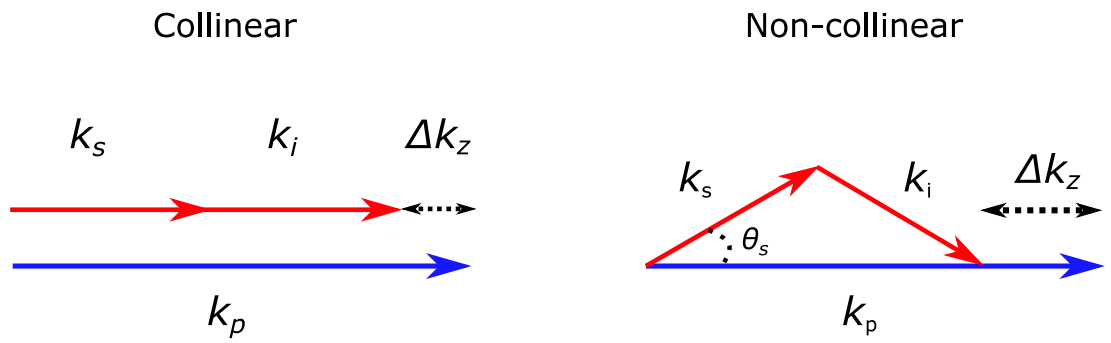

Figure 1.1: Diagram illustrating the cases of collinear and non-collinear emission in spontaneous parametric downconversion. The phase mismatch Δk_z determines both the efficiency and the spectral distribution of the downconverted signal and idler.

Collectively Eqs. 1.2 and 1.3 are referred to as the phase matching conditions [34–36].

When the phase matching conditions are met, downconverted photon-pairs may be emitted collinearly, with signal and idler photons travelling in the same direction as the pump, or in a non-collinear manner with the transverse momentum of signal and idler equal and opposite as seen in Fig. 1.1. Within experimental generation of photon pairs, a non-linear crystal is typically used as the medium within which the downconversion process takes place. Typically the transverse profile of the pump is smaller than the cross-sectional area of the non-linear crystal, such that the phase matching process is invariant to translations in the transverse directions [37]. However, the length of the crystal is finite, meaning the phase matching process is not invariant to translations in z. This leads to a phase mismatch of the z-components of the wave vectors [30, 38]

$$\Delta k_z = k_{p,z} - k_{s,z} - k_{i,z}. \tag{1.4}$$

The phase mismatch Δk_z is important both for determining the efficiency of the downconversion process, as well the spectral distribution of the emitted photon pairs [39]. When the emission is near-collinear, as is the case for the downconversion processes used in this work, the phase mismatch $\Delta k_z \leq \pi/L$, where L is the crystal length [40]. Importantly for imaging, the emission angle of the signal and idler photons can be derived from the phase mismatch, which can be used to determine various imaging parameters such as the field of view, resolution and number of spatial modes for a given downconversion imaging system. As such, the crystal length is an important consideration when designing an imaging system based on SPDC.

The conditions of successful phase matching depend on the type of crystal used to create downconverted photons. Crystals can either be uniaxial, characterised by a single optical axis and two principle refractive indices for the ordinary and extraordinary rays, or biaxial, characterised by two optical axes and three principle refractive indices. Further, the refractive indices experienced by the pump, signal and idler fields within the non-linear material will vary with wavelengths of the pump, signal and idler photons due to dispersion, as described by the Sellmeier equation. The magnitudes of the wavevectors of the three fields can be expressed as

$$\begin{aligned} k_p &= \frac{n_p(\lambda_p)\omega_p}{c}, \\ k_s &= \frac{n_s(\lambda_s)\omega_s}{c}, \\ k_i &= \frac{n_i(\lambda_i)\omega_i}{c}, \end{aligned} \tag{1.5}$$

for a given polarisation state. Within the experiments presented in this thesis, β-barium borate (BBO), a negative uniaxial crystal which exhibits birefringence was used [38]. For a birefringent material, the refractive index depends on both the wavelength and polarisation state of the light. The two possible refractive indices for each wavelength allow for the phase matching conditions to be met in different ways, either where the signal and idler waves have the same polarisation, known as type-I phase matching, or where the signal and idler waves are orthogonally polarised, known as type-II phase matching. For a negative uniaxial crystal ($n_e < n_o$), the phase matching conditions can be expressed as

$$\begin{aligned} \textbf{Type-I} \qquad & n_e(\omega_p) = \frac{\omega_s}{\omega_p} n_o(\omega_s) + \frac{\omega_i}{\omega_p} n_o(\omega_i), \\ \textbf{Type-II} \qquad & n_e(\omega_p) = \frac{\omega_s}{\omega_p} n_e(\omega_s) + \frac{\omega_i}{\omega_p} n_o(\omega_i). \end{aligned} \tag{1.6}$$

When using BBO crystals, these phase matching conditions are achieved by angle tuning of the crystal; changing the angle between the polarisation of the pump beam and the optical axis of the crystal alters the magnitude of the polarisation vectors between the three linearly polarised pump, signal and idler fields [41]. The phase matching conditions affect the spatial properties of the emitted signal and idler beams. In type-I SPDC, the two beams are emitted in a single

cone, with the photon pairs emitted in opposite directions about the pump beam axis to satisfy momentum conservation. In type-II, two spatially separated beams are emitted due to crystal birefringence [42, 43]. The overlap between the two beams can be adjusted by changing the angle between the crystal axis and direction of the pump beam. In the far-field of the crystal, the downconverted beams appear as a ring or beam, whose shape is determined by the spectral distribution of the downconverted photons. In the experiments presented here, only crystals cut for type-I downconversion are used.

1.3 Walkthrough

Here I will give a brief introduction to the topics that will be presented in the chapters that follow.

Chapter 2: In this chapter, work on quantum imaging with correlated photon pairs will be described. This work formed the basis of the publication "Quantum imaging with a photon counting camera" in *Scientific Reports* [44].

Chapter 3: In this chapter a holographic imaging scheme enabling images to be obtained under the noise floor of the detector will be described. This was applied to microscopy in the SWIR and stand-off detection at kHz frame rates. This work was published under the titles "Near single photon imaging in the shortwave infrared" in *Proceedings of the National Academy of Sciences* [45] and "Low photon-number stand-off speckle holography at kHz frame rates" in *Optics Continuum* [46].

Chapter 4: In this chapter work on holography techniques to so-called imaging with undetected photons, a quantum interference imaging scheme is presented. Part of this work concerned applying off-axis holography techniques to imaging with undetected photons schemes, and was published under the title "Single-frame transmission and phase imaging using off-axis holography with undetected photons" in *Scientific Reports* [47]. The other work described here is preliminary in nature, and describes a method for incorporating a spatial light modulator for spiral phase contrast imaging with undetected photons.

Chapter 5: In this chapter, conclusions to the work presented are discussed, and suggestions for future work are presented.

Chapter 2

Imaging with Correlated Photon Pairs

The realisation of SPDC as a reliable quantum source of light has led to the design of many imaging systems which are capable of utilising the correlations between photon pairs to gain an advantage over classical imaging systems. The first of these systems were restricted to single-pixel detectors, such as single-photon avalanche diodes (SPADs), to measure the spatial correlations of photons, which required raster scanning or structured illumination techniques to recreate an image [48–50]. However, the development of array detectors capable of detecting single photons has afforded many full-field quantum imaging experiments. Here, a brief overview of imaging schemes designed to gain advantages over classical, uncorrelated light using SPDC is described.

The first quantum imaging experiments to use correlations between photon pairs performed were so-called ghost imaging systems, originally proposed by Klyshko [51]. In ghost imaging setups, the spatially correlated photon pairs are separated into two beams, and coincidence detection between the two beams is performed. If an object is placed in one of the arms, then a coincidence count heralds the presence of an illumination photon and an image of the object can be built up, either by scanning with single-pixel detectors or by using a detector array. The first realisations of ghost imaging systems utilised single-pixel detectors and scanning [48–50]. However, later schemes utilised a single-pixel bucket detector to herald photons in one arm, with a single-photon sensitive array detector placed in the other [52–54]. Ghost imaging is not a uniquely quantum phenomenon, and various classical demonstrations have been implemented using statistical correlations [55–57]. However, quantum ghost imaging does have an advantage

over classical implementations in terms of achievable visibility, with the visibility limited to 1/2 in classical schemes when compared with a maximum visibility of 1 in quantum schemes [58]. Other promising applications apply to schemes which use non-degenerate downconversion to create photon pairs at differing wavelengths. In this way, one of the photon pair can be chosen to be at an easy to detect visible wavelength for which sensitive array detectors exist, and the other photon which probes the object at a wavelength for which a suitable array detector is either too noisy, slow or does not have sufficient spatial resolution. This was first demonstrated with 460 nm photons illuminating the array detector, whilst 1555 nm photons, for which detectors tend to be expensive and noisy, probed the object [59]. Later experiments have demonstrated the possibility of ghost imaging at even more challenging wavelengths for array detectors, such as X-ray and terahertz (THz) wavelengths [60–64].

Other quantum imaging schemes utilise the intensity correlations of the photon pairs emitted by SPDC. Unlike a classical source, where the intensity fluctuations are Poissonian, the photon pairs emitted by SPDC are subject to the same intensity fluctuations due to the correlated nature of the pair production process [65, 66]. This means if the intensity correlations between photon pairs are measured, the resulting noise of the measurement will be sub-shot-noise [67–69]. The added spatial correlations between the photon pairs emitted by SPDC mean that the intensity correlations can be measured on a detector array, allowing sub-shot-noise imaging of highly transmissive objects as well as phase objects [12, 70–72]. This has been proposed as a method for low photon number imaging in scenarios where higher illumination intensities are prohibited, such as biological imaging. In the presence of a strongly absorbing object however, the quantum advantage of the sub-shot intensity fluctuations quickly disappears [73], due to losses between photon pairs. Consequently intensity correlations have also been used to gain an advantage over classical absorption measurements for objects with absorption coefficients $\alpha < 0.5$ [73, 74].

The loss of a quantum advantage in sub-shot-noise imaging due to absorption is due to the intensity correlations between photon pairs being measured after their interaction with the object. This is a form of quantum decoherence, which is an issue in many quantum applications, not just in imaging [13, 75, 76]. Decoherence occurs when a system is subject to an interaction with its environment, leading to the system becoming entangled with the environment. The off-

diagonal terms of the density matrix, representing the quantum interference terms of the state, go to zero. In this way the system begins to lose its quantum interference effects, responsible for the enhancements in many measurement schemes, and more resembles a classical state. Quantum illumination protocols were suggested as a quantum measurement scheme that would retain a quantum advantage even in the presence of environmental noise and loss [77, 78]. In a quantum illumination protocol, a signal photon is sent to the object or target, with an idler acting as a reference to verify the presence of the object. The entanglement between the signal and idler allows for the distinguishing of signal events over noise events at the detector, even in the case that noise and loss completely destroys the entanglement between the signal and idler photons at the detector. This stands in contrast to many other quantum measurement schemes. This means quantum illumination protocols can offer an advantage in noise rejection over classical schemes, even with added classical noise [79]. As such, they have been proposed as the basis of quantum radar schemes, which would be protected from scrambling [80, 81], as well as for imaging systems that would be robust to noise. A quantum illumination protocol was first demonstrated experimentally to detect the presence of a beamsplitter in the signal arm [82, 83]. Later imaging versions would be demonstrated, first a single mode approach requiring scanning, and later a full-field approach utilising a detector array [84, 85].

Imaging with correlated photon pairs can also provide a spatial resolution enhancement over classical imaging. Typically, most imaging schemes will be limited by the diffraction limit [86, 87]. However, there exist various localisation methods, such as single molecule localisation microscopy, which are capable of beating the diffraction limit by a factor $1/\sqrt{N}$, where N is the number of probes (e.g., fluorescent photons) used in the localisation [88]. Correlated photon pairs, produced by SPDC, can be used to obtain a $1/\sqrt{2}$ ($N = 2$) enhancement in resolution by centroid estimation [89, 90]. Centroid estimation was originally developed for quantum lithography schemes, where a $1/N$ enhancement was achieved using entangled N00N states, reaching the Heisenberg limit [91–93]. Imaging schemes have similarly been able to show $1/N$ enhancement, with $N = 2$ using photon pairs from SPDC, realising the full theoretical quantum advantage [94–96]. Such quantum schemes may provide an advantage in scenarios where classical techniques, such as the use of fluorophores, are not possible. Recent quantum imaging

protocols have also demonstrated PSF correction through the use of correlated photon pairs and adaptive optics [97]. The spatial distribution of photon pairs on the detector gives information about the PSF of the system, with an imperfect PSF broadening the spatial correlations of photon pairs. By measuring this broadening of correlations, spatial light modulators can be used to correct for the aberration, allowing for guide-star free adaptive optics.

The largest downside, despite the advantages that imaging with correlated photon pairs can provide, is that the measurement of correlations between photon pairs typically requires the detection of single photons. This poses a challenge in terms of detection technology, with full-field detector arrays capable of single-photon detection being expensive and bulky, with some systems needing cooling for example. The main challenge, however, is that this requirement means that for most experiments the average illumination level has to be kept <1 photon per pixel per exposure. In order to build up an image, very long acquisition times are needed, especially in detectors with low time resolution such as EMCCDs. This precludes any imaging of a dynamic scene. The very low illumination levels, for which classical schemes would not be able to achieve comparable performance, have often been discussed as the application potential for photon pair correlated imaging schemes, for use in biological imaging settings where high illumination would damage cells. It has been noted, however, that for many of the imaging experiments discussed above, the illumination levels used are several orders of magnitude lower than cell damage thresholds [98,99]. The challenge for quantum imaging schemes which rely on measuring correlations is then how to reduce these acquisition times. SPAD array technology has emerged as a potential solution by measuring both spatial correlations between photons across the detector and time correlations between photon pairs due to their high time resolution [100, 101]. This allows for a reduction in the rate of accidental coincidences measured, increasing image contrast on a comparative number of frames.

2.1 Experimental Methods

In this section the experimental methods used for the detection of correlations between photon pairs from downconverted sources of light will be described. This includes details on the

different methods in which spatial correlations can be detected, and the detector technology commonly used.

2.1.1 Measurement of Spatial Correlations

Spatial correlations between photon pairs may either onbe measured in the form of position correlations in the image plane of the downconversion crystal or momentum correlations in the far-field of the crystal [102–105]. The image plane or far-field of the crystal can be imaged or projected onto the detector with imaging lenses. When imaging an object, the imaging system must be designed such that the object is also positioned in the correct plane of the crystal. When the detector is placed in the image plane of the downconverted crystal, the photon pairs arrive in spatially correlated positions on the detector as the photons are generated in the same position within the crystal. Placing the detector in the far-field of the crystal will result in photon pairs arriving at spatially anti-correlated positions due to the photon pairs being anti-correlated in their momenta. Figure 2.1 shows a diagram of position correlations in the case of type-I SPDC and momentum anti-correlations in the case of type-II SPDC.

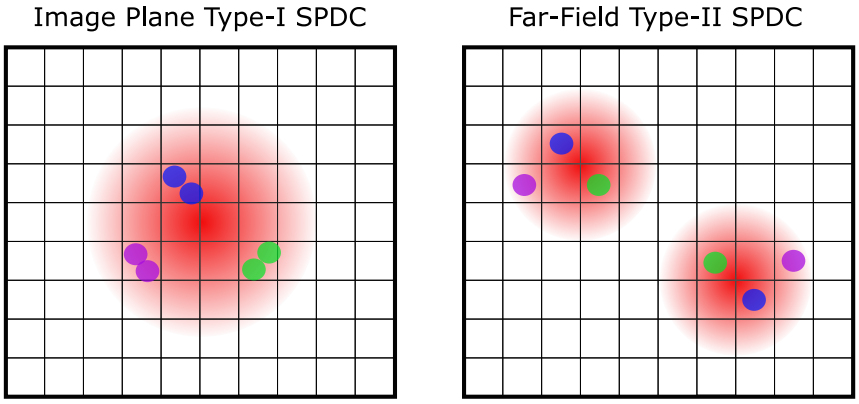

Figure 2.1: Diagram illustrating the arrival of spatially correlated photon pairs at the detector in the case of position correlations in the image plane with Type-I SPDC and momentum anti-correlations with type-II SPDC with the detector placed in the far-field of the crystal.

The spatial correlations are then measured by calculating the auto-correlation function in the case of position correlations or the cross-correlation function in the case of photons arriving at anti-correlated positions on the detector array. The resulting intensity correlation consists of a Gaussian distribution which represents a correlation performed on a distribution of randomly

correlated events. In the case where spatial quantum correlations are present, a peak will sit on top of the Gaussian distribution. The mean integrated correlation (i.e averaged over many frames) $\langle \mathscr{C} \rangle$, is given by

$$\begin{aligned} \langle \mathscr{C} \rangle &= \langle N_t^2 \rangle, \\ &= \langle (N_s + 2N_p)^2 \rangle, \\ &= \langle N_t \rangle^2 + \langle N_s \rangle + 4\langle N_p \rangle, \\ &= \langle N_t \rangle^2 + \langle N_t \rangle + 2\langle N_p \rangle, \\ &= \langle N_t \rangle^2 + \langle N_t \rangle + \sum_{\rho} \mathscr{C}_q(\rho), \end{aligned} \tag{2.1}$$

where N_t is the total number of events, N_s the number of singles and N_p the number of pair events. The value $\langle N_t \rangle^2 + \langle N_t \rangle$ represents the Gaussian portion of the correlation, whilst $\sum_\rho \mathscr{C}_q(\rho)$ represents the peak contributed to by correlated photon pair events over ρ frames. Eq. 2.1 shows that the distribution of N_t will be super-Poissonian in the presence of photon pairs. The Gaussian consists of singles (loss of a photon from a pair) and dark noise events, as well as coincidences between photons from different pairs if the number of pairs per frame is greater than one. An example of a cross-correlation on signal and idler beams from a type-II SPDC source averaged over 100,000 frames can be seen in Fig. 2.2. A full statistical analysis and model for measuring spatial correlations between bi-photons can be found in [106].

The size of the correlation peak is determined by the strength of the spatial correlations and is an important experimental measure of the efficiency of a system designed to image with correlated photon pairs. The size of the correlation peak is maximised when the detector is exactly positioned in the correct plane of the crystal, it is therefore necessary to place the detector on a translation stage and optimise the position of the detector relative to the size of the correlation peak. Furthermore, the measured correlation peak is determined by the transverse size of the spatial correlations convolved with the point spread function (PSF) of the imaging system. Therefore, it is also necessary to ensure the PSF of the imaging system is minimised through correct positioning and choice of lenses.

Ultimately, the size of the correlation peak will be limited by the transverse size of the spatial correlations. It is desirable that the size of the transverse correlations is at least as small as the

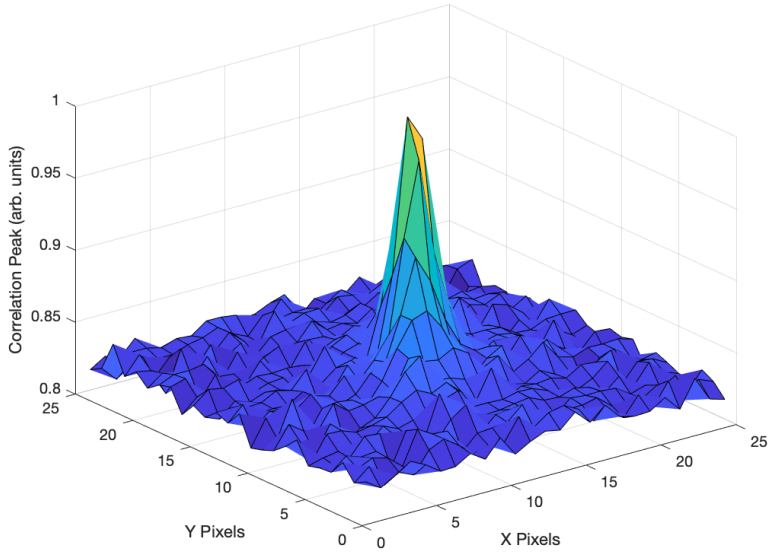

Figure 2.2: Example of a correlation peak calculated from the cross correlation function of two type-II SPDC beams, detecting anti-correlations in the far-field of the crystal. Correlation peak calculated from 100,000 frames.

dimensions of the pixels on the detector array, otherwise the correlated photon pair events will spread over many pixels. In the case of position correlations measured in the image plane of the crystal, the transverse size of the spatial correlations is given by

$$\sigma_{x,y} = \sqrt{\frac{\alpha L \lambda_p}{2\pi}}, \tag{2.2}$$

where $\alpha = 0.455$ a constant included to account for certain approximations in the calculation, L the thickness of the crystal, and λ_p the wavelength of the pump beam [54, 107]. Therefore, to minimise the transverse size of the spatial correlations it is desirable to choose a thin downconversion crystal and short wavelength pump laser. In the case of momentum anti-correlations in the far-field, the transverse correlation size arises from the transverse momentum uncertainty in the pump, given by

$$\sigma_{x,y} = \frac{4f}{k_p w_p}, \tag{2.3}$$

where k_p is the momentum of the pump beam, w_p the waist of the pump beam and f the focal length of the lens used to perform the transform to the Fourier plane of the crystal [108–110]. Accordingly, utilising a large pump beam waist and short focal length lens for the transform are

desirable when designing a system to image using momentum anti-correlations. In many cases, it will not be possible to match the transverse size of the correlations to the pixel size through these parameters alone, and it is necessary to demagnify the desired plane onto the detector with imaging optics. r

2.1.2 Detector Technology

Early work conducted into measurement of spatial correlations between downconverted photon pairs was conducted using single-photon sensitive detectors such as APDs or SPADs and using raster scanning techniques [111, 112]. Whilst scientific CMOS cameras have been used to observe spatial correlations between bright SPDC beams [113,114], the high readout noise of these detectors prohibits their use when imaging correlations between single photons. Single-photon sensitive array detectors, such as ICCDs or EMCCDs however, have allowed full-field quantum imaging and reduced acquisition time due to parallelisation of measurements across many spatial modes. Whilst the work presented in this chapter does not utilise an EMCCD detector, a brief overview of the detector technology has been provided as it important precursor to the results presented later as the standard technology in quantum imaging experiments at the time[1].

An Electron-Multiplying CCD or EMCCD works similarly to a CCD in that in each pixel there exists a potential well, which, when struck by an incoming photon releases electrons stored within the well. These electrons are then shifted horizontally and vertically to a readout register by an applied voltage. The key difference between an EMCCD and CCD is that there is an additional gain register before the CCD readout, which applies a large gain to the electrons present, amplifying them before the readout electronics [115, 116]. This enables EMCCDs to detect single photons as very small numbers of photoelectrons can be amplified above the noise of the readout circuitry [117]. However, the electron multiplication can also be of detriment to EMCCDs, as any electrons present before the readout circuity not corresponding to photon events will also be subject to a large amount of gain. This means electrons induced by thermal noise, or clock induced charge (the 'clock' voltage applied to shift electrons to the readout

[1]Detector technology within quantum imaging is a fast moving field; at the time of writing it could be argued that now SPAD arrays are the favoured technology with in quantum imaging owing to their superior time resolution, sensitivity and readout speeds.

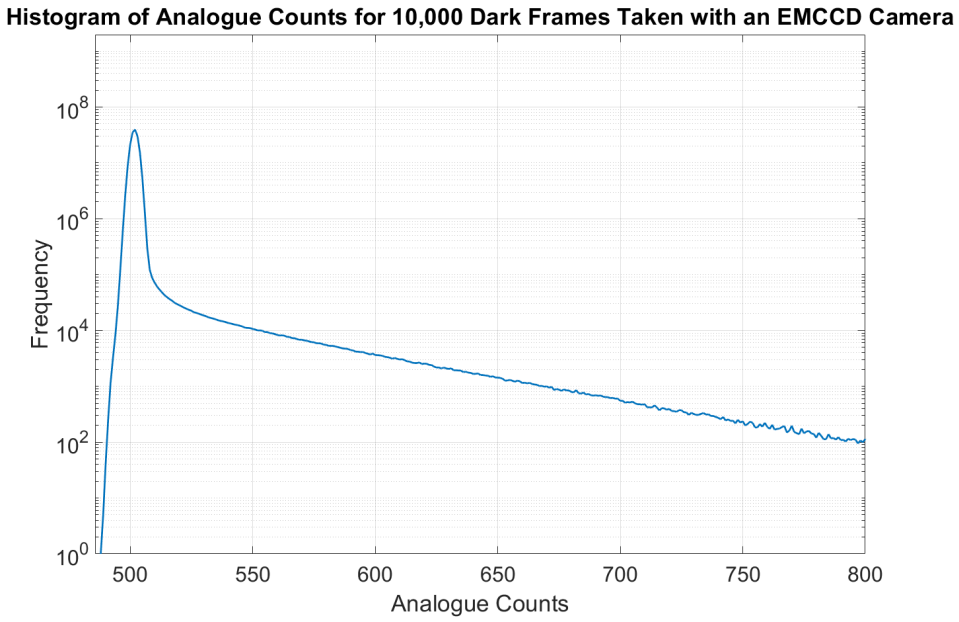

Figure 2.3: Histogram constructed from the analogue counts from 10,000 frames on a 128x128 region of an EMCCD camera. It can be seen the distribution of the counts follows a Gaussian distribution, corresponding to readout noise events, with a long tail at higher analogue counts corresponding to clock induced charge events.

register) produce events which can be difficult to distinguish from real photon events when using an EMCCD. Further this gain process is stochastic such that it is not possible to assign a precise photon number to the output of the EMCCD, at least without complex strategies [118]. Figure 2.3 shows an example histogram of analogue counts of 10,000 dark frames taken with an EMCCD. It can be seen that the distribution of counts consists of a Gaussian corresponding to counts caused by readout noise, with a long tail caused by clock induced charge events.

In order to accurately detect single photons, it is necessary to operate in a low illumination regime such that the probability of more than one photon arriving in each pixel is small. Then, a threshold can be determined from the Gaussian representing the readout noise of sensor. Typically a threshold $T = \mu + n\sigma$ is set, where μ is the mean of the Gaussian distribution, σ the standard deviation and n a constant to be chosen. Any counts registered above this threshold are said to be a photon event, while any counts lower are said to be zero photon events. Setting n too high will cause too many single photon events to be missed, whilst setting n too low will result in too many noise events being falsely registered as single photon events. In the work conducted in Glasgow a value of $n = 3.5$ is typical.

2.2 Quantum Imaging with a Photon Counting Camera

Note: In this section I will present the work that formed the basis of the publication "Quantum imaging with a photon counting camera". This work was completed in collaboration with Hamamatsu Photonics. Authors at Hamamatsu aided with implementation of the camera and designing the maximum likelihood algorithm for photon number estimation. All experimental work was performed in Glasgow by myself and Dr. Thomas Gregory, under supervision of Prof. Miles Padgett.

As discussed above, by utilising quantum correlations between photon pairs quantum imaging has been able to achieve advantages over classical imaging schemes. Typically quantum imaging schemes to date have used spatially resolved detectors such as EMCCDs or ICCDs to detect single photon events by the setting of appropriate thresholds or time gating the detector. The spatially resolved nature of these detectors allows the measurement of a large number of entangled states and enhancements have been realised in terms of image resolution [119], imaging through scattering media [120], sub-shot noise imaging [12] and noise rejection in quantum illumination protocols using such detectors [85, 121]. However the stochastic nature of the gain process in these detector types mean that the readout of multiple photon events is too noisy to resolve photon number and only single photon events can be determined.

The lack of photon number resolution is a disadvantage in image plane quantum imaging applications, where the most strongly correlated of photon pair events arrive in the same pixel or time bin. In these image plane applications, where photon number resolution is not possible, each photon in the pair is typically spatially separated such that they can be resolved, for example by introducing a pinhole to increase the PSF of the imaging system [119] or through changing the parameters in Eq. 2.2. The coincidences between spatially correlated pairs then have to be searched for over a larger kernel of pixels, which increases the number of accidental coincidences, limiting the efficiency of the system.

In the work presented here, a CMOS array detector which is capable of resolving the actual number of photons in each pixel was used allowing for a simpler method for the detection of

spatially correlated photon pairs. By constructing images consisting of either only two photon or one photon events, an increase in the ratio of two photon to one photon events is demonstrated for an SPDC source when compared to classical uncorrelated LED illumination. This increase is shown across a range of illumination levels, and allows for increased contrast in the two photon event images when using the SPDC source. The demonstration of such a scheme shows the possibility of utilising the full extent of the correlations between photon pairs in an image plane quantum imaging application.

2.3 Methods

2.3.1 Imaging System

The imaging system used in the work presented in this chapter is shown in Fig. 2.4. A 355 nm laser with a 10 mm beam waist is used to pump a 1 mm thick BBO crystal cut for type-I parametric down conversion. The down conversion process creates photon pairs of degenerate wavelength centred at 710 nm. A pair of dichroic interference filters is used after the crystal to remove any pump photons. The beam of down converted photons is then demagnified by a factor of 4 using lenses $L_1 = 400$ mm and $L_2 = 100$ mm onto an image plane which contains the binary spoke target used. This plane is then re-imaged onto the camera and further demagnified by a factor of 2 using lenses $L_3 = 100$ mm and $L_4 = 50$ mm. A 710 nm filter is placed on the camera to ensure only down converted photons reach the detector. The camera used was an scientific CMOS camera, a Hamamatsu ORCA-Quest, which through the design of the readout circuitry and low readout noise can resolve the actual number of photons in each pixel per exposure, up to a maximum of ~ 200 photons per pixel. The camera has a quantum efficiency of 55% at 710 nm. The fill-factor of the sensor is not specified by the manufacturer.

The crystal and magnification optics used in the experiment were chosen to maximise the number of pairs detected in the same pixel. The correlation strength of photon pairs in the image plane of the crystal is given by Eq. 2.2. With the crystal and pump laser used in this experiment, the correlation strength is calculated as 5.06 μm. Given a 10 mm beam waist, the number of spatial modes is estimated as $\sim (1976)^2$. With the camera having pixel sizes of

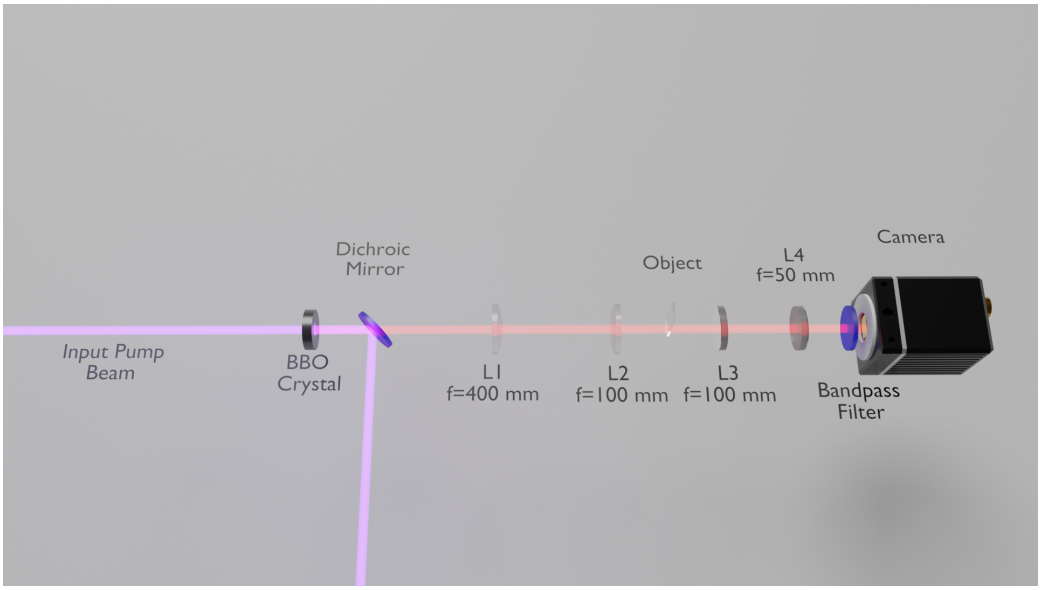

Figure 2.4: Diagram of the experimental setup used to image photon pairs. A 355 nm laser pumps a BBO crystal cut for type-I downconversion. A dichroic interference filter located after the crystal removes remaining pump photons. Photon pairs are generated at 710 nm, where lenses $L_1 = 400$ mm and $L_2 = 100$ mm demagnify onto an image plane which contains a binary spoke target. This plane is then imaged onto the camera and demagnified by lenses $L_3 = 100$ mm and $L_4 = 50$ mm.

4.6 μm, the correlation strength corresponds to a size of 1.1 pixels. The downconversion beams are then further demagnified by a factor of 8 such that the size of the correlations imaged onto the camera is 0.14 pixels. This does not account for broadening effects caused by an imperfect point spread function (PSF) however. The camera employs a trench structure between pixels on the sensor to minimise cross-talk so the effects of cross-talk were considered negligible for this experiment.

2.3.2 Photon Thresholding

For efficient detection of photon pairs it is crucial to accurately determine the correct number of photons in each pixel. A histogram of the digitised signal output of the camera can be built up over many frames to determine thresholds corresponding to each photon number. This histogram can be constructed over all events over all pixels in the region of interest being used, and global thresholds for each photon number can be set. An example of a global histogram constructed over 100,000 frames can be seen in Fig. 2.5. However, this was not determined to be the most accurate way to determine thresholds as the architecture of a CMOS sensor means each pixel

has its own readout circuit unlike a CCD where all pixels are readout by a single circuit. This means each pixel readout will show varying properties in terms of the offset, gain and noise. This means it is more accurate to construct histograms and set thresholds individually for each pixel rather than applying global thresholds. Example histograms from 2 pixels collected over 100,000 frames, showing differences in readout characteristics can also be seen in Fig. 2.5.

a)

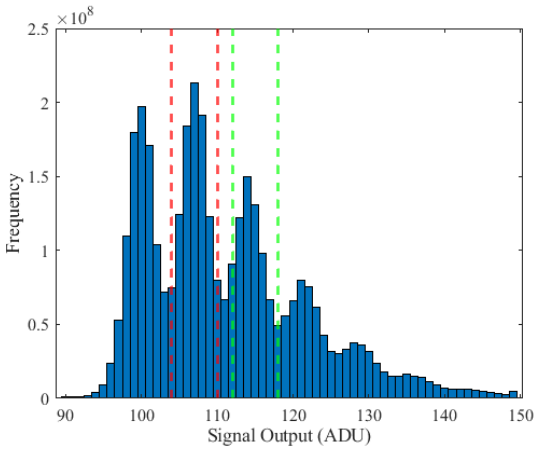

b)

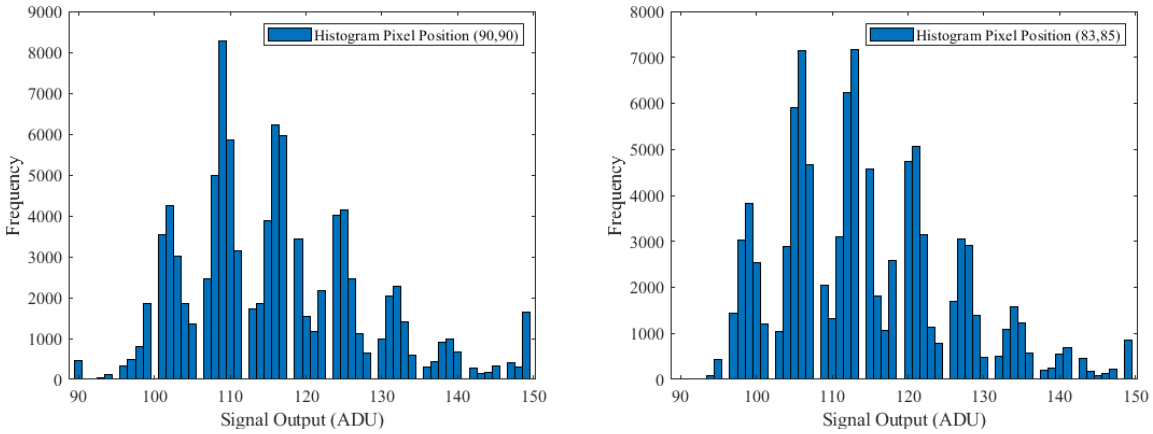

Figure 2.5: Histograms of ADU signal output. (a) Global histogram of events for all pixels over 100,000 frames within the region of interest illuminated by an LED. Red dashed lines indicate the peak corresponding to one photon events while the green dashed line shows the peak corresponding to two photon events. The peak before the red dashed line represents pixels for which zero-photon events are detected and is present due to an offset and a non-zero readout noise. Further peaks indicate greater than two photon events. (b) A selection of two histograms from two pixels within the region of interest, exhibiting slightly different readout characteristics.

In order to most accurately determine the photon number in each pixel it is important to fully consider the signal output of the camera. The offset of each pixel is determined as the average ADU value output under dark conditions. The gain of a sensor as a whole is determined as the mean and variance of the ADU output for a series of frames illuminated by varying intensities of

Poisson distributed light. From gain and offset a relation between ADU and photoelectrons can be determined, which for the camera used in this experiment was 1 ADU $= 0.12e^{-}$. The gain can also be calculated individually for each pixel, from the shape of its histogram, by counting the number of ADU per photon peak. This enables corrections to be made which can achieve uniform sensor response. With gain and offset maps for the sensor it is possible to convert each pixel value into units of photoelectrons, and set thresholds i.e $e^{-} < 0.5$ corresponds to 0 photons, $0.5 < e^{-} < 1.5$ corresponds to 1 photon and so on. Whilst this produces acceptable results, it does not consider the varying readout noises of each pixel. Some pixels will have larger readout noises than others, and this method of setting thresholds means many false positives will be registered in the data. In order to prevent this, a method based on maximum likelihood estimation was employed to determine thresholds.

The probability of the signal output for each pixel is a convolution of both the photon input statistics as well as the readout noise of the specific pixel. The readout noise of the pixel is typically a continuous Gaussian distribution while the photon input will be discrete and dependent on the source. The readout noise can be determined for each pixel from dark frames, and the photon input statistics are estimated empirically from 10 pixels with below average readout noise (around $0.18\,e^{-}$). A small proportion (2.4%) of pixels have non-Gaussian readout noise distributions, these are excluded from any further analysis. Given a value of the signal output, a likelihood function can be constructed which returns the most likely number of the photon input based on these probability distributions. The value of the signal output at which it becomes more likely that the photon number output is the next value becomes the threshold between the photon numbers.

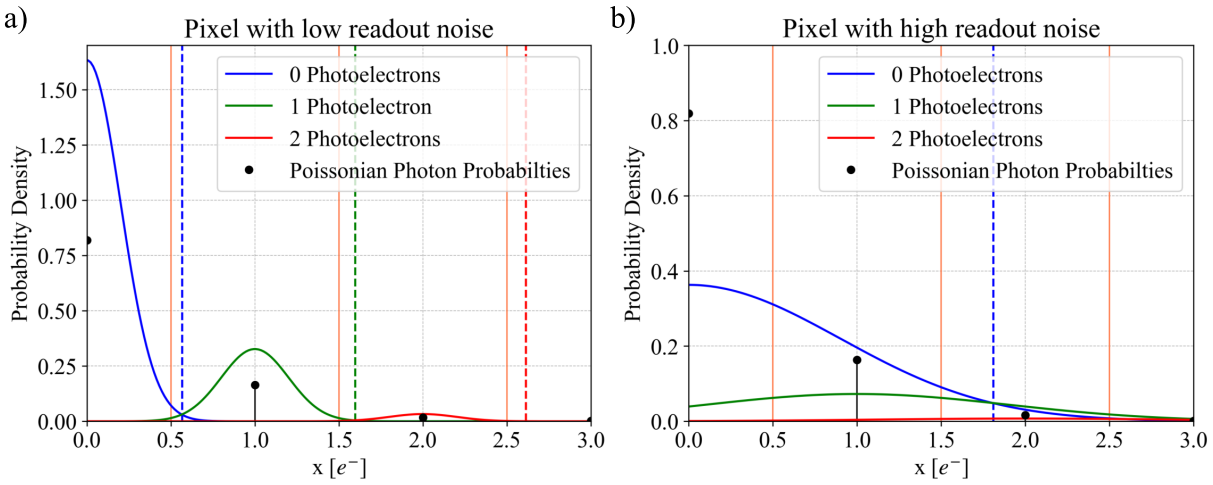

Figure 2.6: Histogram for photon number thresholds in the case of a) a pixel with a low readout noise and b) a pixel with a high readout noise. In the case of the pixel with a low readout noise the peaks corresponding to different photon numbers are well resolved and it is possible to set thresholds to distinguish the number of photon events that occurred at that pixel. However in the case of the high readout noise it can be seen that the peaks are not well resolved making the setting of thresholds in order to distinguish the number of photon events inaccurate or impossible.

An example scenario is shown in Fig. 2.6, for a Poissonian photon source with an average signal of $0.2\,e^-$ but for two pixels with noises, one with a readout noise of $0.2\,e^-$ and one with $0.9\,e^-$. The solid orange lines indicate the original thresholds described above based on half marks between the photoelectron events, while the dashed lines indicate the thresholds based on maximum likelihood. Using the maximum likelihood method, when the signal intensity is low ($< 1\,e^-$ per pixel), it can be seen that higher thresholds are set than the original method, especially in the case of a pixel with a high readout noise. This avoids as many false 1 and 2 photon events being registered. There will be some increase in the number of false negative 1 and 2 photon events, however this does not degrade image quality as much as a false positive.

2.4 Results

By determining the number of photons in each pixel with the method outlined above, images consisting of only one-photon or two-photon events were obtained, as shown seen in Fig. 2.7. A binary star target was imaged over $10,000$ frames, and an intensity cross section was generated by averaging over the rows indicated in Fig. 2.8. The one-photon event images has a greater number of events and displays a smoother intensity distribution over the SPDC beam as a result.

However, a greater number of these events occur in the dark regions of the image masked by the object, which reduces the image contrast. These are a result of camera noise events which are falsely identified as one-photon or two-photon events, but are fewer for the two-photon image. The reduction on contrast can be seen in the intensity cross-sections shown in Fig. 2.7.

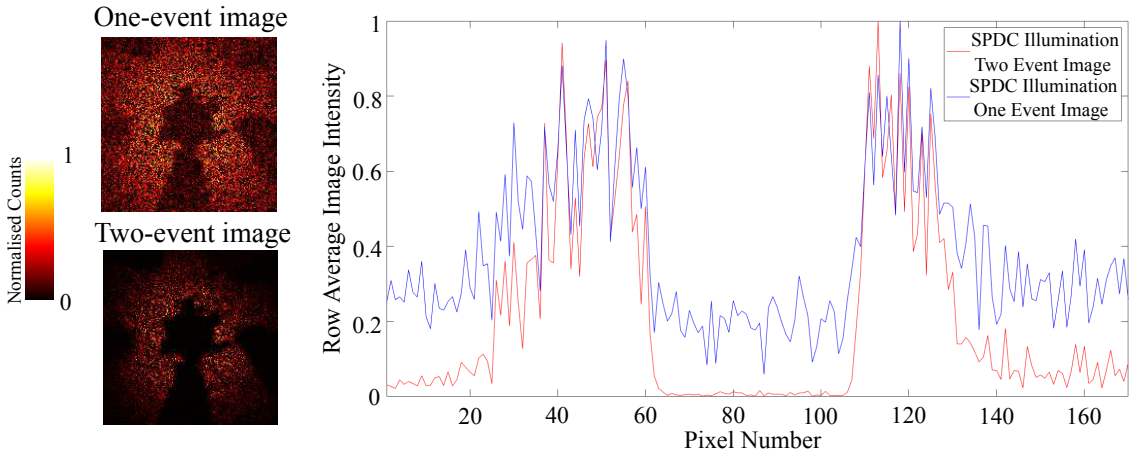

Figure 2.7: Comparison of images of a binary star target consisting of one-photon events and two photon events. Images acquired over 10,000 camera frames. Each image has been normalised independently to its maximum value, to allow representation on the same scale. The number of photon illumination events was equal to 4.70 times the noise events on the camera, as calculated from dark frames. A cross-section of the normalised intensity for the one-photon event image (blue) and two-photon event image (red) against pixel number is also provided. The cross-section was constructed by averaging rows 80-110 of the image, as indicated by the blue dotted lines in Fig. 2.8. The intensity cross-sections for each image were normalised to their maximum value for representation on the same scale.

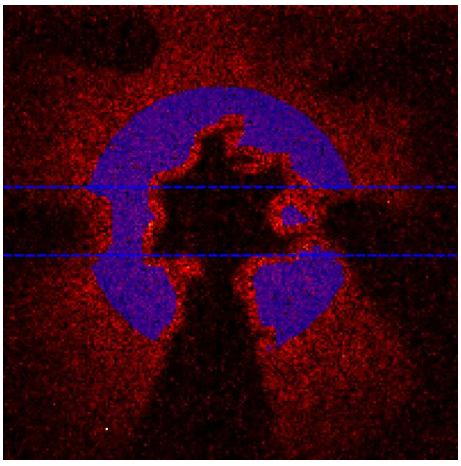

Figure 2.8: Image showing the region over which the different metrics used are calculated, as indicated by the blue circle. This defines the extent of the SPDC beam. The region used contains 5103 pixels. The blue dotted lines also indicate the rows 80-110 which are averaged over in the intensity cross-section graphs.

In order to evaluate the performance of correlated photon pair imaging, the two-photon event images from the down-conversion source were compared against two-photon event images from a classical source (LED illumination). These comparison images, shown for increasing light levels, can be seen in Fig. 2.9. The illumination levels are set in reference to the noise level of the camera, where 1 noise equivalent count (NEC) is an illumination such that the number of illumination events is equal to the number of camera noise events. Also shown is the average number of events per pixel for each image, and the ratio of two-photon to one-photon events (2/1 ratio). The 2/1 ratio is calculated from the number of recorded two-photon events and the number of rejected events for each image. This is a key performance metric as it represents the ability of the imaging system to select downconverted photon pairs. Illumination with the down-conversion source shows an increased 2/1 ratio when compared with illumination from the LED source. Fig. 2.10 shows the two-photon to one-photon event ratio across a greater range of illumination levels. At lower illumination levels the advantage in 2/1 ratio is greater, whereas the advantage is less at higher illumination levels. This is as at the higher light levels although the number of photon pairs from the down-conversion source is greater, there are also many more false positive two-photon noise events. These false positive two photon events arise as a result of combinations of camera noise, for example a camera noise event pairs or a camera noise event and a single photon. The proportion of true two-photon events is maximised at illumination levels where the number of photon events are approximately equal to the number of camera noise events.

	NEC	Events /Pixel	2/1 Ratio	Two Photon Event Images	Image Intensity Cut Throughs
LED	1.53	0.015	0.012	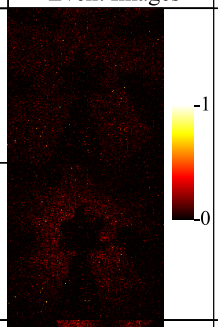	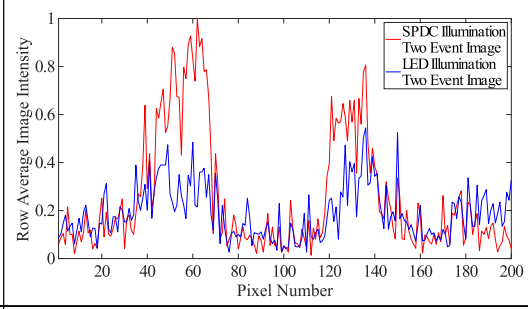
SPDC	1.73	0.017	0.020		
LED	5.64	0.041	0.025	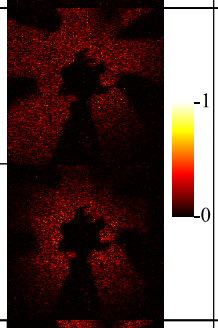	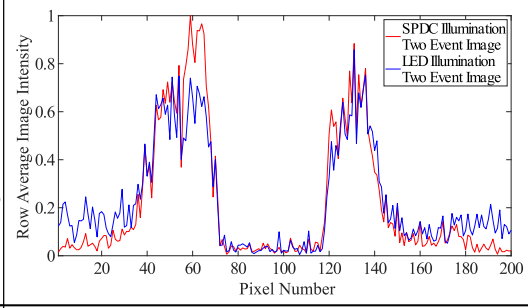
SPDC	4.70	0.035	0.030		
LED	11.92	0.079	0.047	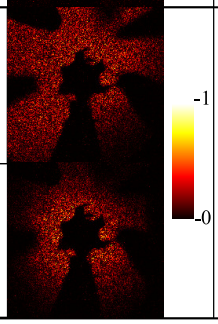	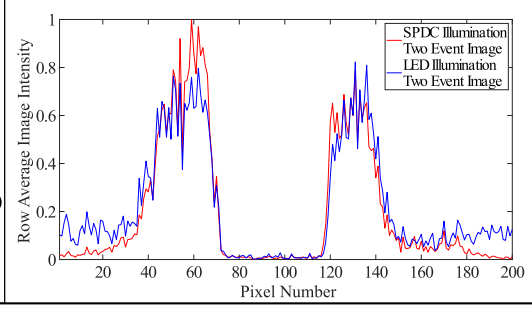
SPDC	10.65	0.071	0.051		

Figure 2.9: A comparison between SPDC and LED illumination at a range of increasing illumination levels. Shown are images constructed from two-photon events for both SPDC and LED illumination, acquired over 10,000 frames, alongside intensity cross-section plots for the displayed image pairs. The ratio of two-photon to one-photon events (2/1 ratio) is calculated for each image from the number of rejected one photon events, showing an improved 2/1 ratio when using the SPDC source compared with LED. Illumination levels for each image are quantified in terms of the number of events per pixel, and NEC (noise equivalent counts) in reference to the number of camera noise events.

The intensity cross-sections in Fig. 2.9 show that the increased 2/1 ratio provides an improvement in image contrast where the object is illuminated by the SPDC source rather than LED illumination. This can be seen image intensity cross-sections shown alongside the images in Fig. 2.9. The enhancement in contrast closely follows the 2/1 ratio of photon events, with greater improvement seen at the lower light levels. A maximum improvement in the 2/1 ratio by a factor of 1.66 is seen for the pair of images obtained at an illumination level of $\sim$ 1.5 to 1.7 NEC.

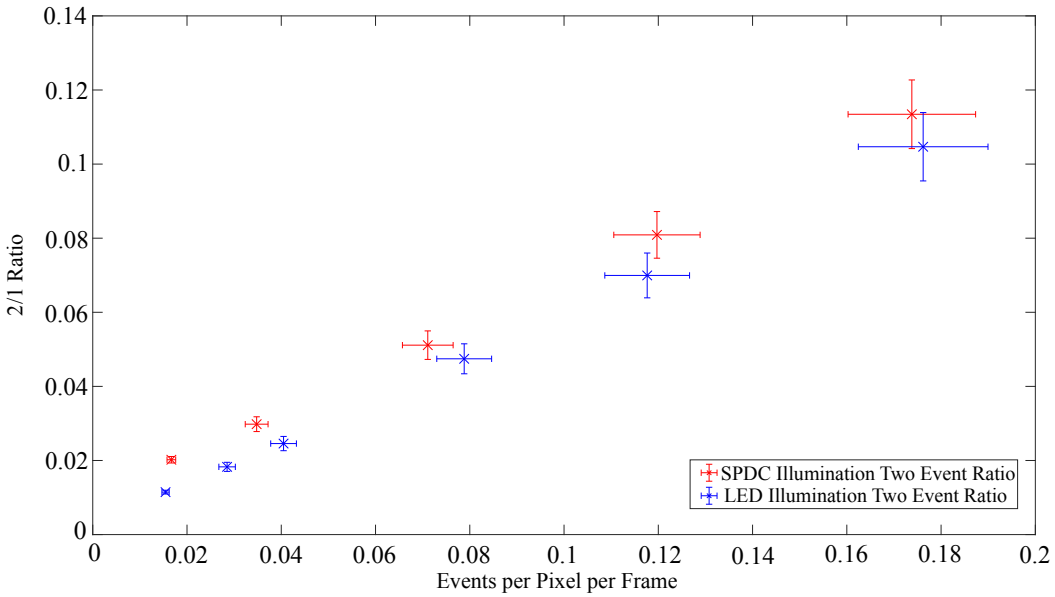

Figure 2.10: A graph of the calculated 2/1 ratios against the number of events per pixel per frame for an extended set of two-photon event images for SPDC and LED illumination. Error bars represent the standard error on the mean, calculated for 10 blocks of 10,000 frames. Error bars are larger at higher numbers of events per pixel per frame as the variance on the number of events recorded is higher at higher illumination levels.

Given that the key performance parameter in the experiment is the ratio between the number of pixels containing a one-photon event, and the number of pixels containing a two-photon event it is worth discussing the detection statistics to explain the performance of the experiment. Considering the limit of zero detector noise, and assuming sparse illumination with the number of events per pixel per frame $E_{Tot,Photon} \ll 1$, then for a classical (LED) source emitting photons with a random spatial distribution the fraction of pixels containing a one-photon event is $E_{Tot,Photon} \approx E_{Tot,Photon}$ and the fraction of two-photon events is $E_{2,Photon} \approx \frac{1}{2}E_{1,Photon}^2$, giving a two to one photon event ratio of $\approx \frac{1}{2}E_{Tot,Photon}$.

Considering an SPDC photon pair source at the same illumination intensity, and assuming that the size of the position correlations are small compared to the pixel size, then the increase in the 2/1 ratio will depend on the efficiency of detecting both photons in a pair in the same pixel, the heralding efficiency, η. This heralding efficiency determines the upper bound of the performance of the pair source when compared with the LED. Under the conditions of a low heralding efficiency the 2/1 ratio is $\approx \frac{\eta}{2} + \frac{E_{Tot,Photon}}{2}(1-\eta)^2$.

When considering the reality of a detector with noise, the above relation no longer holds.

The camera read noise is guassian and therefore it does not follow that the number of two-photon noise events is equivalent to half the number of one-photon noise events squared, i.e $E_{2,Noise} \neq \frac{1}{2}E_{1,Noise}^2$. In the presence of detector noise the expected number of additional events corresponding to accidental instances of two-photon events in the case of classical uncorrelated illumination then becomes $\frac{1}{2}E_{1,Photon}^2 + E_{1,Photon}E_{1,Noise} + E_{2,Noise}$.

It follows from these detection statistics that the largest difference between the 2/1 ratio for the LED and SPDC sources will be obtained when operating at a low number of total events per pixel per frame, $E_{Tot,Photon}$, and a high heralding efficiency, η. In practise, the lower limit on $E_{Tot,Photon}$ is set to be higher than the camera readout noise to avoid images being completely overcome with camera noise. The practical heralding efficiency is determined by a number of factors such as the quantum efficiency of the sensor, losses in the imaging system and imperfect point spread function (PSF) meaning the extent of the correlations is larger than the size of the pixels. In this experiment the greatest difference between two-photon and one-photon event ratio between the LED and SPDC sources is obtained at low illumination levels of ~ 1.5 to 1.7 NEC where the number of accidental two-photon events is minimised. For a dark event rate of 0.006 events per pixel per frame this means $E_{Tot,Photon} \approx 0.016$ events per pixel per frame. Using the SPDC photon-pair source results in an increase in the two-photon to one-photon event ratio by a factor of 1.66 when compared to the LED illumination. In future the two-photon to one-photon ratio obtained using a SPDC source could be improved through an increase in the heralding efficiency of the optical system, η, or a decrease in the readout noises of future CMOS sensors.

2.5 Discussion

By resolving the actual number of photons in each pixel a new method for the detection of spatially correlated photon-pairs from an SPDC source has been demonstrated. Through use of this method we demonstrated an improvement in the ratio between two-photon and one-photon events for a correlated SPDC source when compared with classical LED illumination across a range of illumination levels. Through this improvement in two-photon to one-photon events,

images consisting of only two-photon events show improved contrast when illuminated by the SPDC source. This improvement is greatest at low illumination levels where the contribution of accidental two-photon events is minimised. Whilst the improvement in two-photon to one-photon ratio reported in this work is modest, it demonstrates the validity of the concept and may prove useful for future quantum imaging applications.

Quantum imaging experiments that rely on the detection of both photons generated by the down-conversion process to realise an enhancement over classical imaging could benefit from the technology and methods presented here. In experimental setups designed with the detector positioned in the image plane of the down-conversion crystal, the most tightly correlated photon pairs arrive in the same pixel, which cannot be easily recovered with existing CCD or CMOS technology where it is difficult to distinguish between the number of photon events. The methods presented here allow for an increase in the per frame amount of information obtained, which could lead to increased efficiency and reduced acquisition times in these types of experiment.

Further, the ability to distinguish between multiple photon events in each pixel presents an opportunity for the measurement of spatial correlations between photon pairs in higher gain regimes of SPDC, where photons from multiple pairs will arrive in each pixel. This could allow for shorter acquisition times in quantum imaging schemes, as the requirement that only a single photon from a pair be present in each pixel would be lifted, and illumination levels could be increased. Later work conducted comparing the performance of the CMOS detector used here to an EMCCD detector in measuring spatial correlations across different illumination levels found that the EMCCD slightly outperformed the CMOS detector at illumination levels of < 1 photon per pixel per frame but that the CMOS detector outperformed the EMCCD at illumination levels higher than this, due to the ability to resolve the number of photons in each pixel [122].

With the performance set by the efficiency of photon-pair detection and the camera readout noise it is expected that improvements to these factors would yield more dramatic enhancements in image contrast. Higher photon-pair detection efficiency could be achieved by creating photon pairs at a shorter wavelength where the quantum efficiency of the sensor is higher, or by using a down-conversion crystal with a shorter length to create more tightly correlated photon-pairs. Further future advancements in CMOS and photon counting technology should result in lower

readout noises. With the higher contrast enhancements that may result from these changes it is expected that images could be acquired on fewer frames where it would only be possible to reveal the object using a quantum pair source, with classical illumination failing to reveal the object. Such an experiment approaching real time imaging could find applications with low-light quantum microscopy or covert detection.

Chapter 3

Imaging Below the Detector Noise Floor with Digital Holography

3.1 Holography

In the 1940s Dennis Gabor, a Hungarian-British engineer and physicist was working on improving electron microscopes. Whilst the electron microscope had a greatly improved resolving power compared with visible microscopes, the magnetic electron objective lenses were severely affected by spherical aberration. His idea was to remove the objective lens altogether, recording both the amplitude and phase of the wavefronts diffracted by the electron beam through interference with a reference beam and recording the interference pattern, or hologram, on a photographic plate. The object wavefronts could then be reconstructed optically, by illuminating the photographic plate with a mercury lamp and using conventional objective lenses. When the hologram was illuminated, a real and virtual image of the object would form. With his 'new microscopic principle', Gabor showed that not only can the image be reconstructed without an objective lens, but also that full three dimensional information about the object is contained within the hologram [123].

Gabor's idea, while remarkable, was broadly left untouched by the scientific community for a number of years. The practicality of holography was limited by the lack of high coherence sources, poor image contrast due to the in-line nature of the recording process and the require-

ment of recording the holograms on photographic plates. The invention of the laser provided high coherence sources, which made the recording and reconstruction of visible holograms much more practical. With renewed interest, Leith and Uptnaiks would develop a solution to the poor quality of reconstructed images due to the overlapping reference beam by changing the recording geometry to an off-axis layout [124]. Finally, the availability of digital cameras, combined with Cooley and Tukey's FFT algorithm [125], allowed for the recording and reconstruction of holographic images to be a completely digital process. In spite of the early lack of interest, these practical developments have meant holography has become a widely applied technique across microscopy, industrial process monitoring, data storage and medicine. As such, Gabor was awarded the Nobel Prize in Physics for his work on holography in 1971.

3.1.1 Theory of Holography

In order to record a Gabor type or 'in-line' hologram, a beam illuminates the object, and the diffracted wavefronts from the object interfere with the primary beam to create an interference pattern. The interference pattern contains information about the field of the object wave, and has the form

$$\begin{aligned} I_{tot} &= |E_{obj}(\mathbf{r}) + E_{ref}|^2 \\ &= |E_{obj}(\mathbf{r})|^2 + |E_{ref}|^2 + E_{obj}(\mathbf{r})E_{ref}^* + E_{obj}(\mathbf{r})^* E_{ref}, \end{aligned} \tag{3.1}$$

where $E_{obj}(\mathbf{r})$ is the scattered object field and E_{ref} the primary reference wave. This interference pattern is then recorded on a screen or a CCD to create the hologram. In the case of a physical hologram, when it is illuminated by the reference wave again the light scatters from the hologram and the field takes the form

$$\begin{aligned} E_{holo} &= E_{ref}(a + bI_{tot}) \\ &= E_{ref}(a + b|E_{ref}|^2) + bE_{ref}|E_{obj}(\mathbf{r})|^2 + bE_{obj}(\mathbf{r})|E_{ref}|^2 + bE_{obj}(\mathbf{r})^* E_{ref}^2, \end{aligned} \tag{3.2}$$

where a and b are constants due to the linear response of the holographic film. The first term is spatially constant and the second much smaller than the others as the scattered object field is much lower than the reference field. This leaves the terms containing $E_{obj}(\mathbf{r})$ and $E_{obj}(\mathbf{r})^*$,

which represent the real and virtual image viewed by an observer behind the holographic film. The presence of the virtual image is a major issue for in-line holography, as an observer focusing on the real image will see the out of focus virtual image superimposed due to the in-line geometry of the recording process. This vastly reduces the image quality.

A solution to this problem appeared a couple of decades after the introduction of holography in the form of an off-axis geometry for the recording of holograms. Informed by concepts from communication theory, the work of Lohmann and Leith and Upatnieks suggested a method where a carrier frequency is added to the object field [124, 126]. In an optical setup this takes the form of a spatial modulation, with the reference beam tilted with respect to the object beam. This is demonstrated in Fig. 3.1. Now the recorded intensity pattern takes the form

$$I_{tot} = |E_{obj}(\mathbf{r})|^2 + |E_{ref}|^2 + E_{obj}(\mathbf{r})E_{ref}^* e^{-i\mathbf{k}\cdot\mathbf{r}} + E_{obj}(\mathbf{r})^* E_{ref} e^{i\mathbf{k}\cdot\mathbf{r}}, \tag{3.3}$$

where $\mathbf{k}\cdot\mathbf{r}$ represents the angle between the object and reference fields. It can now be seen following the same re-illumination process as in Eq. 3.2 that the real and virtual images are now offset from each other (and the other terms) by angle $\mathbf{k}\cdot\mathbf{r}$ This greatly increases the signal to noise ratio of the reconstructed image.

The other practical benefit to holography was the realisation that not only could holograms be recorded digitally, but the reconstruction process could also be carried out digitally by computers, without the need for the re-illumination process. Goodman realised that the FFT algorithm allowed for a reconstruction of the images through a Fourier transform of the recorded hologram, which is equivalent to the re-illumination process (the diffraction of the plane wave by the hologram can be thought of as a linear superposition of plane waves) [127]. By taking an FFT of an off-axis hologram, the spatial frequency components of the object appear offset from the DC components (the first two terms in Eq. 3.3). These can be filtered off to leave just the virtual and real image terms.

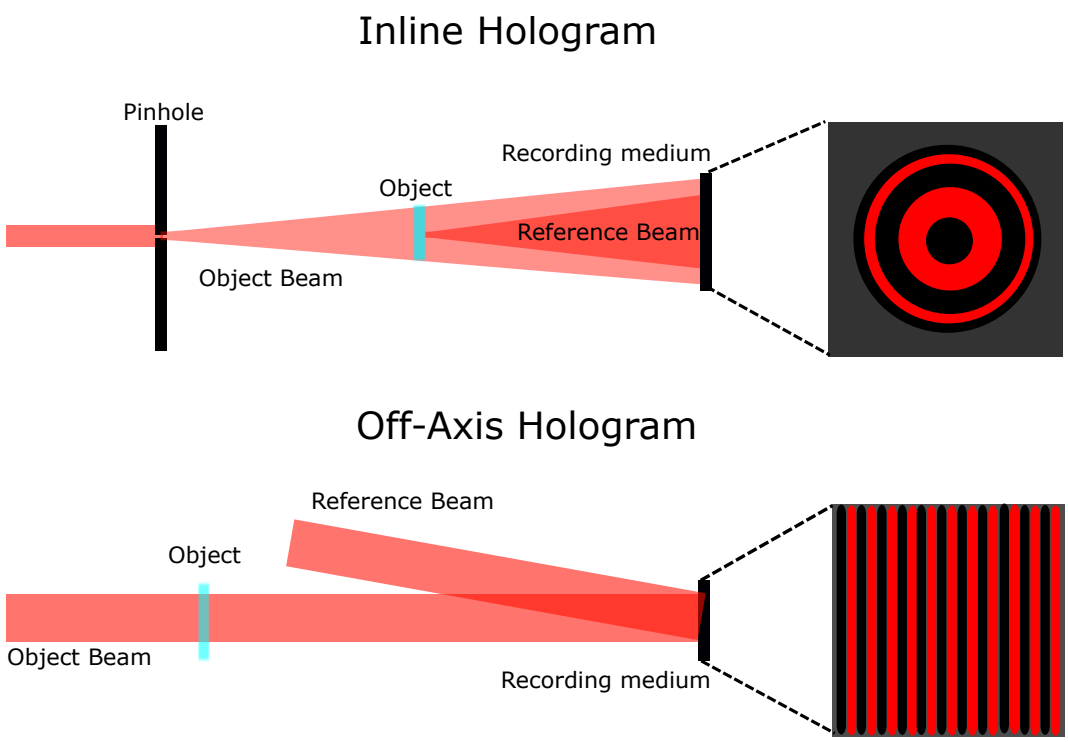

Figure 3.1: Comparison of experimental setups for in-line and off-axis holography configurations. In the off-axis configuration the angle between the signal and reference beams introduces a carrier frequency to the object beam to offset the spatial frequencies of the object from the DC components.

3.1.2 Experimental Methods

In order to obtain intensity and phase images from a digital hologram, first interference fringes must be recorded on the camera, then numerical reconstruction must be performed on the recorded fringe pattern. This section outlines the experimental methods used to record holograms and reconstruct intensity and phase images.

To record holograms of an object, an interferometer must be aligned to record the interference of the object beam with a reference. The main alignment consideration for either interferometer design is the temporal coherence between the object and reference beams. In order to record an interference pattern, the phase between the object and reference beam must be stable over the integration time of the camera. The coherence time of a source of light, defined as

$$t_c = \frac{1}{\pi \Delta \nu}, \tag{3.4}$$

where $\Delta\nu$ is the linewidth of the source, provides a measure of the timescale over which the

phase is stable. It is common to convert the coherence time to a length scale, defining the coherence length of a source as $l_c = ct_c$, where c is the speed of light. To ensure interference is observed, the path length distance between the object and reference beams must be kept within the coherence length of source. Therefore, lasers are a common choice of source for holography applications due to their high spatial and temporal coherence.

When an interference pattern containing the object has been obtained on the camera, intensity and phase images can be reconstructed either by phase-stepping (for an in-line hologram) or off-axis digital holographic reconstruction techniques. As the results presented in this thesis use off-axis methods, phase-stepping will not be described; however an overview can be found in [128]. A schematic of the reconstruction process can be seen in Fig. 3.2. The first step is an optional subtraction of the reference and object beam intensity to suppress the contribution of these terms to the DC component of Fourier transform. This step may not be needed if the fringe contrast is high and the diffracted orders are well separated from the DC in spatial frequency space, as they can simply be filtered off. However, in the case of poor fringe contrast, for example unbalance of the object and reference beam intensities in the interferometer, or insufficient separation from the DC components, then performing this subtraction can improve the SNR of the resulting reconstructed images. The next step is performing a Fast Fourier Transform on the interference pattern. From Eq. 3.3 a Fourier transform of the interference pattern with signal and reference images subtracted gives

$$\mathscr{F}Re\left[E_{obj}(\mathbf{r})E_{ref}^{*}e^{-i\mathbf{k_{tilt}}\cdot\mathbf{r}} + E_{obj}(\mathbf{r})^{*}E_{ref}e^{i\mathbf{k_{tilt}}\cdot\mathbf{r}}\right] = f(\mathbf{k}-\mathbf{k_{tilt}}) + f^{*}(\mathbf{k}+\mathbf{k_{tilt}}), \tag{3.5}$$

where $f(\mathbf{k}-\mathbf{k_{tilt}})$ is the Fourier transform of $E_{obj}(\mathbf{r})E_{ref}^{*}e^{-i\mathbf{k_{tilt}}\cdot\mathbf{r}}$. This gives two well separated peaks $\mathbf{k}$-space, with the separation given by the vector $\mathbf{k_{tilt}}$, which is determined by the angle between the object and reference waves. Achieving adequate separation in $\mathbf{k}$-space requires that the spatial frequency of the interference fringe oscillations is faster than all spatial frequencies contained within E_{obj} and E_{ref}.

With two well separated peaks in $\mathbf{k}$-space, digital filtering can then be applied to select one of the peaks. Different types of filter were experimented with over the course of the work pre-

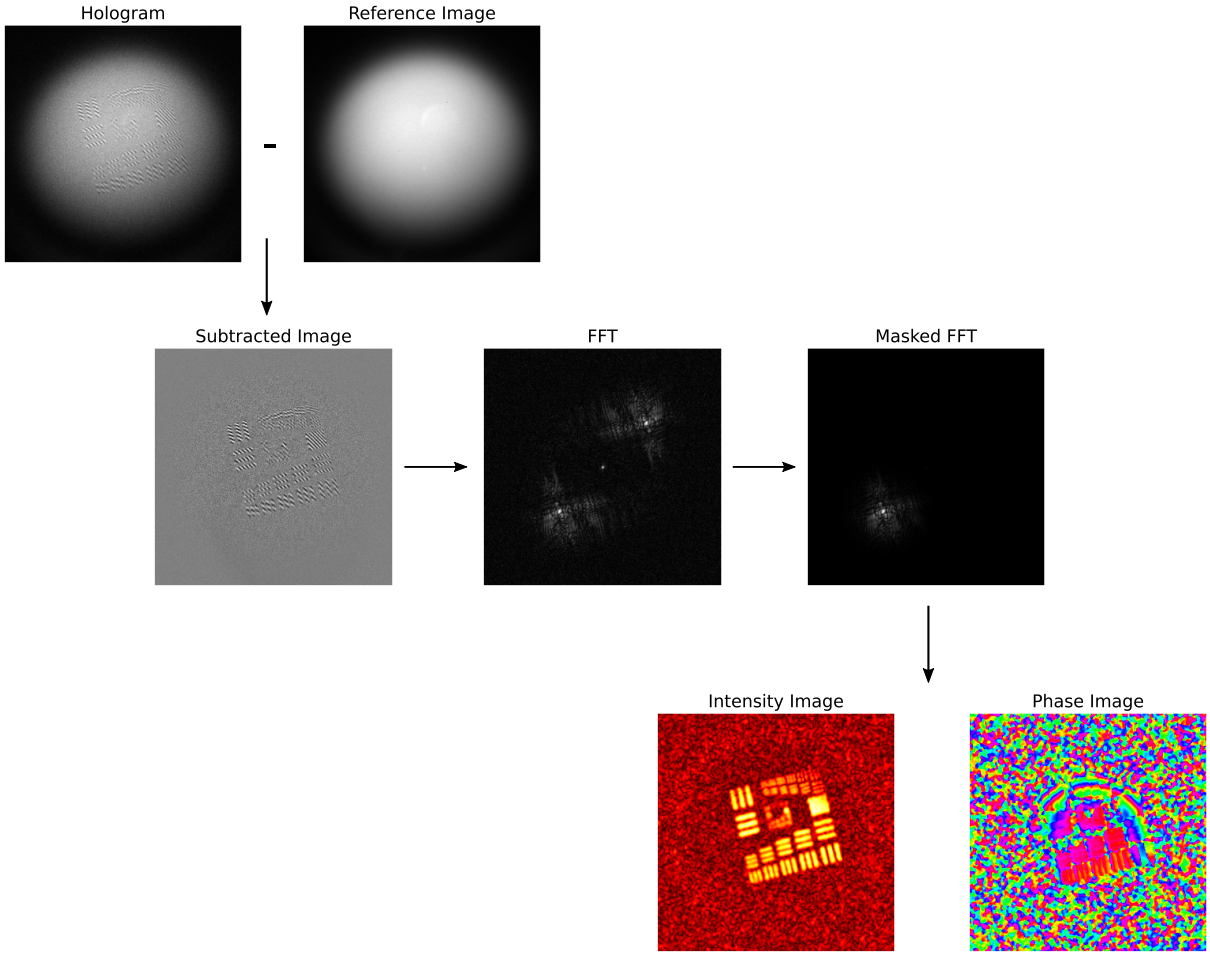

Figure 3.2: Schematic of the off-axis holographic reconstruction process. First, a hologram is obtained by interfering the object beam with a reference beam. Optionally, an image of the reference beam (shown) and in some cases the signal beam, can be subtracted to increase the SNR of the reconstructed images. A FFT of either the hologram or the subtracted image is then taken, from which a mask can be applied to select either the +1 or -1 diffracted order. An IFFT of the masked FFT then allows for a determination of the intensity and phase of the object beam.

sented in this thesis, with examples shown in Fig. 3.3. The diamond shaped mask is effective in preserving high spatial frequencies in the reconstructed images of the object, whilst the circular filter is effective at reducing noise in the reconstructed images. The Gaussian filter has similar properties to the circular filter, but has the advantage of preventing ringing, producing smoother images. Changing the area of the mask in spatial frequency space will affect the resolution of the reconstructed images, with a larger area corresponding to a higher resolution. However, increasing the size of the mask will also increase the amount of noise in the reconstructed images, decreasing the signal to noise ratio.

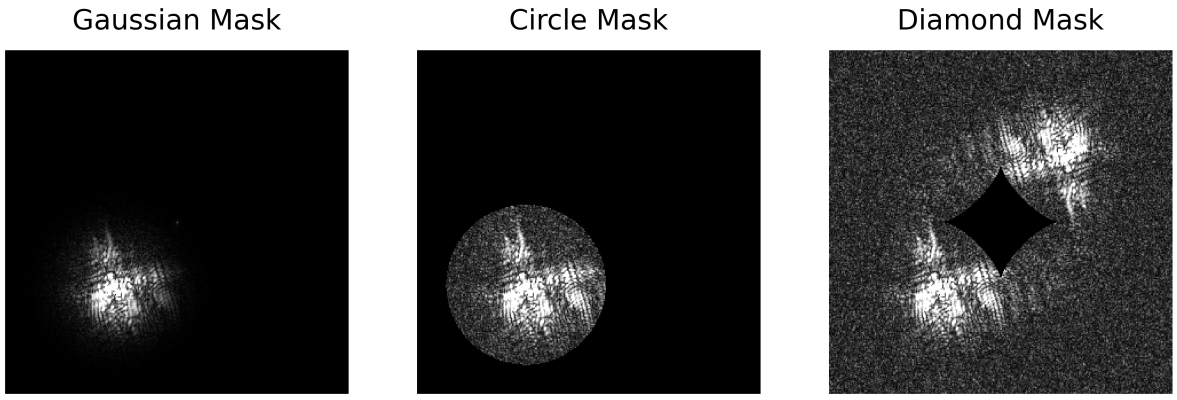

Figure 3.3: Examples of different types of Fourier filters applied to pass object spatial frequencies whilst blocking out DC components in the image reconstruction process. Shown is Gaussian, circle and diamond shape masks. Each mask has different effects on the reconstructed images.

Once masking has been applied, an inverse Fast Fourier Transform (IFFT) is taken. Assuming the correct sign of $\mathbf{k_{tilt}}$ has been chosen, the IFFT gives $E_{obj}(\mathbf{r})E^*_{ref}e^{-i\mathbf{k_{tilt}}\cdot\mathbf{r}}$. In order to determine E_{obj}, $E^*_{ref}e^{-i\mathbf{k_{tilt}}\cdot\mathbf{r}}$ must be determined. As $\mathbf{k_{tilt}}$ is a linear phase ramp, it can either be estimated from the position of the peaks in $\mathbf{k}$-space or by more sophisticated methods such as a centre of mass calculation. The conjugate of the reference E^*_{ref} can be determined from the measurement of I_{ref} and assuming that the phase of the reference beam is flat over its extent. This assumption can be met if a sufficiently large reference beam is used, and any relative phase not accounted for can be removed by additional image processing if required. Once E_{obj} has been determined, intensity and phase images can be reconstructed from the complex amplitude and phase of the object field.

3.1.3 The Paradox of Observation Without Illumination

Returning to the work of Gabor, shortly after his initial work on holography he would present an intriguing paradox in a lecture presented at Edinburgh University in 1951 which was later typed up [129]. Conceived to demonstrate why classical physics cannot provide a full description of the nature of light, 'the paradox of observation without illumination' asks the reader to imagine an object illuminated with an arbitrarily small intensity of light. Classical physics does not require any limits on the intensity of light, as the description of intensity as the square of the amplitude of an oscillating field allows for the amplitude to be decreased to any level. Gabor asks the reader to imagine a situation where this very weak field is interfered with a reference beam with a very high intensity. The resultant intensity pattern recorded is described as

$$I_{tot} = I_{obj} + I_{ref} + 2(I_{sig}I_{ref})^{1/2}\cos\phi. \tag{3.6}$$

If I_{obj} is very small compared to other terms and can be neglected, and an image of I_{ref} can be recorded on its own, such that it can be subtracted from the total intensity pattern, Eq. 3.6 reduces to just the interference term $2(I_{obj}I_{ref})^{1/2}\cos\phi$, which contains all the information needed to reconstruct an image of the object. So, by making the intensity of the reference beam large enough, it would be possible to amplify the interference term such that an image of the object could be reconstructed, even with arbitrarily low illumination.

Physical intuition suggests this cannot be true, so where has the reasoning failed? Classical physics does not provide a full description of the nature of light; in reality the energy of the electromagnetic field is quantised. This means that the light reaching the detector is detected as a series of photons. As described in Section 1.1, this series of photons will be subject to Poissonian noise, meaning there will be uncertainty in any intensities measured at the detector. In the case of observation without illumination this means an image of an object with arbitrarily low illumination cannot be reconstructed by simply increasing the intensity of the reference beam, as this will also increase the Poissonian noise on the homodyne or heterodyne signal. As such, the SNR of the signal will always be limited by the shot-noise.

Whilst it is not possible to observe an object with arbitrarily low illumination due to Pois-

sonian noise, the findings of this paradox are still remarkable. With a high intensity reference beam, a weak signal that would not otherwise be observable due to detector noise could be amplified above the noise floor by detection of the homodyne or heterodyne signal. If the homodyne or heterodyne signal is sufficiently large then the detector noise becomes negligible when compared with the Poissonian noise on the detected homodyne signal. It is interesting that Gabor came from a communication theory background; this effect is well known to radio engineers utilising homodyne or heterodyne detection and perhaps he was able to make the connection between this and his new field of holography. Similarly to his original idea of holography, the idea appears to have been left untouched for a number of years despite Gabor alluding to the fact that detector noise could be eliminated with this principle. To the best of the author's knowledge, the earliest mention within the literature in an imaging context was a demonstration of the noise advantage that Fourier domain OCT compared with time domain OCT in 2003 [130]. A full experimental demonstration of a holographic imaging method as envisaged by Gabor was shown in 2007 [131]. Perhaps the suggestion was too ahead of its time for an earlier demonstration, as when CCD technology that would be affected by electronic detector noise was introduced in the 1960s, the complexity of digital holography in an age of large, expensive computers meant it wasn't thought of as a practical solution. By the time digital holography became more practical, detector technology had likely improved to a point where digital camera noise was less of an issue in the visible regime.

3.2 Single Photon Imaging in the Shortwave Infrared with Digital Holography

In this section I present the work that formed the publication "Near single photon imaging in the shortwave infrared using homodyne detection", published in the Proceedings of the National Academy of Sciences. This paper included two collaborative authors, Prof. Gerd Leuchs and Dr. Paul-Antoine Moreau. Prof. Gerd Leuchs aided in the conception of the project, whilst Dr. Paul-Antoine Moreau had built an early version of an interferometer in the visible regime during his time in the Optics Group. Subsequent experimental work, presented in this section, was performed by myself in Glasgow.

Imaging at a low illumination level, down to a single photon per pixel, is possible with modern CMOS and EMCCD cameras in the visible regime, as discussed in Section 1.1. However, when imaging at wavelengths outside the visible region of the spectrum, the sensor architecture changes resulting in higher noise floors. An example of this is the SWIR, where the noise floor of state of the art InGaAs detectors is at least two orders of magnitude higher than state of the art visible detectors. This poses a challenge to extending the range of single-photon and low-photon illumination imaging applications to wavelengths outside the visible region of the spectrum.

In Section 3.1.3, it was described how with a high intensity reference beam it was possible to amplify a weak signal above the noise floor of the detector and additional noise present when using detectors outside the visible regime can be negated while imaging. This was demonstrated by constructing a digital holographic microscope, with a SWIR illumination source and imaging detector. The microscope, unlike a conventional digital holographic microscope which uses a balanced signal and reference beam intensity for maximal fringe contrast [132], was deliberately unbalanced to take advantage of the optical amplification effect. The weak signal is amplified by the high intensity reference beam above the noise floor of the camera, and phase and intensity images of the object can be reconstructed using off-axis holography, where the measuring of spatial interference allows for the reconstruction of intensity and phase images from a single hologram.

The method presented here shares some similarities with another coherent detection imaging method, optical coherence tomography (OCT) [133]. In OCT, a low coherence source illuminates an object, and the backscattered beam is interfered with a reference beam from the same source. This allows for intensity and depth information to be obtained from a sample when the reference is scanned through different positions. Typically with OCT there is implicitly some coherent detection gain, due to the backscattered signal having a lower intensity than the reference, and it is known that Fourier-domain OCT outperforms time-domain OCT for this reason [130], and can obtain shot-noise limited precision in the right conditions. Whilst there are many different OCT configurations which measure interference either spatially or temporally, the main difference between this system and OCT is that by measuring spatial interference with a high coherence source in an off-axis configuration allows for the measurement of intensity and phase information in a single shot. In all OCT configurations, there is some form of 'scanning', whether that be lateral movements of the reference mirror, raster scanning the sample, phase stepping measurements or sweeping the wavelength of the source. This ultimately limits the acquisition speed of any OCT application.

In terms of previous work, the coherent gain effect that can be achieved with holography has been demonstrated using a CCD to obtain images at a low detected illumination intensity and has been shown to achieve shot-noise limited precision [131, 134, 135]. However, this was performed in the visible region of the spectrum where low-noise cameras are already available. Further, a homodyne detection scheme has been demonstrated in the context of quantum imaging, by illuminating the object with the squeezed vacuum state and interfering with a classical local oscillator to image below the noise floor of the detector [136]. The authors of this work have also generalised their system to work with thermal states, measuring the mean temporal variance between the output ports of the interferometer [137]. Whilst the quantum imaging scheme can image below the shot-noise and therefore at very low photon counts, the advantage of the classical scheme here is the ability to perform real-time imaging below the noise floor from a single camera frame. Low illumination orbital angular momentum measurements have also been demonstrated using an unbalanced interferometer [138].

In the work presented in this chapter, unbalanced homodyne measurements using a digital

holographic microscope are taken in order to obtain images below the sensor readout noise in the SWIR regime. Using coherent gain due to these measurements, imaging down to a illumination intensity of ~ 1.1 photons per pixel per frame is demonstrated, around 200 times below the noise floor of the detector. With this method it is possible to recover wide-field intensity and phase measurements with measurable improved contrast over conventional images. The demonstration of the method here will help extend the range of low-light imaging applications to domains where low-noise detector technology does not exist. For example the method could be adapted to the far-wave infrared or terahertz where environmental noise and detector noise become an issue. Applications could also be found in biological and medical imaging scenarios where light radiation dose is an important consideration, with a weak probing signal amplified by a strong reference which does not interact with the sample.

3.2.1 Experiment Details

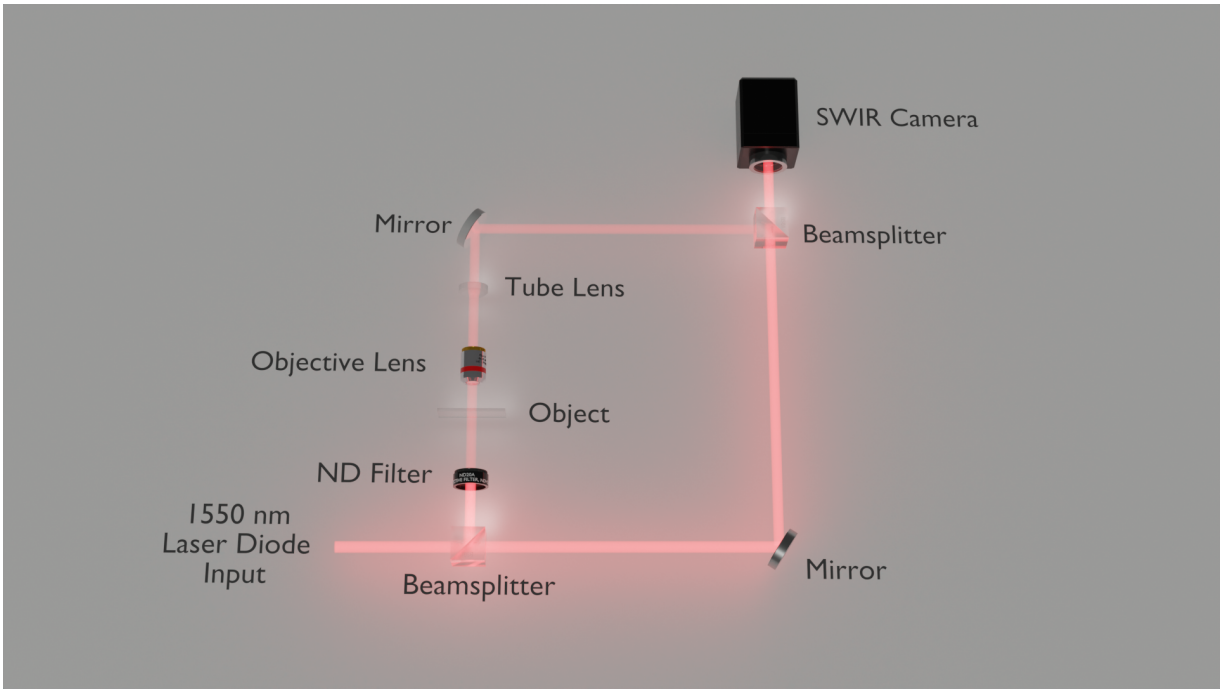

Figure 3.4: Experimental setup used to obtain off-axis holograms. A 1550 nm laser source is split into signal and reference arms using a beamsplitter, where intensity of the signal arm is attenuated by a neutral density filter. The signal arm contains the optics for an inverted wide-field microscope to image a sample, using a $\times 10$ microscope objective and tube lens. The signal and reference beams are recombined using a beamsplitter, and off-axis holograms recorded on a SWIR camera.

The experimental setup used is shown in Fig. 3.4. The signal arm of the interferometer consists of an inverted wide-field microscope, using a $\times 10$ microscope objective and a tube lens as magnification optics. The signal from the microscope arm interferes with a reference beam of much greater intensity. The signal intensity was attenuated by the use of neutral density (ND) filters. The source used is a laser diode with a centre wavelength of 1550 nm and a coherence length of 24.0 mm. The interference is then detected on a SWIR camera with a readout noise of $180e^-$ per pixel and a quantum efficiency (QE) of 85% at 1550 nm, giving an effective noise floor of 207 photons per pixel.

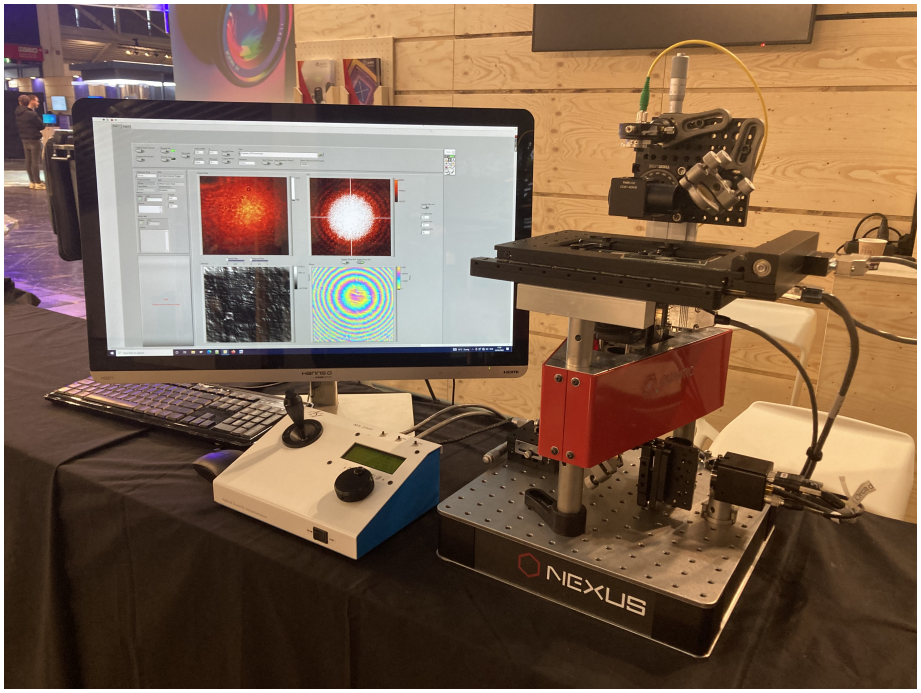

Figure 3.5: Photograph of the demonstrator system taken at Laser World of Photonics. The demonstrator included a controllable x, y, z stage for object positioning and focussing, as well as live reconstruction software and graphical user interface.

For demonstration purposes, for example at conferences, the system was built into a compact inverted microscope, with software written in LabView to perform image reconstruction in real time. The frame for the microscope was taken from an existing system, which consisted of supports for an $x-y$ translation stage to hold the sample, and a z stage to allow focusing of the image from the objective lens. A reference arm was added, along with the other optical components. The reconstruction software was capable of reconstructing intensity and phase images of a 400x400 pixel region of interest at video frame rates. Figure 3.5 shows an image

taken of the demonstrator system presented at Laser World of Photonics for QuantIC, the UK quantum imaging hub.

3.2.2 Image Reconstruction

From the imaging system off-axis holograms are recorded, from which intensity and phase images of the object can be reconstructed digitally. The reconstruction algorithm is similar to that of most digital off-axis holography methods, described in Section 3.1.2. However there are some small differences due to the unbalancing of the signal and reference beams. An intensity pattern of

$$I_{tot} = |E_{ref}|^2 + E_{obj}(\mathbf{r})E_{ref}^* e^{-i\mathbf{k}\cdot\mathbf{r}} + E_{obj}(\mathbf{r})^* E_{ref} e^{i\mathbf{k}\cdot\mathbf{r}} \tag{3.7}$$

is recorded, similar to Eq. 3.3, but where we have assumed the signal intensity I_{sig} is negligible when compared with the other terms as it is below the noise floor of the camera. In a method similar to Fatemi and Beadie [139], and the original suggestion of Gabor [129], we take an average of at least 100 frames of the reference beam alone and take an FFT of $I_{tot} - I_{ref}$. This step is necessary to suppress DC component noise in the reconstructed images. Any remaining DC contributions are subsequently masked out in the Fourier plane. After masking out the DC components, the quadrant containing the interference term is selected along with the conjugate quadrant which are averaged together. The unused quadrants are then masked, and an algorithm based on a centre of mass calculation is used to calculate the relative angle between the beams $\mathbf{k}\cdot\mathbf{r}$. The reference field can then be approximated as $\sqrt{I_{ref}}e^{i\mathbf{k}\cdot\mathbf{r}}$, allowing for a determination of the object field E_{obj}. From this the intensity and phase components of the field can be retrieved. The linearity of the grey scale between the conventional and reconstructed images was confirmed by covering half the frame with clear glass and half the frame with a ND filter and checking that the grey scale values for both the conventional and reconstructed images fell by the same amount.

The choice of mask will affect the final reconstructed images. By filtering out more spatial frequency space, the images will be more smoothed and there will be a loss of resolution. However, this will also remove more low-frequency noise from the reconstructed images. Con-

sequently, there is a trade off when deciding what mask to use. For our mask we tried two shapes as shown in Fig. 3.3; an inverted diamond centred on the DC components and circular filters (high-pass filters) centred on the cross-correlation terms. Typically the inverted diamond shape preserves more spatial frequency space whereas high-filtering returns smoother images. For the results in this work, we chose to preserve resolution with the diamond shaped mask.

3.2.3 Results

In order to determine the performance of the system a series of images of a silicon chip with deposited gold features were taken at decreasing illumination levels, as seen in Fig. 3.6. The silicon regions are transparent to light at 1550nm whereas the gold regions reflect light. The holographic reconstructed intensity images were recorded alongside their corresponding conventional images of the chip. These was taken for four light levels corresponding to an illumination level of $\sim$250 to $\sim$1 photons per pixel per frame. The holographic reconstructions are shown at two different reference beam intensities to investigate the effect of the reference beam intensity on performance. As filtering is applied to the holographic reconstructions, it was decided to show conventional images with an equal amount of filtering applied for fair comparison. A background subtraction was also applied to the conventional images to remove any ambient light effects. All images shown are taken from a single camera frame.

The photon per pixel values for the reference intensity were calculated by converting the pixel values from the camera into a number of photons using the manufacturer stated full-well capacity of the pixels and the quantum efficiency of the sensor at 1550nm. This method could not be used to calculate the signal intensity however, as the full-well capacity of the sensor meant that 1 A.D.U on the camera corresponded to 39.7 photo-electrons, meaning that for signal intensities lower than this the signal information was contained within 1 bit. Instead, the intensity ratio between the signal and the known reference intensity was calculated to obtain a value in photons per pixel in the signal beam. To do this, the manufacturer stated transmission at 1550nm of the neutral density filters was used as well as measurement of the power drop across the magnification optics in the signal beam using a power meter.

The reconstructed intensity images in Fig. 3.6 show that through the coherent gain from the

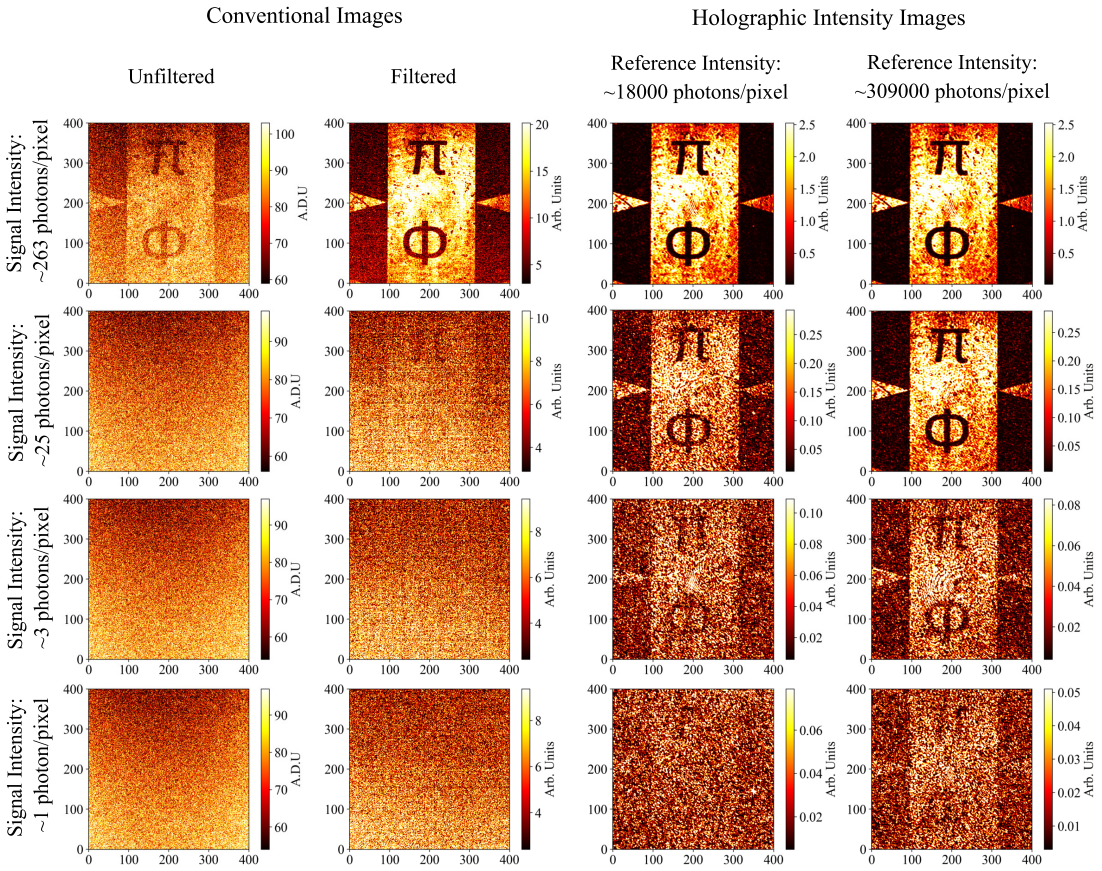

Figure 3.6: A table of conventional camera images and corresponding reconstructed holographic intensity images at decreasing illumination levels. Shown are conventional camera images at four different signal intensities incident on the camera alongside their corresponding holographic reconstructions. Images of a silicon chip with gold deposited features. The reconstructed images are shown using a low intensity reference corresponding to a detected intensity of 18000 photons per pixel and also a high intensity reference beam corresponding to an intensity of 309000 photons per pixel. Due to spatial filtering inherent in the holographic image reconstruction process, we also show conventional images with a background noise subtraction and equal degree of spatial filtering applied alongside the raw images for fair comparison. All conventional and holographic intensity image reconstructions were normalised by setting the minimum and maximum of the scale to the value of the 10^{th} and 90^{th} percentile pixel value respectively.

interference of the signal with the high powered reference beam it is possible to recover contrast in the image of the object when it would otherwise be affected by the readout noise of the camera. This is seen as a reduction of noise at higher intensities when the object is still visible in the conventional images, or even recovering features of the object when it would otherwise be obscured by noise for the lower signal intensities. The bottom row of Fig. 3.6 shows an image of the object obtained for an average signal intensity of 1.1 photons per pixel. This means that with an effective camera noise floor of ~ 207 photons per pixel, with the use of coherent gain it is possible to recover an intensity image of the object from a single camera frame at an illumination level ~ 200 times lower than the noise floor.

In order to further demonstrate the enhancement shown in Fig. 3.6 as well as show the effect of the reference beam intensity on the holographic reconstructions a series of intensity cut-throughs for the filtered conventional images and both sets of reconstructed images is shown for each illumination level in Fig. 3.7, alongside calculated contrast values. The intensity cut-throughs were calculated by averaging over columns between two sets of rows in the image with clear bright and dark regions, corresponding to rows 10 to 45 and 230 to 265. The cut-throughs were then normalised to the average value of the bright region in each cross section so that they could be displayed on the same plot. Contrast was calculated as $(I_{bright} - I_{dark})/(I_{bright} + I_{dark})$, where I_{bright} and I_{dark} represent the intensity values of the bright and dark regions of the cut-through respectively. This was calculated and averaged over 100 frames with the standard error on the mean also calculated. It can be seen from Fig. 3.7 that at the lower signal intensities the contrast is lower when using a lower reference power. This is due to the signal not being amplified sufficiently above the floor of the camera, such that the reconstructed intensity images are still noisy due to the camera readout noise.

From Fig. 3.7 it can also be seen that as the signal intensity decreases the contrast of the holographic reconstructions also decreases. Whilst the amplification effect can negate the effects of detector noise, the signal is still subject to shot noise fluctuations in the intensity. It has been shown that for a homodyne detection scheme such as ours the signal to noise ratio (SNR) is proportional to the square of the signal intensity [134]. Whilst the images are still noisy, features of the object are still visible and have measurable contrast when compared with their

Intensity Cross Sections	Image	Contrast
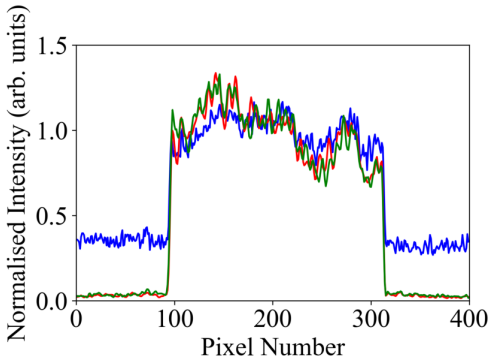	Coventional: ~263 photons/ pixel	0.4937 ± 0.0007
	Holographic High Intensity Reference	0.9484 ± 0.0003
	Holographic Low Intensity Reference	0.9387 ± 0.0002
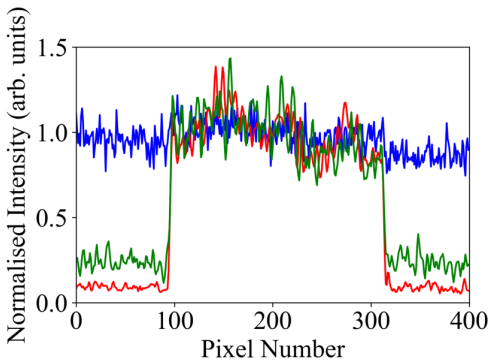	Coventional: ~25 photons/ pixel	0.0532 ± 0.0005
	Holographic High Intensity Reference	0.8411 ± 0.0007
	Holographic Low Intensity Reference	0.628 ± 0.001
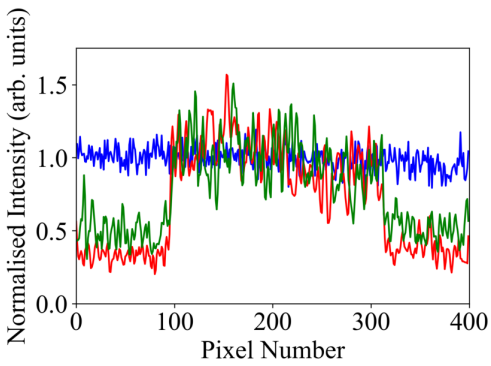	Conventional: ~3 photons/ pixel	0.0463 ± 0.0006
	Holographic High Intensity Reference	0.489 ± 0.003
	Holographic Low Intensity Reference	0.319 ± 0.001
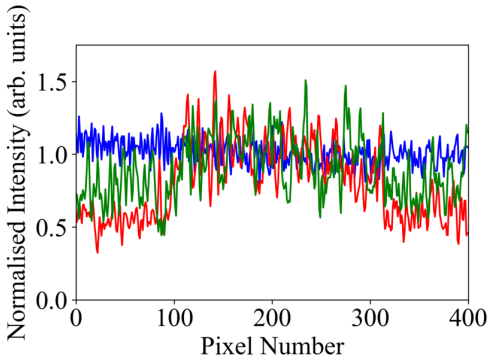	Conventional: ~1 photon/ pixel	-0.0056 ± 0.0005
	Holographic High Intensity Reference	0.293 ± 0.002
	Holographic Low Intensity Reference	0.147 ± 0.002

Figure 3.7: Image intensity cross-sections for images displayed in Fig. 3.6 alongside image contrast statistics. Image intensity cross-sections were produced by averaging image intensity over columns between two sets of rows for each image. Columns $0-400$ were averaged over between rows $10-45$ and $230-265$ to generate the intensity cross-section line plots. These plots were displayed on the same scale by normalising each to the average value of the bright regions of the cross-section, columns $100-300$. The contrast was then determined using the average value of these bright regions and the average value of the dark regions and averaged over 100 frames with the standard error on the mean calculated. The dark regions were determined by columns $0-75$ and $325-400$.

corresponding conventional images.

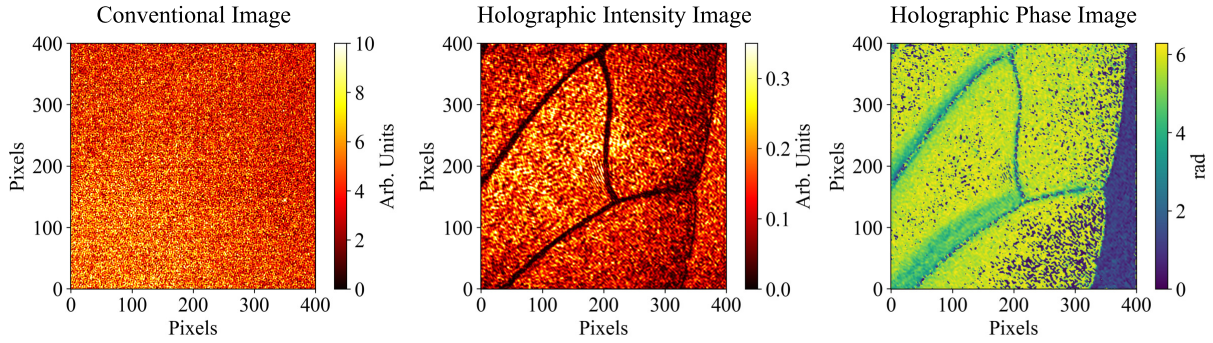

Figure 3.8: Single frame conventional camera image alongside corresponding holographic intensity and phase reconstruction images of an insect wing. The holographic intensity and phase images show features of a transmissive object can be recovered by the system when they are not visible in a conventional camera image. Furthermore, access to the phase image gives information on the optical path difference caused by the object. Note the blue portions towards the lower right of the wing showing the phase discontinuity where the optical path difference exceeds one wavelength. The intensity of the signal beam illumination incident on the camera was calculated to be $\sim$25 photons per pixel.

It is also worth noting that the system is capable of retrieving phase information from a sample below the noise floor of the detector. An image of an insect wing was used to demonstrate the imaging of an object with a complex transmission profile. Fig. 3.8 shows an image of the wing at an illumination intensity of ~ 25 photons per pixel, with the conventional image and holographic reconstructions of the intensity and phase shown. The phase image can show depth information about the sample within $2\pi\lambda$, before wrapping occurs. This can be seen in the phase image in Fig. 3.8, where some wrapping can be seen as discontinuities in the lower right portion of the wing. The access to phase measurements below the detector noise floor could be attractive in the imaging of biological and material samples as it can reveal features of the object that are otherwise not visible in the intensity profile.

With the system a loss of resolution is seen when comparing the holographic reconstructions to the conventional camera images. While the Nyquist theorem might suggest that the fundamental limit of holography systems is two pixels, in practise the optical design of microscopes to be oversampled at the detector means this limit is not reached in our system. Instead, the drop in resolution is from the masking process, which filters out some spatial frequencies in the Fourier plane. It is worth noting that this isn't inherent to DHM, however, and could be overcome by op-

tical design. If the wavevector $\mathbf{k_{tilt}}$ is large enough, then the diffracted orders can be sufficiently offset from the central DC components such that there is no overlap and no spatial frequencies are lost in the masking process. This could be achieved by using a value of $\mathbf{k_{tilt}}$ larger than the numerical aperture (NA) of the optical system, in our case the NA of the objective lens divided by the magnification. With our system, using a low magnification (x4) microscope objective, we cannot achieve a value of $\mathbf{k_{tilt}}$ larger than the NA at the detector. This could be achieved by using a higher magnification objective or a camera with a smaller pixel pitch, and it should be possible to reconstruct images without the drop in resolution observed.

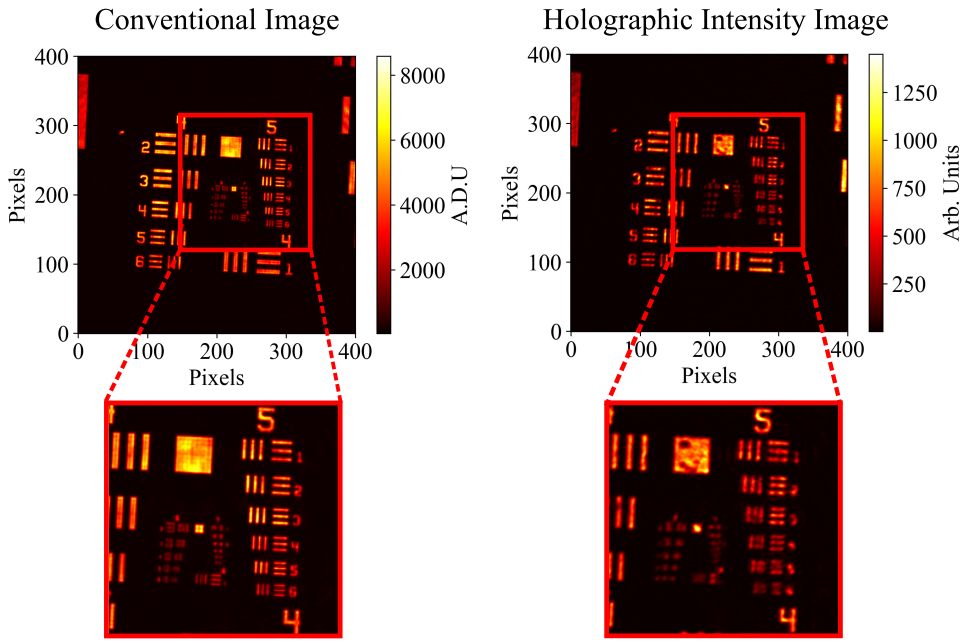

Figure 3.9: Images of a USAF resolution target from the conventional camera image and reconstructed holographic intensity image. It can be seen that in the conventional camera image the smallest resolvable element is 1 in group 6 (largest element in the lower left of inner square), whilst for the holographic image it is element 4 of group 5 (4th element down on right hand side). This corresponds to a loss in resolution of 29.2% when images are reconstructed using the holographic method when compared with what could be achieved with a conventional camera image.

The resolution loss for the filtering performed in this experiment was quantified with the use of a USAF resolution target imaged and the conventional and reconstructed holographic intensity images compared. This can be seen in Fig. 3.9, which shows element 1 of group 6 is resolvable for the conventional image, giving a resolution of 64.0 lp mm^{-1} (line pairs per millimeter). We see in the corresponding holographic intensity reconstruction that element 4 of

group 5 is the smallest resolvable element, giving a resolution of 45.3 lp mm^{-1}. This means with the filtering implementation for the results presented here there is a 29.2% drop in the resolution of the holographic reconstructions when compared with their conventional images.

3.2.4 Discussion

Presented in this chapter is a holographic imaging method which is capable of reconstructing intensity and phase images of an object at signal intensities below the noise floor of the camera. It was possible to measure contrast in an image of the object down to a signal illumination of ~ 1.1 photons per pixel per frame, despite the camera having a noise floor 200 times higher. This is possible due to homodyne detection amplifying the signal before the photoelectric conversion process at the detector. A 29.2% drop in resolution was observed but it has been discussed that this could be avoided by the optical design of the imaging system.

The intensity of the reference beam was identified as a key parameter to the performance of the system, with a lower reference intensity leading to decreased contrast in the reconstructed images. Due to this, the dynamic range of the detector used is an important consideration when designing a system to utilise coherent gain. The results presented here were obtained with a camera with a dynamic range of 72 dB, which allowed a maximum ratio between reference and signal of 300,000:1.

With the ability to image down to an average signal intensity of ~ 1 photon pixel in a regime where the detector noise is much higher the imaging scheme could extend the range of single-photon and low-light imaging schemes to other regimes where low noise detectors do not yet exist. This could be at UV wavelengths for example, or further into the infrared. Another regime where detector noise is high is high-speed imaging, with cameras operating at kHz frame rates often having high noise floors compare to those operating in the SWIR.

3.3 Stand-off Speckle Holography Below the Noise Floor

This section describes the results which formed the basis of the publication "Low photon-number stand-off speckle holography at kHz frame rates" published in Optics Continuum. This work was the result of exploring whether the previous demonstration of imaging below the detector noise floor could be applied to a stand-off detection setting.

When using active illumination in a stand-off detection setting, imaging can be challenging as the intensity of the backscattered light decreases with the square of the distance to the target. Some examples of stand-off imaging applications requiring active illumination include imaging through scattering media such as fog or water [6, 7, 140] and imaging systems for autonomous vehicles [5]. In some situations, it may not be appropriate to simply increase the illumination flux to increase the backscattered signal reaching the detector, such as applications where eye-safe illumination is required or if the imaging is covert in nature. If using an array detector with a high noise floor, such as those designed to image at kHz frame rates or IR wavelengths, these issues are especially apparent as the high noise floor limits the achievable SNR of the detection of the backscattered signal.

In the previous section, an imaging scheme utilising homodyne gain was shown to be capable of imaging below the noise floor of a noisy detector. Digital off-axis holography, a form of homodyne detection was used to reconstruct intensity and phase images from the interference of the weak signal with the high intensity reference beam. Despite the widespread applications of digital holography within closed interferometer setups, there have been fewer demonstrations of stand-off holography systems, owing to the experimental complexity of recording interference within the returned speckle pattern from optically rough surfaces. More typically, stand-off interferometric detection would be performed by spatially filtering the speckle pattern to select a single speckle, which is an inherently inefficient process. Stability of the interferometer over long distances can also prove a challenge, especially if long exposures are necessary due to the low return signal. An example of stand-off holography is electronic speckle pattern holography (ESPI), a technique developed in the 1970s used to measure the displacement of an optically

rough surface, where two holograms of the object are subtracted to give an image showing the phase variation of the displacement as fringes in the subtracted image. More recent demonstrations of stand-off holographic imaging include imaging through fog and fire [141,142]. Intensity correlation holography has also been proposed as a method for stand-off holographic detection which removes the need for phase-stability between signal and reference, allowing long exposures [143]. Doppler holography is an example of high-speed stand-off holographic imaging, where holography is used to perform Doppler measurements on backscattered light from tissue. There have been several demonstrations performing Doppler holography to image retinal blood flow in low-light, eye-safe conditions for ophthalmology [144, 145].

There have also been several demonstrations of measurements of vibrational motion of a remote surface using high-speed holography. Redding et. al performed off-axis holography on the returned speckle pattern from a remote surface to obtain full-field phase measurements of vibrational motion, showing a $\sqrt{N}$ pixel advantage in SNR when compared to a single pixel method [8]. In another demonstration, Verrier et al. demonstrated a sideband holography method capable of shot noise limited detection to measure vibrations on the scale of 0.01 nm [146]. Another method of measuring the vibrational motion of a remote surface is by using speckle tracking methods, where a high speed camera is used to measure the change of the speckle intensity pattern as the surface vibrates. Zalevsky et al. measured acoustic signals from various targets up to a range of 30 m using this method [147]. Similarly, Cester et al. measured human heartbeats by tracking the speckle pattern returned when a laser was directed at the persons throat, using eye-safe illumination at a range of 2 m [148].

In the work presented in this chapter, the intensity imaging capability of the system is demonstrated, where intensity images of a target at a range of 2 m were reconstructed, down to an average signal intensity of ~ 1 photon per pixel per frame at 50 kHz. The performance of the system in relation to measuring the vibration of a remote surface is then investigated, showing that vibrational motion can be measured even when the speckle pattern is below the noise floor of the detector. This method could be applied to the interferometric methods of vibrational sensing outlined above, or those which rely on speckle tracking, such that they are no longer detector noise limited. This could increase the range at which vibrational sensing systems could operate,

especially systems with eye-safe illumination requirements limiting laser power output.

3.3.1 Imaging System

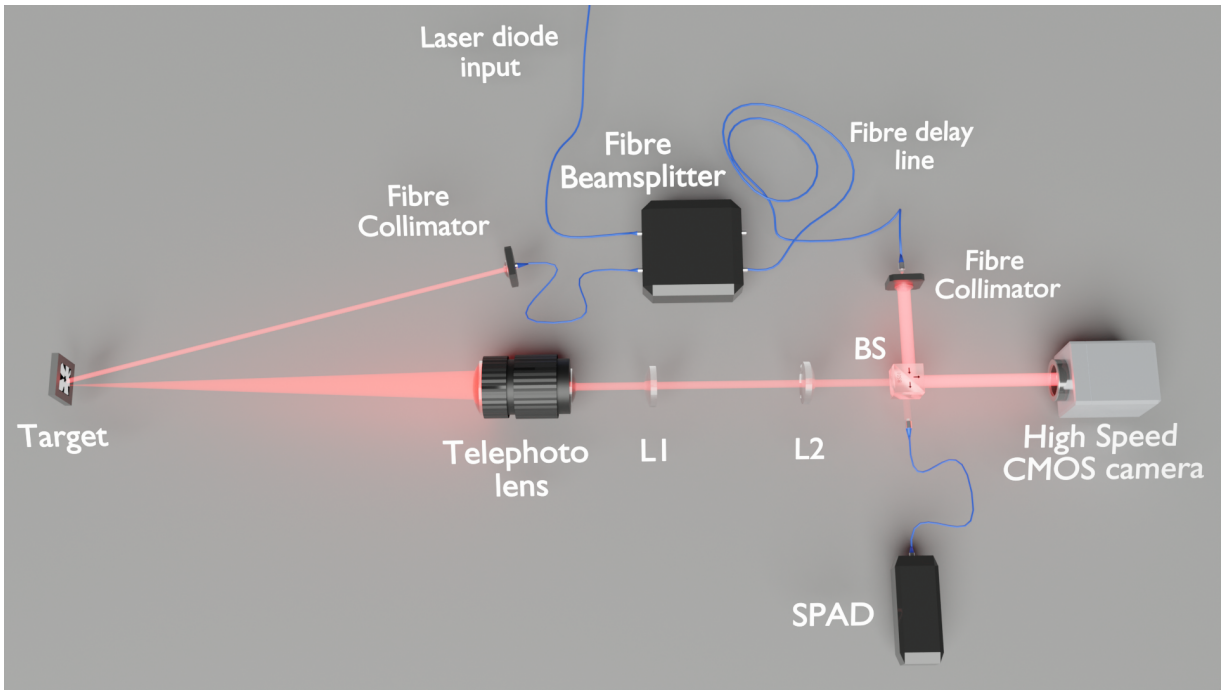

Figure 3.10: The experimental setup used to perform off-axis holographic imaging of a remote target. A laser diode is coupled into a fibre beamsplitter, with the signal arm coupled to a fibre collimator and directed at the target. The light backscattered from the target imaged by a telephoto lens, which is then re-imaged by lenses L1 ($f = 16\,\text{mm}$) and L2 ($f = 120\,\text{mm}$) to magnify the resulting speckle pattern on the detector array, such that multiple fringes can be recorded within a speckle grain. The light from the target is then interfered with the collimated light from the other output of the fibre beamsplitter, forming the reference arm of the interferometer. The interference pattern is then imaged onto the high speed detector array. A single-mode fibre coupled to a SPAD is used to measure the illumination intensity to calculate the number of photons per pixel incident on the high-speed detector.

The experimental setup used is shown in Fig. 3.10. It consists of a laser diode at 785 nm chosen for its coherence length of $\sim 6\,\text{m}$, which is split by a fibre beamsplitter into a signal and reference arm. The signal beam is collimated and directed at the target, whilst the reference is sent through a fibre delay line to maintain coherence between the signal and reference beams over the distance travelled by the signal beam to the target. The backscattered light from the target is imaged by a telephoto lens. For an extended source, the feature size of the speckle pattern formed on the detector solely depends on the wavelength and the numerical aperture (NA) of the imaging lens. To ensure interference can be recorded, it is necessary that the feature

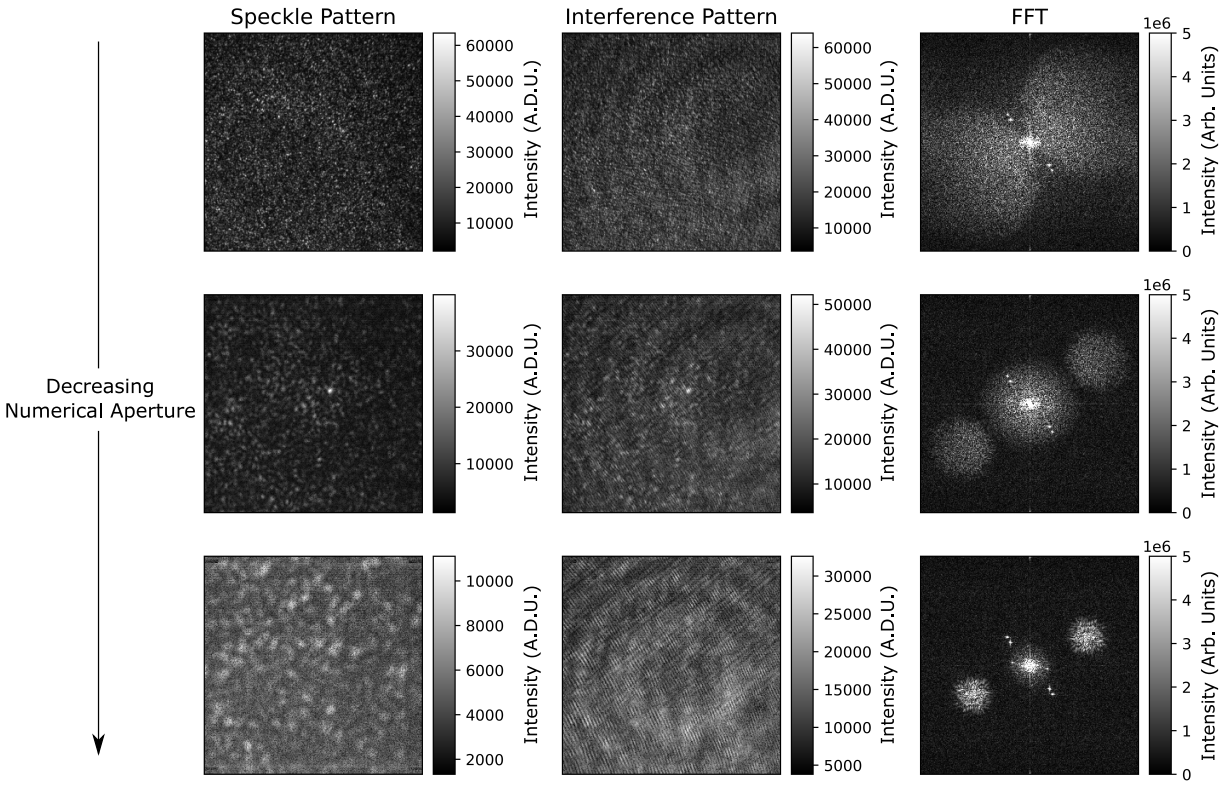

Figure 3.11: Examples of different sizes of speckle recorded on the camera, along with interferograms and FFTs of the interferogram, obtained by changing f-number of the telephoto lens which alters the numerical aperture. To ensure sufficient separation of $+1$ and -1 diffracted orders from the DC components in spatial frequency space, the speckle must be large enough that each bright speckle covers many pixels, reducing the extent of $+1$ and -1 orders.

size of the speckle is large enough such that there are a sufficient number of camera pixels within each speckle that the interference fringes can be resolved. Furthermore, the reference beam must also be brought in to interfere with the signal beam at angle which is larger than the NA of collection lens. It was found that meeting these conditions was not possible with the telephoto lens alone, as the speckle pattern needed to be magnified further and the focal length of the lens was not sufficient to place a beamsplitter between the lens and camera sensor. As such, lenses L1 ($f = 16\,\text{mm}$) and L2 ($f = 120\,\text{mm}$) were used to magnify the resulting speckle pattern onto the camera sensor, also allowing for the positioning of a beamsplitter before the camera. An adjustable iris within the telephoto lens also allows for control of the f-number to change the size of the speckle on the camera, as is demonstrated in Fig. 3.11. Figure. 3.11 shows in the top row that the scale of the recorded speckle pattern is too small, and the extent of the $+1$ and -1 diffracted orders in spatial frequency space are too large to sufficiently separate the diffracted orders from the DC components, which would lead to poor reconstructed image contrast. The array detector used to record the interferograms is an iX i-speed 509 high-speed camera, capable of recording a 256×256 pixel region of interest up to 50 kHz. The high readout speed typically introduces a large amount of readout noise however, and as such high-speed cameras have a high noise floor when compared to cameras designed to operate at video rates in the visible region, with the detector used in this work having a readout noise of approximately 50 photoelectrons per pixel.

In order to measure the signal illumination in terms of a photon number, a SPAD connected to a single mode fibre was placed in the other exit port of the beamsplitter, as shown in Fig. 3.10. By measuring the number of photons entering the fibre, the number of photons per metre squared was calculated using the known diameter of the fibre, which was then converted to a number of photons per pixel per frame.

Intensity and phase images of the speckle pattern from the object were reconstructed using the standard off-axis digital holography techniques described in this chapter, where an average image of the reference beam was subtracted from the speckle hologram to improve the SNR of the reconstructed images. After a FFT of the subtracted interferogram, a high-pass Gaussian filter was applied to the select one of either the $+1$ and -1 diffracted orders, and a linear phase

ramp applied to correct for the k-vector between the signal and reference beams.

3.3.2 Results

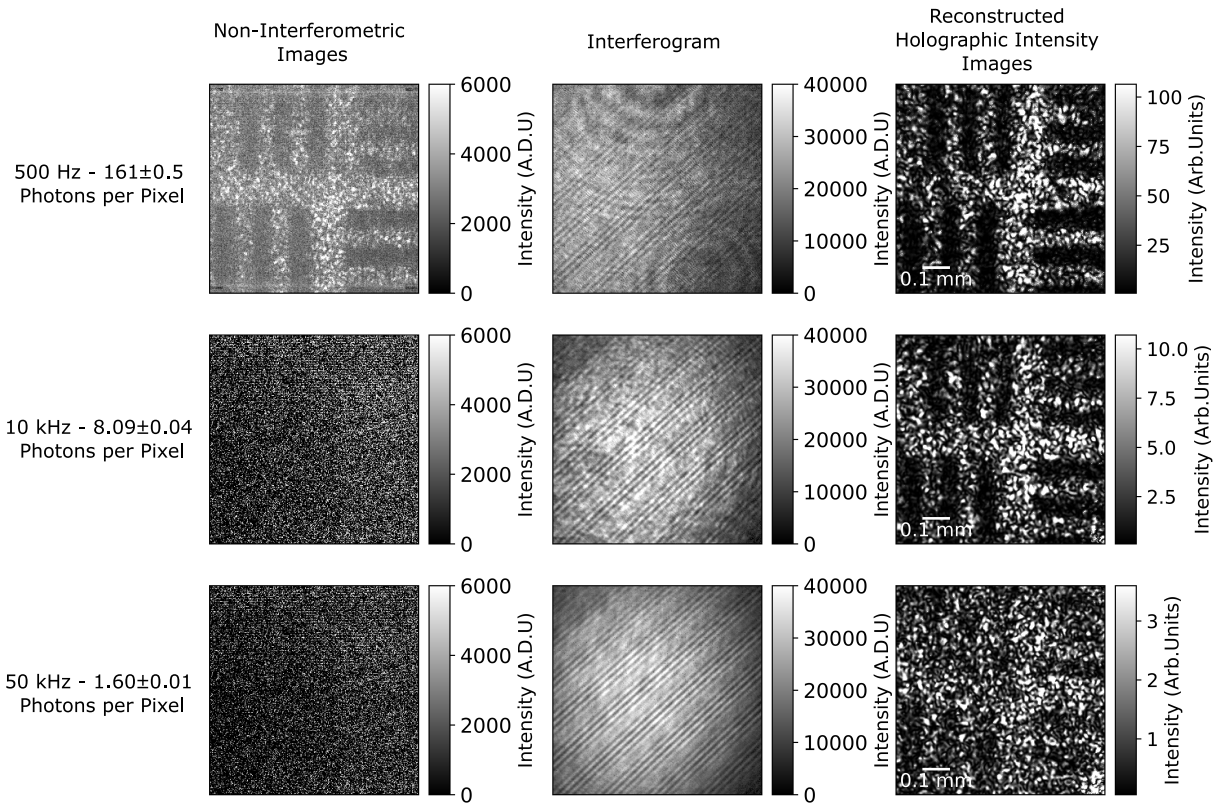

Figure 3.12: Series of non-interferometric signal images of a USAF resolution target obtained by the imaging system along with corresponding holographic reconstructed intensity images at increasing frame rate. As the exposure time decreases, so does the photon-number flux detected at the camera as measured by the SPAD detector. As the illumination incident on the camera is decreased, the object becomes obscured by readout noise. However, in the holographic reconstruction images, image contrast is largely maintained down to a detected intensity of ~ 1 photon per pixel per frame.

The intensity imaging capabilities of the system under low-light conditions were explored by acquiring a series of images of a USAF resolution test target whilst increasing the frame rate, with the corresponding decrease in exposure time limiting the light from the target recorded on the sensor. The reference beam was kept constant across the different exposure times with the use of neutral density (ND) filters. The USAF test target was printed on card with a high resolution printer to give a target that would produce specular reflections. Images of the signal with the reference beam blocked are shown alongside their corresponding holographic reconstructions in

Fig. 3.13. As the exposure time decreases, and the detected signal is lowered below the noise floor of the camera, it can be seen for the non-interferometric images with signal blocked that the image contrast becomes lost within the noise floor of the camera. However, image contrast is largely maintained in the holographic intensity reconstructions, with features of the USAF target still visible, down to an average detected signal intensity of 1.60 ± 0.01 photons per pixel per frame due to the amplification of the signal through coherent detection with the high intensity reference beam.

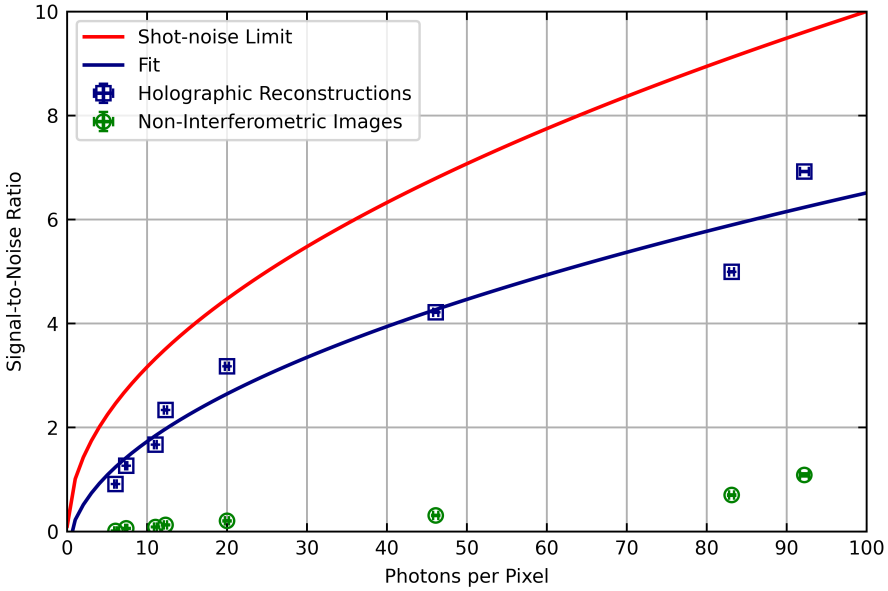

Figure 3.13: Signal-to-noise ratio against detected intensity in photons per pixel per frame for a series of non-interferometric images and their respective holographic reconstructions. Also plotted is the shot-noise limit for reference. Whilst the SNR of the non-interference signal images is rapidly overcome with detector noise, the SNR of the holographic reconstructions remains higher due to the amplification through interference. A $1/\sqrt{N}$ fit of the data points for the holographic reconstructions shows the SNR approaches shot-noise limited sensitivity within a factor of 0.70 ± 0.07.

Under the right conditions, coherent detection can achieve shot-noise limited measurements of a signal. To investigate the noise performance of the system, the signal-to-noise ratio of a series of images, calculated both for non-interferometric images and their corresponding holographic reconstructions. The SNR was calculated by acquiring images of knife edge, defining bright and dark regions from which the signal and noise statistics were calculated. The camera frame rate was held at a fixed frame rate of 1 kHz to prevent any differences in detector noise from increased readout speed from affecting noise statistics, with the signal intensity varied with

the use of neutral density filters instead. Figure 3.13 shows the SNR for both non-interferometric images of the signal, and their corresponding reconstructed holographic intensity images plotted against the detected number of photons per pixel, N, which was calculated from the SPAD channel. Also plotted is the shot-noise limit, defined as $N/\sqrt{N}$, for comparison. The reconstructed intensity images have a higher SNR than the non-interferometric images, as the detector noise is no longer the dominant noise contribution. The imaging system approaches shot-noise limited detection of the signal within a factor of 0.70 ± 0.05. The reason for the difference is likely due to temporal variations in the reference intensity, which cause fluctuations in the the DC components of the reference subtracted interference pattern, which introduces noise into the reconstructed images.

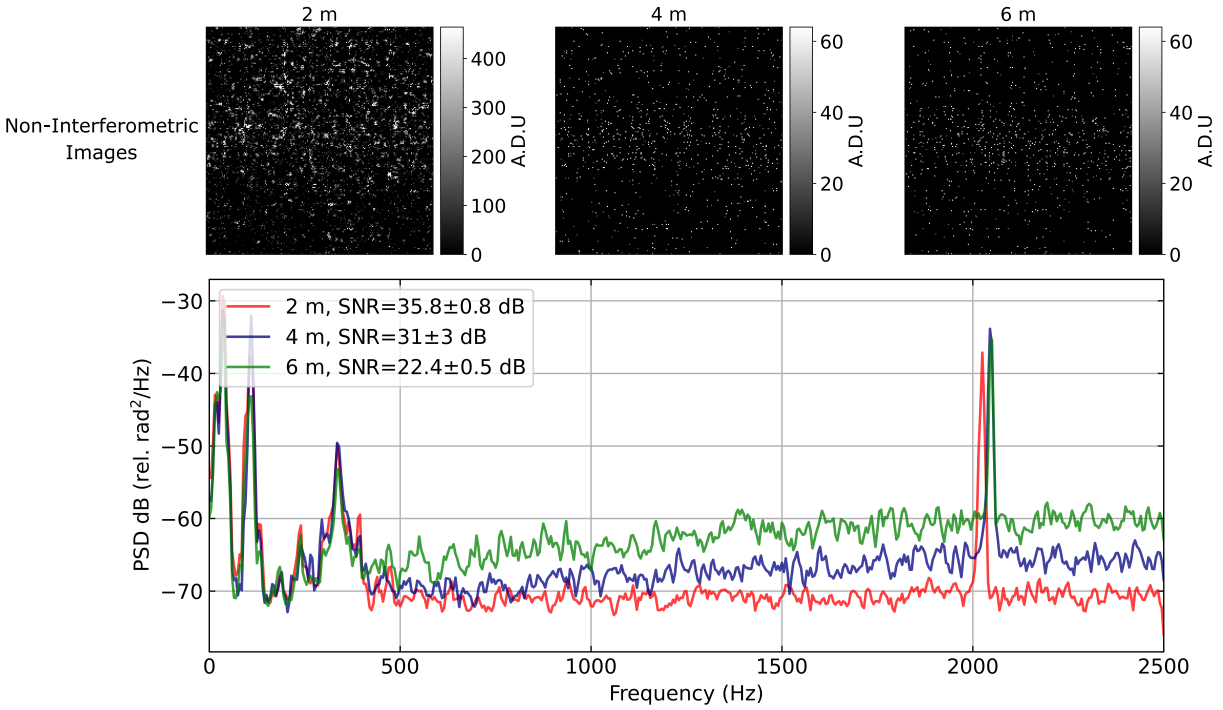

Figure 3.14: Power spectral density plots for a vibration signal of 2 kHz measured from the piezo at different ranges. Also shown are examples of the non-interferometric images at each distance. It can be seen that whilst the returned signal collected on the camera falls beneath the noise floor at 4 m, it is still possible to measure the vibrational signal through amplification by interference with the high powered reference beam. Note that the difference in frequency of the peaks is due to drift on the function generator used to drive the piezo.

Recording the interference pattern of the backscattered light with the reference beam also allows for a reconstruction of a phase image of the speckle pattern. This allows for the stand-off detection of vibrational motion, up to the Nyquist frequency of the frame rate of the camera, by

recording the phase of successive speckle patterns as the target vibrates. As long as the phase difference between successive frames does not exceed 2π, then the average phase difference can then be plotted against time to construct a vibrational signal of the surface. To investigate how the system performs as a stand-off vibrational sensor, a piezo speaker was attached to the back of a scattering imaging target, and a tone at a constant frequency of 2 kHz was played. A series of interferometric images of the returned speckle pattern were then recorded at a frame rate of 5 kHz, from which phase images were then reconstructed and a time series of the average phase difference calculated. This was repeated with the vibrating target placed at increasing distances from the collection lens, from a distance of 2 m to 6 m. At the longer distances from the collection lens, the detected backscattered light falls below the noise floor of the detector. Figure 3.14 shows examples of the non-interference images of the speckle pattern returned from the target, as well as the power spectral density (PSD) calculated using Welch's method [149] for each reconstructed waveform. It can be seen from Figure 3.14 that at all ranges tested the system is capable of recovering the vibrational signal, despite the intensity of the backscattered light being below the noise floor of the detector at ranges greater than 4 m. As the target is moved away from the collection lens, the noise floor of the vibrational sensing system increases. The phase noise on each pixel of can be calculated as [8, 150]

$$\Delta\phi = \sqrt{\frac{2h\nu\Delta f}{V^2\eta P}}, \tag{3.8}$$

where h is Planck's constant, ν the optical frequency, Δf the noise equivalent bandwidth, V the fringe visibility and P total power reaching the detector. As the target is moved from the collection lens, both the total power reaching the detector and the fringe visibility drop as the intensity of the backscattered signal reaching the detector decreases. At a range of 6 m, it was possible to measure a signal with a SNR of 22.4 ± 0.5 dB, using an illumination source with a power of 2.2 mW.

The recording of more complex vibrational systems was also explored, where a speaker was positioned behind the target and audio played. Figure 3.15 shows a spectrograms of a recording of speech played on the speaker, alongside a spectrograms of the audio file played

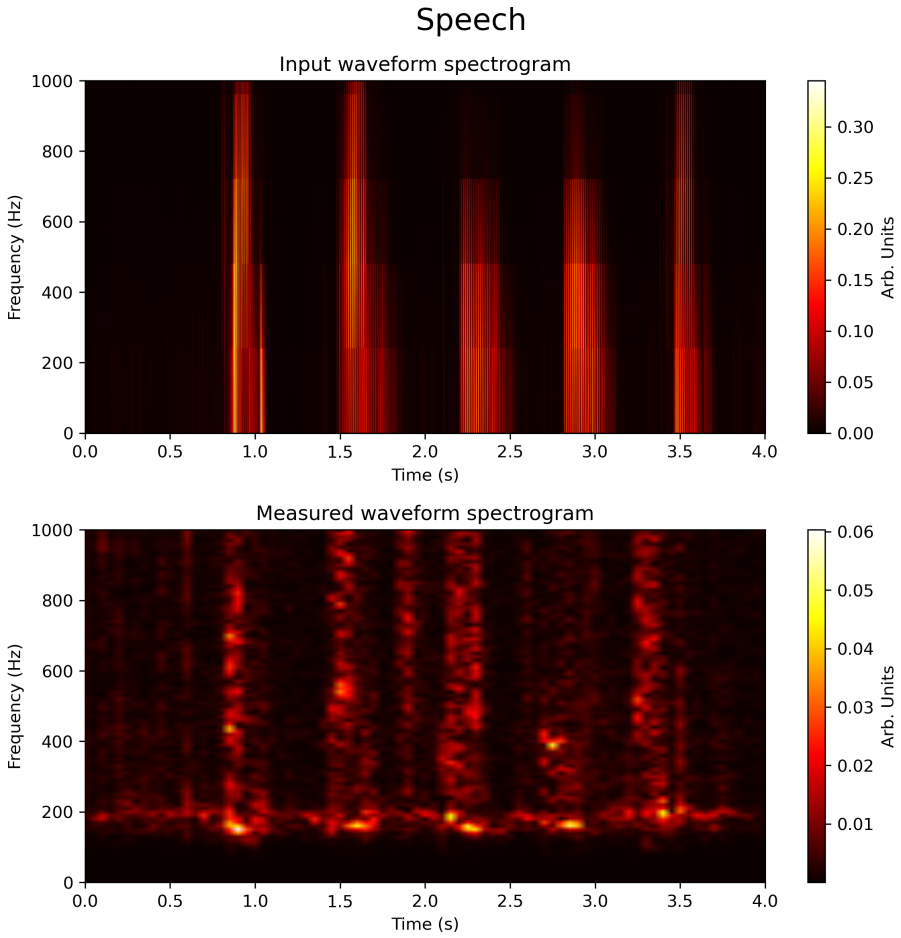

Figure 3.15: Example spectrogram of more complex vibrational signal. A recording of human speech was played on a speaker behind the target surface, and a spectrogram of the signal from the system is shown alongside the spectrogram of the input audio file for comparison.

on the speaker, recorded at a range of 2 m. Whilst it was possible to reconstruct such signals under these conditions, the recording of stand-off vibrational signals in this manner is more complex, due to considerations of the frequency response of the material the backscattered light is collected from.

3.3.3 Discussion

In this section, a full-field, stand-off off-axis holography system acquiring images at kHz frame rates was demonstrated reconstructing intensity and phase images under the condition if a low return signal collected at the detector. With such a system, intensity and phase images of the returned speckle pattern can be recovered, even when the signal is below the noise floor of the detector. The recovery of intensity images was demonstrated down to a signal intensity of 1.60 ± 0.01 photons per pixel per frame, upto a frame rate of 50 kHz. The noise performance of the system was analysed, which showed the system approaching shot-noise limited detection within a factor of 0.70 ± 0.07. With the applications of stand-off holographic detection becoming more widespread, performing sensitive interferometric measurements with coherent detection will help extend the applicability of these schemes to low photon flux scenarios where the backscattered signal may fall below the noise floor of the detector.

The system was also demonstrated to be capable of performing vibrational sensing measurements which are not detector noise limited, which would typically be the case when using a high speed camera under the conditions of the low photon flux at the detector. A single frequency tone was measured with a SNR of 22.4 ± 0.5 dB, at a range of 6 m, using an illumination power of 2.2 mW. This level of performance was despite the intensity of the backscattered light falling below the noise floor of the detector. This demonstrates the possibility of such a method being used to help extend the distance at which vibrational sensing can be performed with an array detector, without the need to increase the illumination power. This could be especially useful in cases where it is not possible to increase illumination power, such as systems which require eye-safe illumination. The sensing of more complex vibrational signals was also demonstrated.

It is an interesting point of discussion that in the experimental setup used in this experiment, a fibre delay line was used to maintain phase stability between the signal and reference beam when

the round-trip distance to the target exceeded the coherence length of the laser ($\sim 6\,\mathrm{m}$). However, in order to observe interference the phase stability only needs to be maintained over the exposure time of the camera. As cameras with very short time resolution are now available, interference could be observed even if the round-trip distance exceeded the coherence time of the laser, as has been demonstrated in a similar method based off intensity correlation holography [143]. Using a laser with a very narrow linewidth in conjunction with a camera with very short time resolution could allow stand-off speckle holography to be performed over very long distances.

Chapter 4

Holography for Imaging with Undetected Photons

4.1 Imaging with Undetected Photons

In addition to the many quantum imaging experiments that use correlations between photon pairs, there have been many other quantum imaging schemes which instead look to utilise quantum interference effects for an advantage of classical imaging. Perhaps the most well researched of these are so called non-linear interferometry or imaging with undetected photons imaging systems. These systems, as many other quantum interference imaging schemes, are based on the pioneering work into quantum interference by physicists at the University of Rochester in the 1980s and 1990s [151, 152]. In 1991, the group of Leonard Mandel published work on the interference of photons emitted from parametric downconversion, which they called induced coherence without induced emission [153, 154]. In this work, a sketch of which can be seen in Fig. 4.1, two downconversion crystals were pumped with mutually coherent pump beams, producing signal and idler pairs at 788.7 nm and 632.8 nm respectively. The crystals were aligned such that the idler mode i_1 from the first downconversion crystal overlapped with the second idler mode i_2 from the second crystal. The signal beams from the first and second crystal s_1 and s_2 were then combined at a beamsplitter, where the signal count rate was measured by detector D_s. The idler count rate was also measured by detector D_i.

Interference was seen in both the coincidence rate R_{si} and the counting rate R_s, when the idler beams were within the coherence length of the signal beams. If the intensity of the down-conversion was large, then it would be expected that i_1 would induce downconversion in the second crystal NL2. In this case, the fields i_1 and i_2 would be mutually coherent and necessitate that s_1 and s_2 were also mutually coherent and interference would be seen. However, interference was still seen when the intensity of the downconversion was weak, such that emission from NL2 was spontaneous. Also remarkable was that if a phase shift was added to the idler arm, the interference present in the signal counting rate R_s would modulate according to that phase shift, without having to measure the idler photons in coincidence.

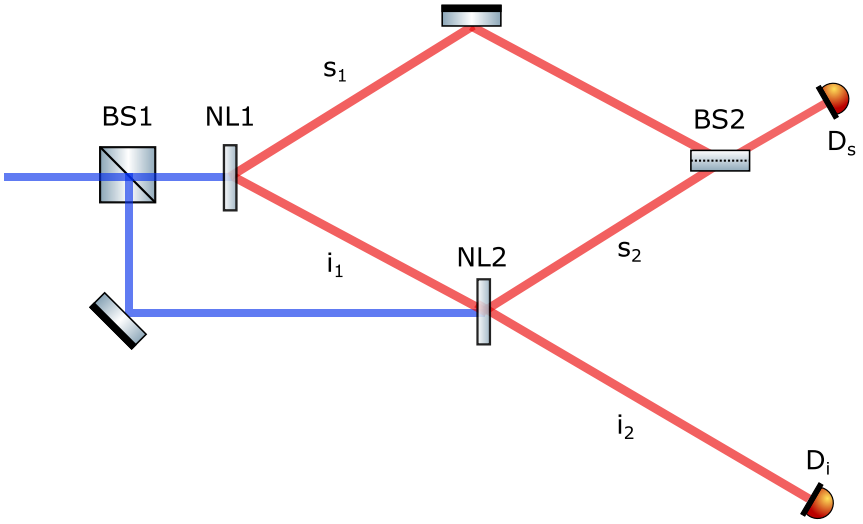

Figure 4.1: A sketch of the original induced coherence without induced emission experiment, presented in Refs. [153, 154]. A mutually coherent pump beam pumps non-linear crystals NL1 and NL2, producing signal and idler pairs s_1, i_1, s_2 and i_2. If the crystals are aligned such that photons emitted into mode i_2 overlap with idler emission i_1 from the first crystal NL1, when the signal beams are combined at the beamsplitter interference will be seen in the counting rate $R_s i$ and R_s.

The interference in the coincidence rate R_{si} without induced emission was explained by the indistinguishability of the photon pairs from either crystal. As it is not possible to determine whether a coincidence count was caused by a photon pair from the first or second crystal, the outcomes are indistinguishable, and the probability amplitudes must be added together and squared, leading to the observed interference. Blocking the idler path i_1 causes a loss of interference as it is then possible to determine that the coincidence must have been from a photon pair emitted from the second crystal. If efficient detectors are used, such that every signal photon detected is

accompanied by and idler photon, the idler detector D_i is no longer necessary, and interference will be seen in the count rate R_s alone. The idler beam i_1 is said to be inducing coherence in the signal beams without any additional emission. The explanation of the loss of interference when an object is placed in the path of i_1 without the detector D_i present is more subtle however. At first, it may appear that there is still no way of knowing which crystal the detected photon was emitted from the measurement of R_s. However, the outcome indistinguishability relies not only on what is measured, but what is *in principle* measurable from the system. Consider that i_1 is blocked and D_i were reintroduced such that a coincidence between D_s and D_i is measured. This means that the photon measured at D_s must have come from the second crystal, as the idler path in the first is blocked. Even the possibility of knowing the which way information is enough to destroy the interference seen in R_s, even if the coincidence rate R_{si} is not measured, or the idler detector D_i is not present at all.

In 2014, Lemos et al. would extend this work to devise a full-field imaging scheme based on induced coherence without induced emission, and use a crystal with greater non-linearity to image an object with 1550 nm idler photons, but only detecting signal photons at 810 nm [155]. A sketch of the setup is shown in Fig. 4.2. In order to exploit the effects of induced coherence without induced emission for full-field imaging, the momentum anti-correlations between signal and idler in type-0 downconversion were used. By placing the camera and object in the far-field of the downconversion crystals, there is a point by point correspondence of the spatial modes from the object plane to the array detector. This allows a transmission image of the object to be measured by subtracting the constructive and deconstructive interference images from either output of the beamsplitter. In a similar manner to ghost imaging, the method was proposed as a solution to imaging at wavelengths at which suitable detector technology, for example in terms of noise performance, does not exist. Unlike ghost imaging however, the method does not rely on coincidence measurements of photon pairs, meaning that higher illumination levels can be used, as single photons do not have to be detected. This means much shorter acquisition times can be used in so called imaging with undetected photon schemes compared with the typically long acquisitions for ghost imaging.

Since this full-field imaging demonstration using non-degenerate downconversion, there

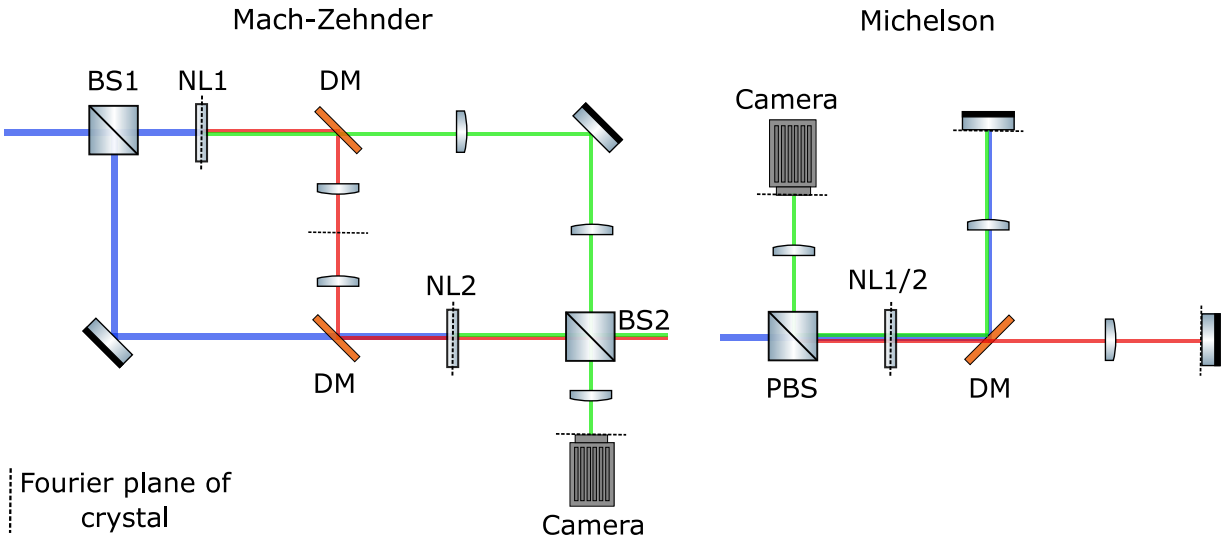

Figure 4.2: Diagram showing two common configurations of imaging with undetected photons experiments. The Mach-Zehnder layout was the original used by Lemos et. al. [155]. Subsequent experiments have used the folded Michelson layout, where NL1 and NL2 are the same crystal, with the pump reflected back with the signal photons. In both layouts, a series of lenses are used to image the Fourier plane of the crystal onto the object and camera.

have been numerous extensions of the technique to perform imaging and sensing with undetected photons. Phase shifting holography techniques have been implemented to allow phase as well as transmission images to be obtained from the object placed in the idler arm. There have also been several demonstrations of microscopy with undetected photons, either through the use of further magnification optics when the object is placed in the far-field of the crystal, or by placing the object in the image plane of the crystal where the position correlations between signal and idler allow for higher resolution imaging [156, 157]. Microscopy with undetected photons has been applied to fabrication quality control and biological imaging. Optical coherence tomography with undetected photons has also been demonstrated, using the low coherence of the downconverted photons and scanning the signal mirror to construct 3D scans of a sample [158, 159]. Numerous studies have also utilised the broadband nature of the emitted photons from SPDC. This includes frequency-domain OCT [160] and hyperspectral imaging. There have also been several spectroscopy applications, which use the tuneability of periodically poled downconversion crystals. This has enabled FT-IR spectroscopy of samples such as gases and polymers [161–163].

4.1.1 Experimental Techniques

The conditions required for interference can make the design and alignment of imaging with undetected photons setups challenging. Furthermore, the use of SPDC means the signal and idler paths are not visible to the eye, adding difficulty to alignment. Imperfections in the alignment can impair contrast of the interference fringes obtained, which ultimately limits the SNR of imaging. Here the conditions for interference and techniques to fulfil them and maximise fringe contrast are discussed.

In a typical interferometer, the coherence length of the source is a key consideration in design and alignment. In imaging with undetected photon schemes, there are two restrictions on path length mismatches arising from the downconverted photon pairs. Figure 4.2 shows a Mach-Zehnder type layout of a non-linear interferometer. If the distances from BS1 to the first and second non-linear crystals NL1 and NL2 is labelled $l_{p,1}$ and $l_{p,2}$ respectively, the idler path from NL1 to NL2 labelled $l_{i,1}$ and the signal paths $l_{s,1}$ and $l_{s,2}$ from NL1 (NL2) to BS2, the following conditions on path length difference must be met

$$\Delta l_1 = l_{p,1} + l_{i,1} - l_{p,2} < l_{coh,p}, \tag{4.1}$$

$$\Delta l_2 = l_{i,1} + l_{s,2} - l_{s,1} < l_{coh,s}, \tag{4.2}$$

where $l_{coh,p}$ and $l_{coh,s}$ are the coherence lengths of the pump and signal. In practise, the first condition means choosing a pump laser with a long enough coherence length for the chosen experimental layout, which should not be too much of a challenge given the availability of high power, long coherence length lasers available. However, second condition can prove more of a challenge due to the broadband nature of downconverted light, meaning the coherence length of the signal can be of the order of 10^{-5} m. Narrow bandpass filters, placed before the camera, can be used to narrow the linewidth of the signal photons in order to increase the coherence length. As with a typical interferometer, an alignment laser with longer coherence length can be used to find an approximate path length match and micrometre translation stages used to finely balance the signal and idler path lengths. Both conditions become simpler to meet if the interferometer is built in a Michelson type layout, also shown in Fig 4.2. In this configuration, when the two arms

are an equal length then both the path difference conditions will be met. As such, the Michelson configuration has become common amongst imaging with undetected photons set-ups.

The next consideration is the spatial alignment of the system. To observe interference with good visibility it is necessary that the signal and idler generated from the first crystal overlap well with the signal and idler generated in the second pass. Furthermore, imaging lenses must be positioned correctly to image the desired planes at each crystal, misalignment can reduce the degree of overlap and reduce visibility. As the SPDC beam in either the signal or idler arm is not visible by eye, it is usually helpful to align components using the pump, removing and replacing any dichroic mirrors as necessary so the pump beam is visible by eye and ensure both signal and idler passes overlap properly. To monitor the position of the beams it can also be useful to have access to imaging both the far-field and image plane of the crystal using flip mounts to ensure the beams are well overlapped. Access to both planes is useful for correct positioning of imaging lenses also; placing a knife-edge on mirrors and checking for a sharp edge in the far-field or imaging defects and dust on the surface of the crystal in the image plane.

In order to maximise fringe visibility, losses in the interferometer are also an important consideration. As losses in the idler beams between the first and second crystal reduce the mutual coherence of the signal beams, any loss in the idler arm will reduce the resulting fringe visibility and cannot be compensated for [164]. Therefore, it is essential that care is taken to minimise idler loss. This means ensuring all optics have the correct anti-reflection (AR) coatings, lens materials have the best possible transmission for the idler wavelength and similarly mirrors have the best possible reflectivity. Losses between the signal beams will also reduce fringe visibility; however, this can be compensated for by introducing loss into the other signal beam. In a two crystal setup such as the one shown in Fig. 4.2, by splitting the pump with a polarising beamsplitter (PBS) and positioning a rotating half wave plate before the PBS, the relative pump power between the two crystals can be controlled, allowing fringe visibility to be maximised [165] .

4.2 Off-axis Single Frame Complex Image Reconstruction for Imaging with Undetected Photons

In this section, the basis of the publication "Single-frame transmission and phase imaging using off-axis holography with undetected photons", published in Scientific Reports, is presented. This project was a collaboration with authors from Imperial College London and the University of Bristol, conceived of during meetings of the UK quantum imaging hub, QuantIC. All experimental work on the project was carried out by Dr. Emma Pearce and myself in Glasgow.

In all imaging with undetected photons schemes prior to this work, the interferometer has been aligned in an on-axis configuration. In an on-axis configuration, multiple interferograms must be acquired at equally spaced phase shifts to reconstruct the full oscillation for each pixel. This is achieved with a small movement of either the signal or idler mirror using some form of motorised stage. For these phase-shifting methods, a minimum of three images at different phases is required, which slows the effective frame rate of the system, as time is required for the stage to move and settle, and multiple exposures of the camera are needed. In the case of low photon flux at the detector, which is common when using SPDC illumination, long exposure times can be necessary making the overall process time consuming. One option is to image the transmission profile directly from the interference, allowing video rate imaging of the sample [166], however with this approach it is not possible to obtain a phase image of the sample. Another approach obtained both transmission and phase images from a single frame by splitting the detected signal into 4 regions of the sensor, each with a different phase shift and applied a phase-shifting reconstruction algorithm to the four images. However, this approach means that the SNR of the obtained interferogram is reduced by a factor of 4 when compared to conventional methods, and significant experimental complexity is introduced [167].

In this section, an experimental demonstration of a single-frame approach using off-axis holography is presented, as suggested in [164]. As discussed in Chapter 3, off-axis holography allows for reconstruction of the object field from a single interferogram by introducing an angle between the object and reference waves. The introduction of a spatial carrier frequency separates

the $+1$, -1, and DC diffracted orders from each other in $\mathbf{k}$-space. This allows digital filtering to be applied in $\mathbf{k}$-space and subsequent processing gives a reconstruction of the object field. In the case of a linear interferometer, the interference pattern detected on the camera takes the form

$$I_{tot} = I_{obj} + I_{ref} + 2\Re\left[E_{obj}(\mathbf{r})E^{*}_{ref}(\mathbf{r})\exp\left(i\mathbf{k_{tilt}}\mathbf{r}\right)\right], \tag{4.3}$$

where I_{obj} and I_{ref} are the intensities of the object and reference waves, E_{obj} and E_{ref} the complex fields of the object and reference waves and $\mathbf{k_{tilt}}$ is the relative wavevector between fields introduced as a spatial carrier frequency. As discussed in Section 3.1.2, typically the non-interfering terms I_{obj} and I_{ref} are subtracted using pre-recorded images and a Fast Fourier Transform (FFT) of the remaining terms yields the two interference terms which are separated in $\mathbf{k}$-space. The application of a spatial filter, for example a Gaussian low-pass filter, allows for the selection of one of these terms which, when an inverse FFT (IFFT) is performed, corresponds to $E_{obj}(\mathbf{r})E^{*}_{ref}(\mathbf{r})\exp\left(i\mathbf{k_{tilt}}\mathbf{r}\right)$. Assuming a flat phase profile, the measurement of I_{ref} allows for an estimate of E_{ref}, and a linear phase ramp can be calculated from the location of the centre of the term in the Fourier transform to correct for $\mathbf{k_{tilt}}$. This allows for a calculation of the field information about the object contained within E_{obj}.

Comparatively, in a nonlinear interferometer for imaging with undetected photons in the low gain regime of SPDC, the recorded intensity takes the form

$$I_{tot} = I_{sig,1} + I_{sig,2} + 2\Re\left[A_{sig,1}(\mathbf{r})A_{sig,2}(\mathbf{r})\exp\left(i\phi + i\mathbf{k_{tilt}}\mathbf{r}\right)\left[T(\mathbf{r})\exp\left(i\phi_{object}(\mathbf{r})\right)\right]^{2}\right], \tag{4.4}$$

where a position-dependent transmission $T(\mathbf{r})$ and phase $e^{i\phi_{object}(\mathbf{r})}$ contain the object information, which is squared as the object is double passed in the Michelson interferometer. Comparing with Eq. 4.3, it can be seen that $I_{sig,1} + I_{sig,2}$ can be determined by recording a frame when the idler beam is blocked, so a subtraction from the total intensity can be performed in a manner similar to a conventional reconstruction. A FFT of the subtracted image can then be taken and spatial filtering applied to select one of the diffracted orders. This results in $A_{sig,1}(\mathbf{r})A_{sig,2}(\mathbf{r})T^{2}(\mathbf{r})\exp\left(i\phi + 2i\phi_{object}(\mathbf{r}) + i\mathbf{k_{tilt}}\mathbf{r}\right)$ after the IFFT. It is assumed that the amplitude profile of the first and second pass signal beams, $A_{sig,1}(\mathbf{r})$ and $A_{sig,2}(\mathbf{r})$, respectively,

are approximately equal, and so division by half the measured DC signal, $(I_{sig,1} + I_{sig,2})$, yields $T^2(\mathbf{r}) \exp\left(i\phi + 2i\phi_{object}(\mathbf{r}) + i\mathbf{k_{tilt}}\mathbf{r}\right)$. The phase ramp $\mathbf{k_{tilt}}$ is calculated in exactly the same way as in a conventional off-axis scheme. The global phase (ϕ) can also be removed in a pre-calibration step by calculation of the phase without an object present. This allows for a calculation of the object transmission $T(\mathbf{r})$ and phase $\phi_{object}(\mathbf{r})$ from a single camera frame.

By obtaining tilt fringes within the non-linear interferometer, and following the above reconstruction process, it is demonstrated that it is possible to reconstruct transmission and phase images from a single interferogram. This demonstration will help reduce acquisition times in imaging with undetected photons schemes, and enable transmission and phase imaging capability of dynamic scenes. Since publication, the method has already been applied to reducing the acquisition time of methane sensing with undetected photons [168].

4.2.1 Imaging System

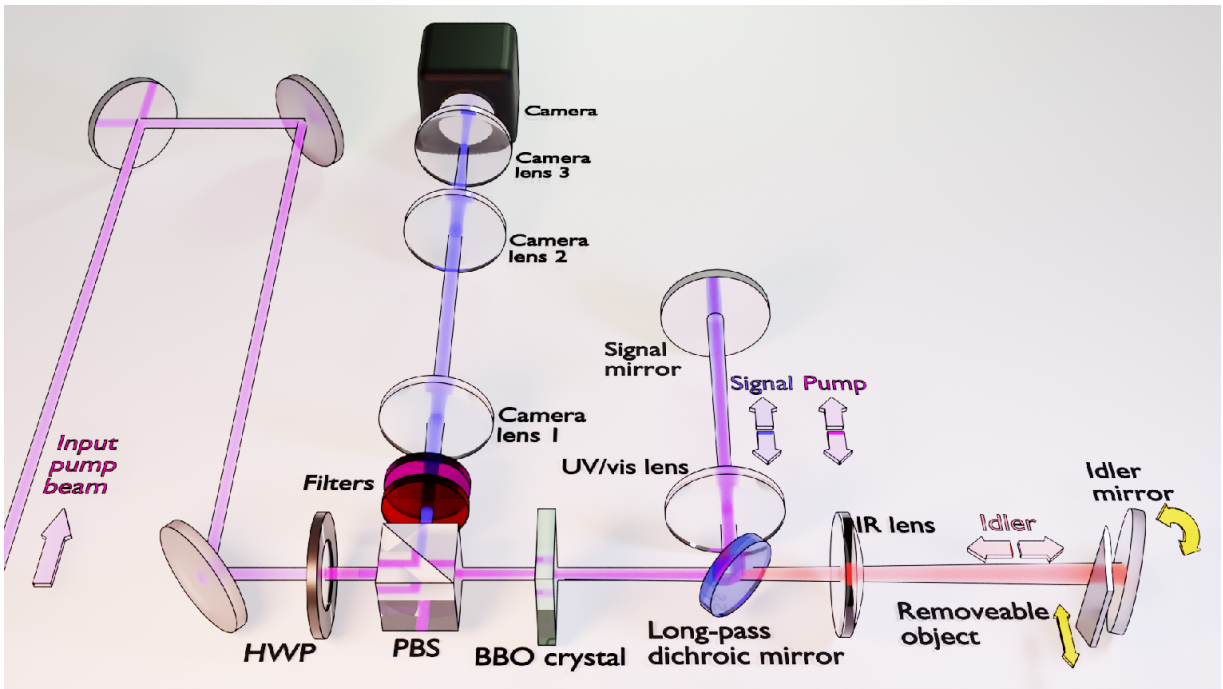

Figure 4.3: Experimental setup for off-axis holography with undetected photons. Purple indicates the UV, 355 nm pump beam, which is used to pump the BBO crystal, cut for type-1 non-degenerate downconversion to produce signal and idler pairs at 460 nm (blue) and 1555 nm (red), respectively. The interferometer uses a Michelson type layout, where the pump travels along the same optical path as the signal photons and are reflected back to a second pass of the crystal.

Figure 4.3 shows the experimental setup used to perform off-axis digital holography with undetected photons. A 275 mW continuous-wave laser at a wavelength of 355 nm is prepared in polarization by a half-wave plate (HWP) and a polarizing beam-splitter (PBS) before pumping a 5 mm-thick beta barium borate (BBO) crystal. Signal (460 nm) and idler (1555 nm) pairs are produced via non-degenerate type-1 SPDC. The idler photons are separated by a long-pass dichroic mirror, with signal and pump propagating together towards the signal mirror, while the idler is sent to the idler mirror. The object to be imaged is placed in front of the idler mirror. A lens in each arm ($f = 100$ mm) is used to image the Fourier plane of the crystal onto the mirrors (object). All three wavelengths are then reflected to pass back through the crystal. Upon the second pass of the pump, there is a probability to generate another signal-idler photon pair. If the interferometer is correctly aligned, the indistinguishability of idler pairs will induce coherence between the signal pairs. The signal and idler photons are then separated from the pump at the PBS, with any residual pump and idler removed by a combination of filters. The camera is placed in a projected Fourier plane of the crystal and records the interference of the signal photons. The idler photons which interact with the object are never detected.

Introducing tilt fringes can be achieved by either tilting the signal or idler mirror within a non-linear interferometer, even though the idler photons are never detected [169, 170]. This is remarkable when compared with a conventional interferometer, and is a consequence of the interference depending on all three fields within a non-linear interferometer. In this experiment, it was chosen to align the signal mirrors for maximum intensity at the camera to ensure good overlap between the two signal passes, and then introduce tilt through the idler mirror to produce tilt fringes at the detector.

In order to ensure that it is possible to isolate the +1 diffracted order from the DC and -1 order with the spatial filtering applied, enough tilt fringes must be introduced such that the +1 order is sufficiently separated in $\mathbf{k}$-space. Ideally, the spatially frequency of the tilt fringes introduced would also be faster than all spatial frequencies contained within the object and the signal beams such that filtering can be applied without compromising reconstructed image resolution by the removal of higher spatial frequencies. However, introducing more tilt fringes will worsen the fringe contrast as the beams walk off from each other, as with a conventional interferometer.

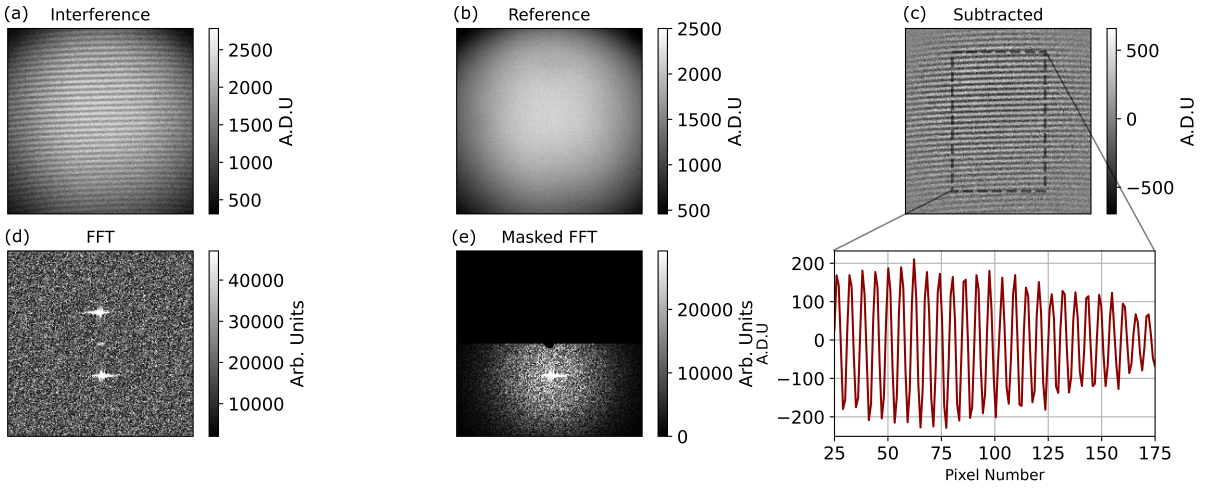

Figure 4.4: Digital off-axis holography acquisition and analysis. Example frames showing (a) interference, (b) the reference beam acquired by blocking the infrared path, and (c) interference with the reference subtracted. Raw camera frames are shown in Analog-to-Digital Units (A.D.U.) A vertical cut averaged over the rows (zoomed inset) shows ~ 25 fringes with a maximum $22.8 \pm 0.9\%$ contrast. Also shown is (d) the FFT of the subtracted image and (e) the mask used in the image reconstruction.

Alignment of the system thus becomes a balance between maintaining a reasonable fringe contrast such that signal-to-noise ratio (SNR) of images is preserved, whilst introducing enough tilt fringes in order to preserve high spatial frequencies in the reconstructed images after filtering. Figure. 4.4 shows the interference pattern and reference subtraction used; the system is aligned such that there are ~ 30 fringes in the field of view (FoV), measured to be 12.47 ± 0.03mm. This results in a maximum fringe contrast of $22.8 \pm 0.9\%$ as measured on 1000 reference-subtracted images, defined as $(I_{max} - I_{min})/2A_{sig,1}A_{sig,2}$, giving a maximum measurable transmission of 0.48 ± 0.01. A Gaussian filter was chosen to isolate the $+1$ diffraction order. Whilst subtraction of an image of the signal beams removes the majority of the DC component, a mask was applied to the central ~ 5 pixels to remove any remaining DC component. Figure 4.4 shows an example of an unmasked and masked FFT of the interference pattern used in the image reconstruction.

4.2.2 Results

Figure 4.5 shows transmission and phase images of a binary transmission, star-shaped target placed in the idler arm acquired with the imaging system. The transmission and phase images were both reconstructed from a single interferogram, which were acquired at a rate of 10 Hz.

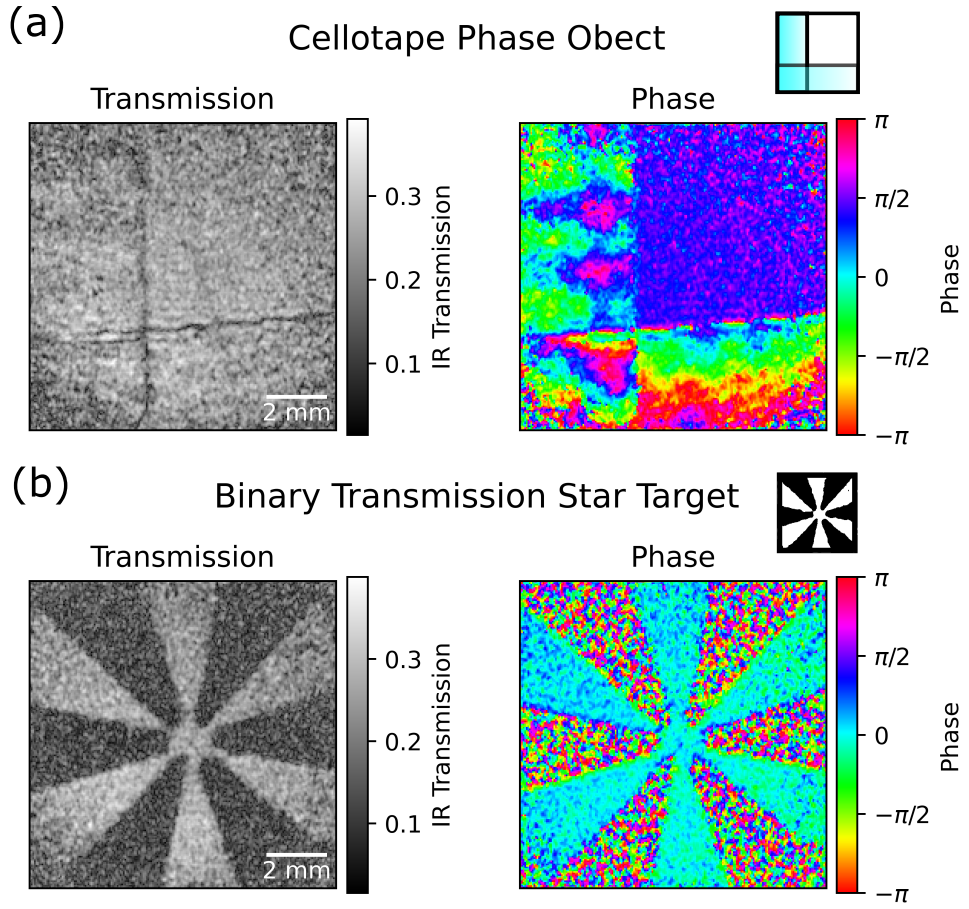

Figure 4.5: Single-frame complex image reconstruction of (a) a phase object (overlapping pieces of cellotape) and (b) a binary transmission object (3D printed star). Objects measured over a 12.47 ± 0.03 mm field of view. Note the phase measured here is twice the optical phase thickness of the object due to the double pass.

In order to demonstrate phase imaging capability of a system, an example of a transmissive 'phase object' made from two pieces of overlapping cellotape is also shown. From the phase images, variation in the optical thickness in the cellotape can be seen which is not present in the transmission image. Note that in the phase images, due to the presence of a global phase, a pre-calibrated reference phase has been subtracted in order to measure the phase profile of the object alone and no unwrapping is currently performed. Figure 4.5 demonstrates that by using off-axis holography, it is possible to reconstruct transmission and phase images from a single interference pattern in a non-linear interferometer where the light detected has never interacted with the object.

To assess the performance of the imaging system, the SNR and resolution of the reconstructed images were measured. These metrics were measured by placing a knife-edge in the

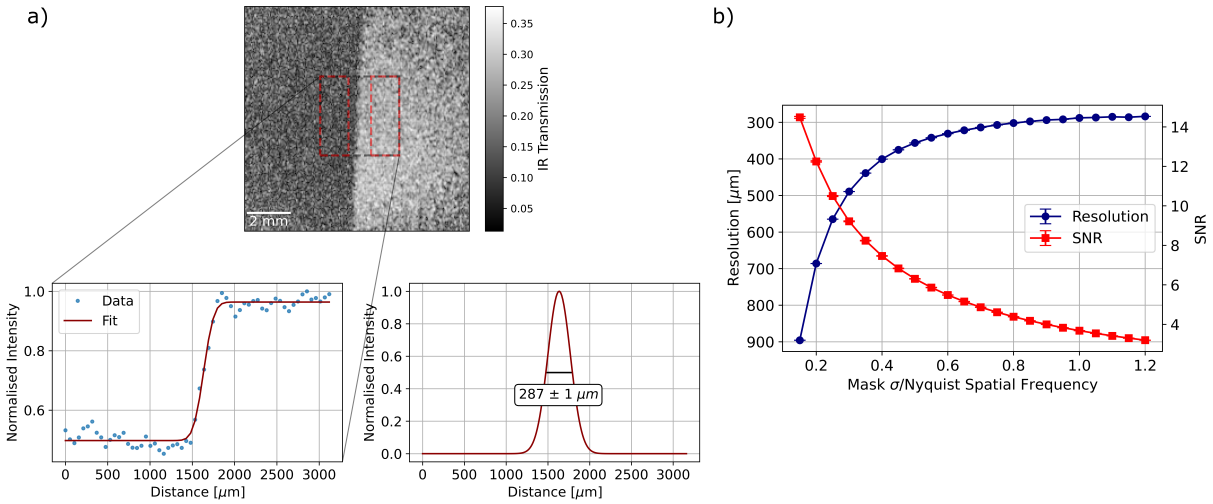

Figure 4.6: a) Reconstructed image of a slanted edge placed in the idler arm, with the region used to measure the edge response of the system indicated. The tilt of the edge was corrected for and the edge response fitted with a Gaussian error function (zoomed inset). The derivative of the error function is a Gaussian, the FWHM of which is used to calculate the point spread function. This was repeated for 1000 frames with the mean value calculated and error stated as the standard error on the mean. b) Plot of measured resolution and signal to noise ratio as the size of the high-pass Fourier filter is varied. It can be seen that an increasing mask size increases resolution whilst decreasing signal to noise ratio due to the inclusion of more spatial frequencies and more noise.

idler beam. The resolution was measured by fitting a Gaussian error function to the edge response, as shown in Fig. 4.6. The PSF of the system is calculated as the full width at half maximum (FWHM) of the Gaussian function obtained from the derivative of the Gaussian error function fitted to the edge response. This calculation was averaged over 1000 frames, which gives a measurement of the PSF in units of pixels. With knowledge of the magnification of the system, including the wavelength magnification inherent to imaging with undetected photons [171], and knowledge of the pixel size, the PSF of the system was calculated as $287 \pm 1\,\mu$m. The FoV of the system was calculated by a measurement of the extent of the signal beam on the camera and a similar calculation, measured to be 12.47 ± 0.03 mm. This allows for an approximation of the number of spatial modes of the system as 1890 ± 20. In the far-field [156], the theoretical FoV is calculated as $\text{FOV} = 2f\theta_i/M$ where f is the focal length of the lens matching the far-field of the crystal to the object, θ_i is the emission angle of the idler photons and M the magnification factor due to the difference in wavelength of signal and idler photons [171]. The emission angle of the idler photons can be derived from the phase-matching conditions in the

crystal, however this does not account for the broadband nature of the downconverted photons. To more accurately estimate the emission angle a model taking into account the 5 nm bandpass filter used in the experiment was used [39]. From this calculation, a FOV of ~ 12.97 mm is expected. The resolution is calculated as

$$\delta x_{corr} = \frac{\sqrt{2\ln 2} f \lambda_i}{\pi w_p M}, \tag{4.5}$$

where λ_i is the idler wavelength and w_p the pump beam waist. This gave a theoretical value of the resolution as $\sim 406\,\mu$m. The total number of spatial modes is then calculated as

$$m_{2D} = \left(\frac{\text{FOV}}{\delta x_{corr}} \right)^2, \tag{4.6}$$

giving a total number of modes as ~ 1000. The difference between the theoretical and experimentally measured value of the FoV in this experiment can be explained by the difference in the angle of the BBO compared to the nominal value used in calculations, and a difference in the modelled value of the emission angle compared to the true value. The emission angle is sensitive to the centre wavelength and bandpass of the filter placed before the camera; in this experiment the filter was tilted slightly to optimise the detection of the signal photons on the camera, and as such it is difficult to precisely estimate the centre wavelength and bandpass. The difference between the measured and theoretical FOV corresponds only to a 0.04° difference in emission angle. The difference between the theoretical and measured value of the resolution is likely due to error in the value of the pump waist used in the calculation, corresponding to a difference in beam waist of 0.4 mm. The value of the pump beam waist used was taken from the manufacturer specification sheet as 1.0 ± 0.2 mm. Further, the theoretical value is calculated from the correlation strength between downconverted pairs. For the calculation of the experimental value, it is assumed that the PSF is equivalent to the correlation strength, however this does not account for optical effects such as aberration which could broaden the PSF of the optical system and cause a discrepancy between theoretical and measured values.

Figure 4.6(b) shows the effect of changing the spread σ of the Gaussian mask used in the reconstruction process on both the measured resolution and SNR of the reconstructed images.

The SNR of the images was measured by masking the bright and dark regions of the image as indicated in Fig. 4.6(a) and averaging over 1000 images. The same process as detailed above was used to estimate the resolution of the images at different mask sizes. As the mask size is increased, it can be seen that the resolution improves as higher spatial frequencies are included in the reconstruction, however more noise is also passed through the filter causing a reduction in SNR. For the mask used in Fig. 4.6(a) (Mask σ/Nyquist Spatial Frequency = 1), the SNR was calculated as 3.680 ± 0.004. At this size of mask, it can be seen from Fig. 4.6(b) that the improvement in resolution begins to level off. As such it was determined that the masking process does not have a significant effect on the resolution of the system. As the predicted and measured resolution of the system are in agreement, it can be concluded that the off-axis approach does not result in a notable deterioration of the resolution of the imaging system. This is in agreement with Figure 4.4 which shows that the high spatial frequencies from the object appear well-separated in the +1 and -1 diffracted orders, and no fringes are observed in the reconstructed images, as would be the case if there was significant overlap between diffraction orders. As the alignment here was chosen as a balance between best separation of the +1 and -1 diffracted orders and SNR, there is still likely a small degree of information loss due to overlapping orders. Whilst greater separations were possible in this experimental configuration, they were avoided due to their adverse effect on SNR.

Finally, it is demonstrated that the single-frame reconstruction and FFT based analysis means that both the recording and reconstruction of transmission and phase images can be performed at video rates. The reconstruction process was integrated into a graphical user interface, allowing for the recording of dynamic scenes of frame rates of up to 33 frames per second. Figure 4.7 shows a sequence of images from a video of the binary transmission target as it is moved across the IR path, demonstrating the video rate capabability of the system.

4.2.3 Discussion

In previous experiments obtaining tilt fringes within non-linear interferometers, it was only possible to obtain a few fringes over the field of view (FoV). This is likely because in these experiments, quasi-phase-matched periodically poled downconversion crystals, such as ppKTP were

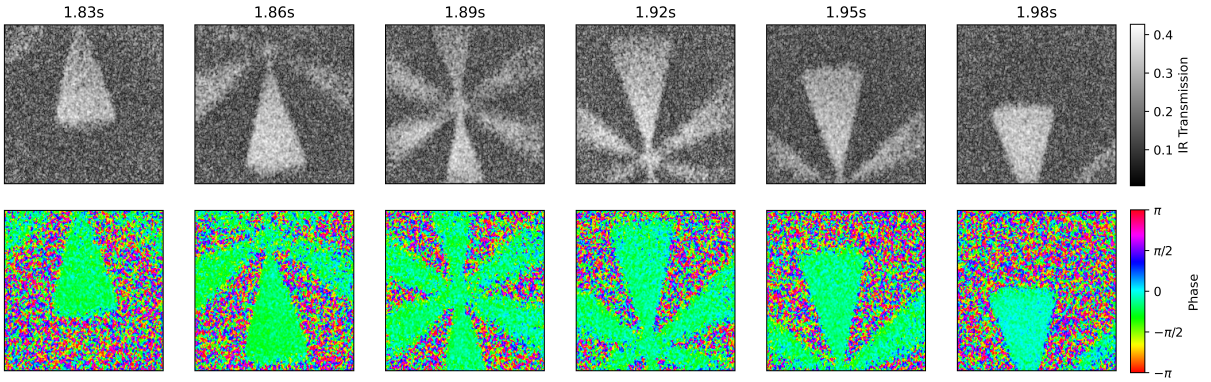

Figure 4.7: Reconstructed transmission and phase images from selected frames from a 33 frames per second video of a moving binary transmission target.

used. Periodically poled materials are typically chosen due to their higher downconversion efficiency, high non-linearities and wavelength tuneability when compared to bulk materials such as BBO. However, the poling of the crystal limits the transverse size possible, as such most periodically poled crystals have apertures limited to a couple of millimetres. Considering the sketch presented in Fig. 4.8, it can be seen how achieving significant tilt between interfering beams in the far-field, whilst maintaining overlap between the beams, necessitates some degree of separation at the crystal. By using a bulk BBO crystal, with dimensions 10 mm $\times$ 10 mm, a larger degree of tilt between beams can be introduced. This effect is evident here when tilting the signal mirror instead, as the first and second pass of the pump are visibly separated at the crystal when many fringes are present in the interferogram. The geometric constraints of the crystal aperture are therefore an important consideration when applying this technique to IUP systems. After submission of the manuscript that formed the basis of this section, a manuscript presenting an alternative method of performing off-axis holography with undetected photons came to the attention of the authors [172]. In this work, the forward and backward path of the signal photons are spatially separated into a Mach-Zehnder interferometer, before being recombined with a beamsplitter before the camera. A tilt angle between the two signal beams is introduced by one of the mirrors before the beamsplitter. Whilst this setup does introduce significant experimental complexity, it does allow for greater tilt angles to be introduced without sacrifice of SNR and provides a viable method if using a periodically poled crystal with a small aperture.

When using off-axis holography for imaging with undetected photons, the main downside

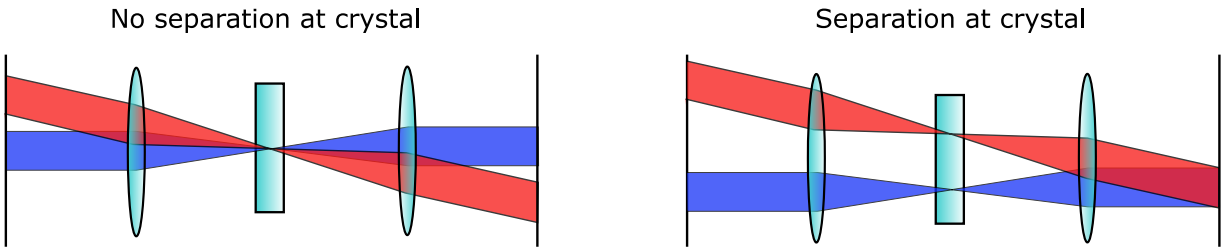

Figure 4.8: Sketch demonstrating how introducing tilt between interfering beams whilst maintaining overalp in the Fourier plane of the crystal necessitates some degree of separation of the beams at the crystal.

when compared with phase-shifting is the trade-off between SNR and resolution introduced by the tilt fringes themselves and the filtering process. Whilst in principle it is possible to perform off-axis holography without loss in resolution, obtaining a sufficient angle between interfering beams is a challenge in a nonlinear interferometer due to the loss of visibility when walking beams off from one another. Whilst an off-axis approach is unlikely to produce images with as high SNR and resolution as phase-shifting, it does have a significant advantage in the speed of both image acquisition and image processing, as well as experimental complexity, with no need for motorised stages.

Whilst the image reconstruction in this paper is relatively simple, there is scope to explore more complicated image reconstruction approaches, for which there is a large body of work within digital holography literature [173–175]. Some of these approaches may be able to increase the signal to noise ratio and resolution of the reconstructed images, addressing the issues discussed above [176]. By demonstrating off-axis holography with undetected photons, many previously demonstrated techniques within digital holography literature can now be explored at wavelengths which pose a challenge in terms of detector technology. Such techniques may include for example off-axis spatial multiplexing [177] and quantitative phase imaging techniques for disease identification [178].

To conclude, in this section work applying off-axis digital holography to imaging with undetected photons for the first time was presented. The use off-axis holography was found to have no noticeable effect on the resolution of the imaging. The single frame nature of the reconstruction process facilitated video rate imaging at 33 frames per second. This demonstration will help extend the applicability of imaging with undetected photons schemes to scenarios where acqui-

sition time and frame rate are an important consideration, such as the monitoring of industrial and biological processes in real time [132, 173].

4.3 Spiral Phase Imaging with a Spatial Light Modulator for Imaging with Undetected Photons

The work presented in this chapter was performed in the final months of the PhD studies. As such, it is unpublished and preliminary in nature. It is interesting however and points towards future developments in imaging with undetected photons, and as such has been included.

Within microscopy, there are several well known methods for altering image contrast of phase objects by manipulating the Fourier components of light coming from the object. For example, by shifting the phase of the undiffracted zeroth-order Fourier component by a quarter wavelength with respect to higher order components, an image with maximal enhanced contrast of the phase variations of the sample is obtained, in what is known as Zernike phase contrast [179]. Alternatively, the zeroth-order component can simply be blocked, resulting in details within the image appearing bright against a dark background, in what is called dark field microscopy [180]. Another type of filter is a spiral phase filter, with a helical phase proportional to $e^{i\ell\varphi}$, where ℓ is the helical index and φ the angular polar coordinate [181]. These create orbital angular momentum carrying Laguerre-Gauss beams. With $\ell = 1$, a phase mask is created which has a phase varying from $0-2\pi$ around a central axis with a phase singularity located in the centre. If the spiral phase mask is located in the Fourier plane of the object, the resultant image will appear dark except for the edges of the object, in an effect known as spiral phase contrast or isotropic edge enhancement [182, 183].

A full mathematical description of the spiral phase relief effect is provided in [184], which is omitted here for an intuitive explanation. The spiral phase filter, in combination with the Fourier transform lens transform a collimated beam to a focused 'doughnut' beam, with a ring shaped intensity beam. As a result, the point spread function (PSF) of the imaging system has a ring shaped intensity pattern, with an azimuthally varying phase between $0-2\pi$. In the object plane, it can be envisaged that each object 'pixel' is then one of these doughnut rings weighted by the complex object transmission function for that pixel, which is then integrated over the whole area. The resulting intensity in the image plane is then mainly determined by the complex value

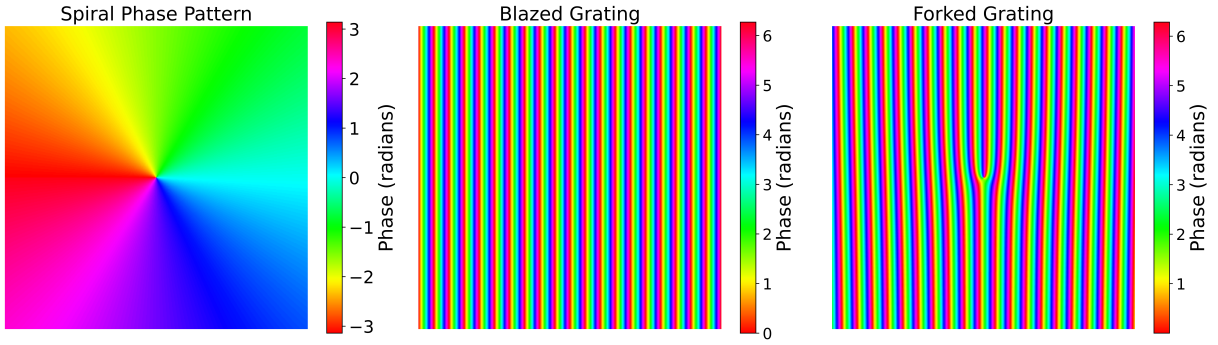

Figure 4.9: Example of the combination of a spiral phase pattern and a blazed diffraction grating, which can be combined to give a forked diffraction grating. When displayed on the SLM, the incoming light is diffracted, turning the imaging configuration from on-axis to off-axis and allowing for better modulation of the incoming light.

of neighbouring pixels, such that regions with little structure will appear dark as neighbouring pixels will be π out of phase due to the spiral phase topology of each ring and destructively interfere. In an area where there is a change in amplitude or phase of the object transmission function however, the resulting intensity will be different. In the case of a change in amplitude, the intensity of neighbouring rings is different across the amplitude variation, and thus there is not complete destructive interference and these regions appear brighter than their surroundings. In the case of a phase change, neighbouring pixels across the jump in phase are no longer π out of phase and complete destructive interference does not occur, and the edge at the jump will appear brighter. In these cases, any edges present in the image will appear brighter than their surroundings. It stands to reason that this effect will be most notable when the object produces a π phase jump.

One option to create an $\ell = 1$ spiral phase filter is to use a spiral phase plate. Alternatively, spatial light modulators have been demonstrated as an effective means of generating a spiral phase filter, and have the advantage of being able to switch between different imaging modalities (i.e dark field, phase contrast) without the need to switch physical optics [184–186]. The spiral phase pattern displayed on the SLM can be combined with a blazed diffraction grating, also displayed on the SLM, to produce a forked grating hologram, as shown in Fig. 4.9. This diffracts the incoming light, where the 1^{st} is used for imaging and the undiffracted zeroth order can be blocked, allowing for improved modulation of the imaging light.

The use of spatial light modulators for imaging with undetected photons is a relatively un-

explored topic. In one setup, an SLM was used to create a phase object for a demonstration of a classical equivalent for imaging with undetected photons [187]. Another recent experiment used an SLM to perform synthetic off-axis holography for imaging with undetected photons, by displaying a linear phase gradient on an SLM placed in place of a mirror in the idler arm of a Michelson interferometer. This way, tilt fringes at the detector could be achieved without the need to tilt any optical elements [188].

In this chapter, a method for manipulating the Fourier components of the light from the object, using a spatial light modulator which never 'seen' the object is demonstrated within an imaging with undetected photons imaging system. By displaying a spiral phase pattern on the SLM, it is possible to acquire an image showing isotropic edge enhancement. Whilst in this demonstration, the images had to be acquired by phase stepping, and other imaging modalities could not be shown due to experimental factors, the work presented here serves as a demonstration of the concept. A refined method could see various imaging modalities such as dark field and phase contrast demonstrated on a single camera frame. This would open the way to new imaging modalities for imaging with undetected photons schemes, and could remove the need for off-axis or phase-stepping holography techniques without sacrificing access to phase information.

4.4 Imaging system

Figure 4.10 shows the experimental setup used. A 355 nm pump beam is prepared in polarisation by a half-wave plate and polarising beamsplitter before pumping a 1 mm thick BBO crystal. The crystal is cut for type-I non-degenerate downconversion, producing signal and idler photon pairs at 460 nm and 1555 nm respectively. The signal and idler photon pairs are split into two arms of the interferometer using a long-pass dichroic mirror. Signal lenses 1 and 2 are used to image the crystal onto the SLM. A grating is displayed on the SLM and by tilting the SLM the 1st diffraction order is reflected back towards the crystal. Idler lens 1 and 2 similarly image the crystal onto the idler mirror, with the object placed in the far-field of the crystal. A short-pass dichroic mirror placed after the crystal separates the pump beam from the signal and idler

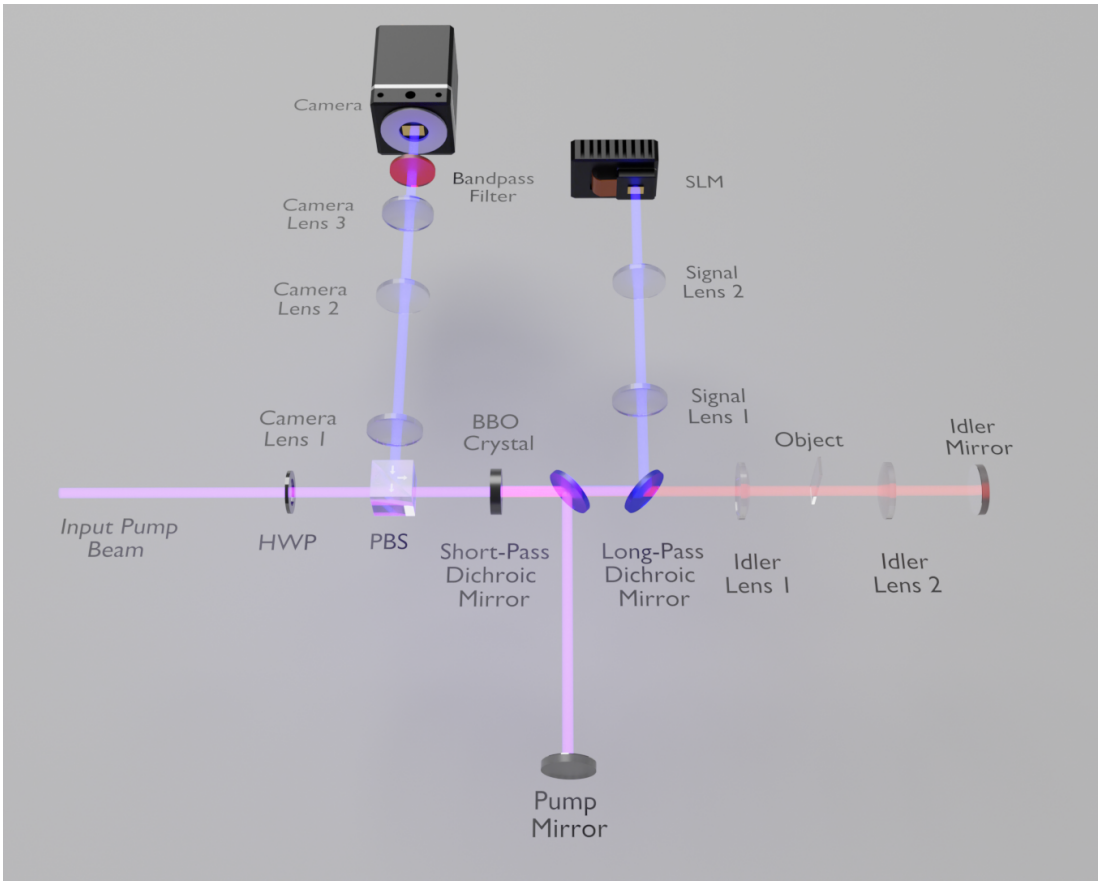

Figure 4.10: Diagram of the experimental setup used to modulate the Fourier components of light from the object whilst imaging with undetected photons. A 355 nm pump beam pumps a 1 mm thick BBO crystal, creating downconverted signal and idler pairs at 460 nm and 1555 nm respectively. Signal and idler photons are separated by a dichroic mirror into the two arms of the interferometer, which each contain a $4f$ imaging system. In the signal arm, a spatial light modulator is located at $4f$, whilst in the idler arm the object is located at $2f$. This places the SLM in the far-field of the object, and the object in the far-field of the crystal. Camera lenses 1, 2 and 3 then image the object and the project far-field of the crystal onto the camera.

photons, and the pump mirror reflects the pump back towards the crystal. This step is necessary to protect the SLM from damage by the pump. The second pass of the pump beam through the crystal generates a second pair of signal and idler photons, where sufficient overlap of the idler modes results in induced coherence between the two signal beams. The camera is placed in the far-field of the crystal and the object is re-imaged by camera lenses 1, 2 and 3.

Within a nonlinear interferometer designed for imaging, the choice of lens system in the signal and idler arms of the interferometer is limited by the need to maintain spatial correlations between signal and idler photon pairs so full-field imaging can be performed. Imaging with undetected photons has been demonstrated utilising both momentum anti-correlations and position correlations. In practise, this means choosing a lens system such that the object and camera are placed in a Fourier or image plane of the camera, and that the lens system performs the same transform in the signal and idler arms of the interferometer, to maintain the spatial correlations. The inclusion of an SLM places an additional constraint; in order to shape the Fourier components of the light from the object, the SLM must be placed in a plane Fourier to the object in the signal arm of the interferometer. We utilise the folded Michelson style design of the SU(1,1) interferometer which has become common in imaging with undetected photons schemes, placing a $4f$ imaging system in the signal and idler arm of the interferometer. This allows for the signal mirror to be replaced with an SLM, and an object to be placed in a plane Fourier to the SLM and the downconversion crystal. A series of lenses is then used to image the Fourier plane of the crystal and object onto the camera. This imaging system allows for the conditions of maintaining spatial correlations between photon pairs and the SLM being placed in a plane Fourier to the object without double passing the SLM.

A downside of the Michelson style nonlinear interferometer used here is that the object is double passed. Usually in imaging with undetected photons schemes this is not an issue as the object is placed on or close to the mirror such that the images overlap. However in this system two images of the object are formed in two halves of the field of view. This effectively halves the number of spatial modes available for imaging. This issue could be alleviated by adopting a Mach-Zehnder style design of nonlinear interferometer, as was used in the initial demonstration of imaging with undetected photons [155].

4.5 Results

To assess the resolution of the imaging system, a USAF resolution test target was imaged as shown in Fig. 4.11. It was determined from Fig. 4.11 that the smallest element resolvable was element 4 of group 2. This gives an estimate of the resolution of the system as $4\,\mathrm{lp\ mm^{-1}}$ (line pairs per millimetre). With the object placed in the far-field of the downconversion of the crystal, the theoretical value of the resolution is given by

$$\delta x_{corr} = \frac{\sqrt{2\ln 2} f \lambda_i}{\pi w_p M}, \tag{4.7}$$

where f is the focal length of the lens used to image the far-field of the crystal onto the object, λ_i the idler wavelength, w_p the pump beam waist and M the wavelength magnification factor due to the difference in signal and idler wavelengths [189]. For this experiment, this gives the expected resolution as $\sim 147\,\mu$m, agreeing well with the measured resolution. Similarly to the previous section, the bandwidth of the downconverted idler photons was modelled [39], and the theoretical value of the field of view was calculated as 22.0 mm. The field of view was approximately measured using a reticle, as shown in Fig. 4.12. The outermost ring indicates 15 mm. The discrepancy between these values is likely due to tilt of the bandpass filter before the camera altering the true value of the bandpass. Using the measured value of the resolution, and approximating the field of view as 15 mm, the number of spatial modes can be roughly estimated as $\sim (94)^2$.

Ideally, the interferometer would be aligned on-axis and then the path length adjusted until the zero phase delay point was reached, and the resulting interference pattern was a beam of either perfect constructive interference or destructive interference. Then the constructive interference beam would be used for bright field imaging and imaging modalities could be switched by changing the pattern on the SLM, without any need for holographic image reconstruction. However, the interferometer could not be perfectly aligned to the zero phase delay point, with residual fringes always seen, as shown in Fig. 4.13. This is potentially due to curvature of the pump beam. Further, there was significant phase instability between exposures, meaning the interference pattern would fluctuate between constructive and destructive interference. This

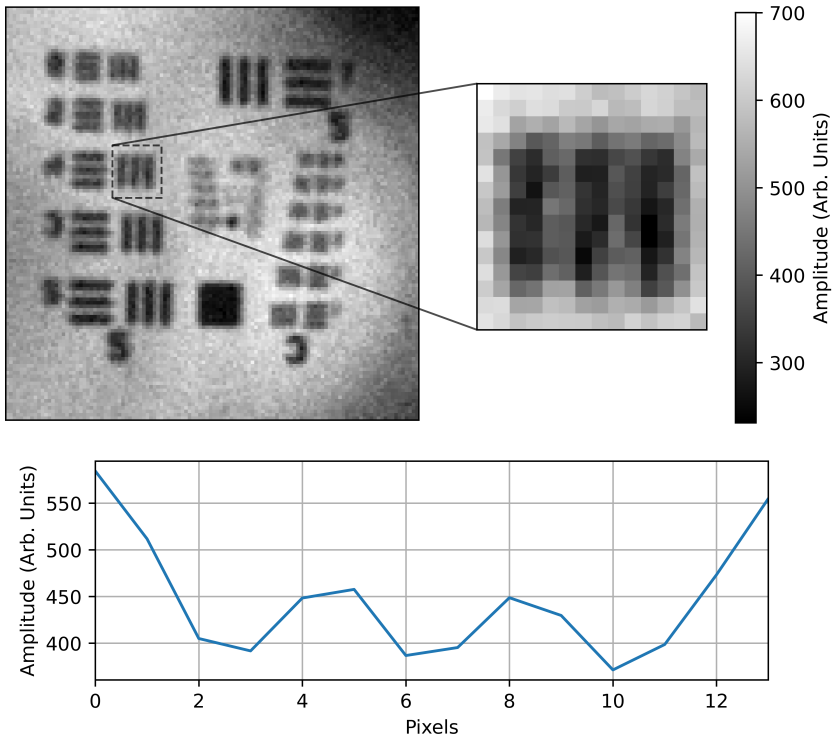

Figure 4.11: Determination of the resolution of the imaging system with a USAF target. The smallest resolvable element of the USAF test target was determined to be element 4 of group 2, which is shown enlarged and a horizontal cross section of the intensity of the enlarged region is also shown. Element 4 of group 2 corresponds to a spatial frequency of 4 lp mm^{-1}.

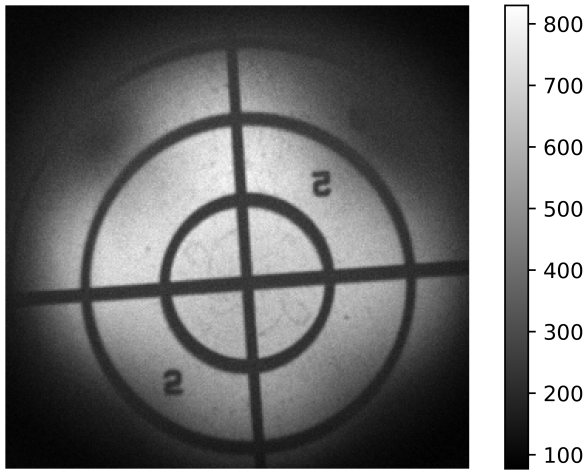

Figure 4.12: Determination of the field of view of the system using a reticle. The rings are spaced in increments of 5 mm. From this, the field of view is roughly estimated as 15 mm.

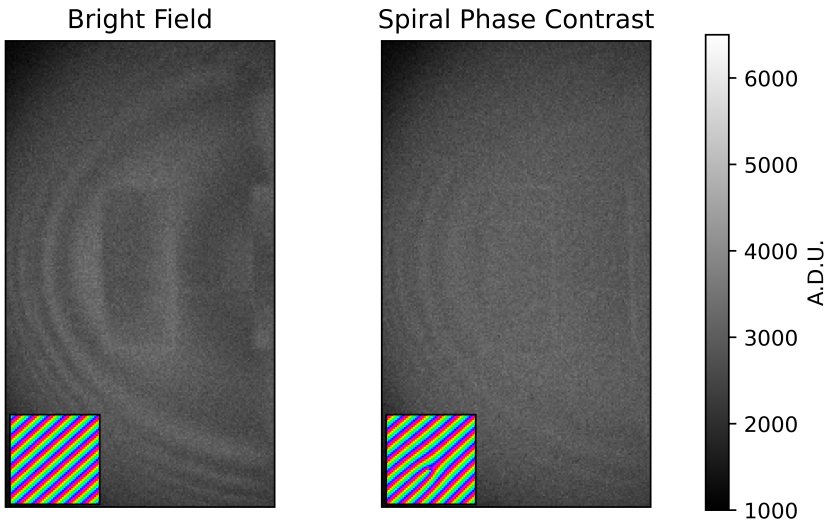

Figure 4.13: Bright field and spiral phase contrast images obtained from a single camera exposure. It can be seen in the bright field image that it was not possible to align the interferometer such that the phase was flat across the beam, and fringes remained over the field of view. When displaying the forked grating on the SLM, the contrast of the fringes is greatly reduced as would be expected, however the edges of the object do not appear significantly brighter. Note A.D.U. stands for analogue to digital units.

was noticed to be introduced when the pump was separated with the short-pass dichroic mirror, which could either be due to the extra turbulence from another optical path, or the short-pass mirror vibrating within the mount. The spiral phase effect was not significant on a single frame, likely due to low signal photon counts due to the thin crystal used and low fringe visibility. As frames could not be averaged due to the phase instability, reconstruction methods had to be used. It is a point of interest that in the work in the previous section, off-axis holography was used. However, in this configuration it was not possible, as due to the $4f$ imaging system in each arm, tilting the mirrors does not alter the position of the fringes. Instead, phase-stepping reconstruction methods, as described in Section 3.1.2 were used.

Figure 4.14 shows the results of applying a spiral phase mask to the grating displayed on the SLM whilst imaging a phase object. Each image is the average of 100 intensity images, reconstructed by phase stepping. Without the spiral phase mask applied, a bright field image of the object is obtained, where the edges of the etchings appear dark against a bright background. When the spiral phase mask is applied, the background image intensity is redirected to the edges, resulting in bright edges appearing on a dark background. When applying a spiral phase mask,

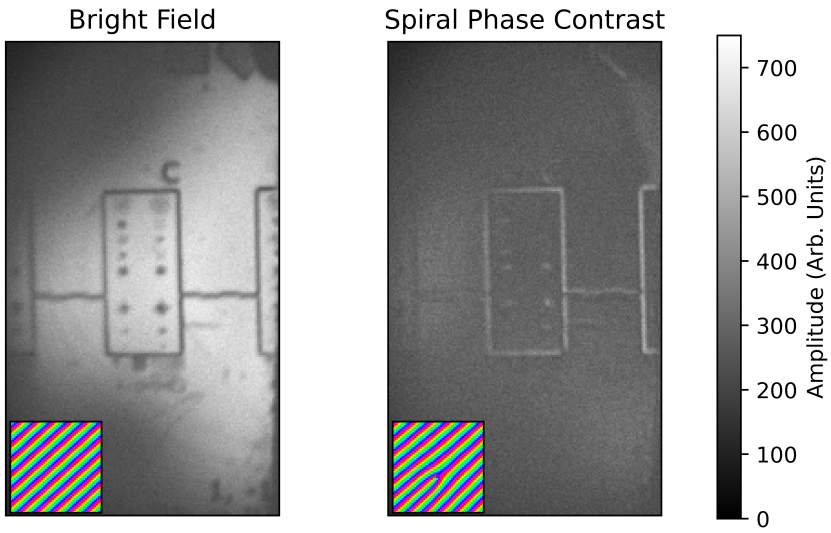

Figure 4.14: Bright field and spiral phase contrast images of a phase object acquired with the system. Each image is the average of 100 intensity images reconstructed from phase stepping. Also shown is the pattern displayed on the SLM for each image. It can be seen that in the spiral phase contrast image, the intensity is redirected to the edges of the object with the surroundings appearing dark.

the total image intensity of the spiral phase filtered image should be roughly equal to the total image intensity of the bright field image. This case the intensity of the spiral phase filtered image corresponds to $\sim 70\%$ of the total bright field image intensity.

4.6 Discussion

In this section, a novel use of a spatial light modulator within an imaging with undetected photons scheme has been presented. By replacing the signal mirror in a Michelson nonlinear interferometer, it is possible to manipulate the Fourier components of light from the object, by only modulating signal photons which have never seen the object. By displaying a spiral phase pattern on the SLM, it was possible to obtain images showing an edge enhancement effect produced by the spiral phase filter. Whilst the effect was not significant on a single frame, the demonstration serves as a proof of concept, and highlights the possibility of using an SLM to perform single frame imaging of phase objects, without the need for holography techniques. Furthermore, the work here demonstrates a method which could be used if one wished to image using an SLM at a challenging wavelength for SLM technology, for example into the MWIR,

due to the modulation only being performed on the visible signal photons.

Two of the main reasons the imaging system was not capable of producing high contrast edge enhanced images on a single frame were low fringe visibility and phase instability in the interferometer. Fringe visibility is a particular challenge when using an SLM, as signal photons are lost when they are diffracted into orders other than the selected $+1$ diffracted order, causing an imbalance in the amplitudes of the two signal fields, which reduces fringe visibility. It is suggested that switching to a Mach-Zehnder interferometer layout with two nonlinear crystals could help address both the issue of low fringe visibility and phase instability; the pump could be separated with a sturdier element to reduce phase instability introduced by the short-pass dichroic mirror, and loss compensation could be implemented with the use of polarisation optics in the pump beam, as in [165]. The Mach-Zehnder geometry would also alleviate the issue of two images forming in the FoV due to the double pass of the object.

It was also explored whether other types of Fourier filters could be displayed on the SLM to observe for example, dark-field, phase contrast and spiral phase relief effects for multimodal imaging [182]. However, none of the these effects were successfully observed when the corresponding Fourier filters were displayed on the SLM. Common to all these filters is that a circular region in the middle of the filter is replaced with a different phase to the rest of the filter, for example for dark-field the central region is set to 0, whilst for phase contrast and spiral phase relief effects the central region is offset by $\pi/2$ compared to the rest of the filter [184]. The size of this circular region should correspond to the size of the DC component of the image Fourier transform. The size of the DC component of the image Fourier transform is related to the Airy diffraction pattern of the image through the lens system, and can be estimated as

$$s = 1.22\frac{\lambda f}{d}, \tag{4.8}$$

where s is the size of the DC component and d the field of view at the object plane. For the system used here, with $f = 75$ mm and $d = 22.0$ mm, the size of the DC component at the SLM is estimated to be 1.91 μm. As an SLM with a pixel size of $20\,\mu$m was used, it is likely that the DC component is too small compared to the size of the SLM pixels to observe these effects.

This could also explain the relatively low contrast of the spiral phase contrast images. Using an SLM with smaller pixels could help alleviate this issue, and potentially lead to demonstrations of the other discussed imaging modalities.

Chapter 5

Conclusions

In this thesis three different methods for the reduction of sources of noise in imaging have been investigated. The first method, presented in Chapter 2, was a quantum imaging scheme which utilised spatial correlations between photon pairs produced by SPDC and new camera technology, capable of resolving the number of photons in each pixel. By designing the imaging system such that both photons in each pair produced would arrive in the same pixel, improvement in image contrast was demonstrated when constructing images consisting of only two-photon events when using SPDC illumination compared with classical LED illumination. The improvements in image contrast were only modest, due to the low efficiency of pair detection of the system, and the readout noise of the camera. However, it did demonstrate the validity of the concept, and demonstrated the use of new photon counting camera technology within a quantum imaging experiment. This could be useful for the development of image plane quantum imaging schemes, where the most tightly correlated photon pairs arrive in the same pixel.

Improving the enhancements produced by this method would rely either on improving the efficiency of pair detection, or the reduction of readout noise on future photon number resolving detectors. Changing the downconversion crystal and pump to produce photon pairs at 532 nm has been suggested as a method to increase the efficiency of pair detection due to the higher quantum efficiency of the sensor at green wavelengths, and is the subject of current work in Glasgow. A thinner crystal could also be used to reduce to transverse size of the correlations at the detector, however with the transverse correlation size in this experiment having a value

of 0.14 pixels the larger issue is likely to be broadening of the correlations due to the PSF of the imaging system. In future work, the PSF of the imaging system could be quantified to confirm whether this is causing significant broadening of the extent of the correlations at the detector and investigations on how to reduce the size of the PSF could be carried out. It is also expected that improvements in the readout noise of photon number resolving detectors would improve the system, as it would reduce the number of accidental coincidences recorded. Whilst photon number resolving camera technology is highly impressive, the dark event rate using the photon number resolving detector was a factor of ~ 4 times higher than in previous experiments carried out in the group using an EMCCD detector [85, 190]. Furthermore, it was shown in later work that the EMCCD outperformed the photon number resolving detector for event rates of < 1 photon per pixel per frame [122]. Improvements in sensor readout noise will improve the performance and feasibility of photon number resolving detectors in quantum imaging experiments.

The use of photon number resolving detectors could also be explored for other quantum imaging experiments where it is necessary to detect multiple photons in each pixel. These could be for example 2-photon NOON state experiments, where the use of a photon number resolving array detector could allow for full-field imaging as opposed to scanning. Such systems could be used to demonstrate quantum enhanced phase imaging schemes [191, 192].

Chapter 3 presented the second method, where a homodyne gain effect that could be utilised in holographic imaging, as originally proposed by Gabor, was applied to enable near single photon imaging in the shortwave infrared. This was despite the InGaAs detector having a noise floor ~ 200 times higher. The method was then applied to stand-off speckle holography, which allowed for an increase in the range of stand-off vibrometry system by being able to detect the phase of a vibrating target when the signal fell under the noise floor of the detector.

In terms of future work, finding applications where detector noise is high and the image signal is low have the most promise for homodyne or heterodyne holographic imaging schemes. For example, imaging weakly scattered light from the eye at kHz frame rates to perform flow measurements on blood vessels has been demonstrated by one group [145, 193, 194]. Other applications could potentially be found at wavelengths outwith the visible and SWIR regions, where

cameras are even noisier and more expensive, such as X-ray, midwave infrared and terahertz regions. Another interesting possibility would be utilising the gain effect in situations where the signal and reference come from two different sources using intensity correlation holography. This uses a method first demonstrated by Hanbury, Brown and Twiss to measure intensity correlations between two independent sources to obtain holograms, with the requirement that the integration time of the detector is less than the coherence time of the two fields [195]. Improvements in the time resolution of array detectors have made full-field holography based on this principle possible, and future improvements could see the possibility of interfering a bright reference beam with a weak independent source, such Raman scattered light or fluorescence. Such a scheme could help realise improvements in microscopy methods based on these effects.

In Chapter 4, the knowledge of downconversion sources, quantum imaging experiments and holography techniques was combined to apply off-axis holography to imaging with undetected photons. This allowed for the reconstruction of transmission and phase images from a single interferogram, enabling video rate imaging of a dynamic scene. It was demonstrated that the off-axis reconstruction did not have a significant deterioration on the resolution of the imaging system.

Also demonstrated was a method to incorporate a spatial light modulator within a nonlinear interferometer for imaging with undetected photons, for the purpose of manipulating the Fourier components of light from an object by only modulating photons that had not 'seen' the object. Whilst preliminary in nature, the results highlighted the validity of the concept. Future work should concentrate on improving several experimental factors to make the scheme feasible, including improving fringe visibility, phase stability and the number of SLM pixels covered by the signal beam.

Imaging with undetected photons appears to be one of the most likely quantum imaging schemes to find practical applications. This is due to the fact that the interferometer does not require operation in a photon sparse regime at the detector, meaning long acquisition times are not required. As such, they show promise for applications far into the midwave infrared, where sensor technology is still highly expensive, noisy and low resolution. Of particular interest is histopathology applications in $6-8\,\mu m$ range, where there are distinct molecular fingerprints

for various diagnoses. Future work on imaging with undetected photons will likely focus on implementing different crystal materials with large non-linearity such as AGS (Silver Gallium Sulfide), and the challenges that will be associated with longer wavelengths, such as resolution of the imaging system and meeting phase matching conditions.

Bibliography

[1] M. A. Taylor and W. P. Bowen, "Quantum metrology and its application in biology," Physics Reports **615**, 1–59 (2016).

[2] A. Khodjakov and C. L. Rieder, "Imaging the division process in living tissue culture cells," Methods (San Diego, Calif.) **38**, 2–16 (2006).

[3] S. Wäldchen, J. Lehmann, T. Klein, S. van de Linde, and M. Sauer, "Light-induced cell damage in live-cell super-resolution microscopy," Scientific Reports **5**, 15348 (2015).

[4] J. Biele, S. Wollmann, J. W. Silverstone, J. C. F. Matthews, and E. J. Allen, "Maximizing precision in saturation-limited absorption measurements," Physical Review A **104**, 053717 (2021).

[5] J. Hecht, "Lidar for Self-Driving Cars," Optics and Photonics News **29**, 26–33 (2018).

[6] R. Tobin, A. Halimi, A. McCarthy, M. Laurenzis, F. Christnacher, and G. S. Buller, "Three-dimensional single-photon imaging through obscurants," Optics Express **27**, 4590–4611 (2019).

[7] A. Maccarone, A. McCarthy, X. Ren, R. E. Warburton, A. M. Wallace, J. Moffat, Y. Petillot, and G. S. Buller, "Underwater depth imaging using time-correlated single-photon counting," Optics Express **23**, 33911 (2015).

[8] B. Redding, A. Davis, C. Kirkendall, and A. Dandridge, "Measuring vibrational motion in the presence of speckle using off-axis holography," Applied Optics **55**, 1406 (2016).

[9] S. D. Johnson, P.-A. Moreau, T. Gregory, and M. J. Padgett, "How many photons does it take to form an image?" Applied Physics Letters **116**, 260504 (2020).

[10] M. Gilaberte Basset, F. Setzpfandt, F. Steinlechner, E. Beckert, T. Pertsch, and M. Gräfe, "Perspectives for Applications of Quantum Imaging," Laser & Photonics Reviews **13**, 1900097 (2019).

[11] H. A. Bachor and Timothy C. Ralph, "Quantum Models of Light," in *A Guide to Experiments in Quantum Optics,* (John Wiley & Sons, Ltd, 2004), chap. 4, pp. 60–98.

[12] G. Brida, M. Genovese, and I. R. Berchera, "Experimental realization of sub-shot-noise quantum imaging," Nature Photonics **4**, 227–230 (2010).

[13] V. Giovannetti, S. Lloyd, and L. Maccone, "Advances in quantum metrology," Nature Photonics **5**, 222–229 (2011).

[14] H. T. Beier and B. L. Ibey, "Experimental Comparison of the High-Speed Imaging Performance of an EM-CCD and sCMOS Camera in a Dynamic Live-Cell Imaging Test Case," PLoS ONE **9**, e84614 (2014).

[15] M. Bigas, E. Cabruja, J. Forest, and J. Salvi, "Review of CMOS image sensors," Microelectronics Journal **37**, 433–451 (2006).

[16] M. Rezaei, M.-S. Park, C. Rabinowitz, C. L. Tan, S. Wheaton, M. Ulmer, and H. Mohseni, "InGaAs based heterojunction phototransistors: Viable solution for high-speed and low-noise short wave infrared imaging," Applied Physics Letters **114**, 161101 (2019).

[17] S. Beer and J. R. Brown, "Igniting questions, detecting answers: Hamamatsu Photonics introduces the world's first photon-number-resolving scientific camera," in *Quantum Technology: Driving Commercialisation of an Enabling Science III,* vol. 12335 (SPIE, 2023), pp. 43–47.

[18] A. D. Hood, M. H. MacDougal, J. Manzo, D. Follman, and J. C. Geske, "Large-format InGaAs focal plane arrays for SWIR imaging," in *Infrared Technology and Applications XXXVIII,* vol. 8353 (SPIE, 2012), pp. 116–122.

[19] T. H. Maiman, "Stimulated Optical Radiation in Ruby," Nature **187**, 493–494 (1960).

[20] A. Einstein, B. Podolsky, and N. Rosen, "Can Quantum-Mechanical Description of Physical Reality Be Considered Complete?" Physical Review **47**, 777–780 (1935).

[21] N. Bohr, "Can Quantum-Mechanical Description of Physical Reality be Considered Complete?" Physical Review **48**, 696–702 (1935).

[22] J. S. Bell, "On the einstein podolsky rosen paradox," Physics **1**, 195–200 (1964).

[23] J. F. Clauser, M. A. Horne, A. Shimony, and R. A. Holt, "Proposed experiment to test local hidden-variable theories," Physical review letters **23**, 880 (1969).

[24] S. J. Freedman and J. F. Clauser, "Experimental test of local hidden-variable theories," Physical Review Letters **28**, 938 (1972).

[25] D. M. Greenberger, M. A. Horne, A. Shimony, and A. Zeilinger, "Bell's theorem without inequalities," American Journal of Physics **58**, 1131–1143 (1990).

[26] A. Aspect, P. Grangier, and G. Roger, "Experimental Tests of Realistic Local Theories via Bell's Theorem," Physical Review Letters **47**, 460–463 (1981).

[27] A. Aspect, J. Dalibard, and G. Roger, "Experimental test of Bell's inequalities using time-varying analyzers," Physical review letters **49**, 1804 (1982).

[28] B. Hensen, H. Bernien, A. E. Dréau, A. Reiserer, N. Kalb, M. S. Blok, J. Ruitenberg, R. F. L. Vermeulen, R. N. Schouten, C. Abellán, W. Amaya, V. Pruneri, M. W. Mitchell, M. Markham, D. J. Twitchen, D. Elkouss, S. Wehner, T. H. Taminiau, and R. Hanson, "Loophole-free Bell inequality violation using electron spins separated by 1.3 kilometres," Nature **526**, 682–686 (2015).

[29] S. Storz, J. Schär, A. Kulikov, P. Magnard, P. Kurpiers, J. Lütolf, T. Walter, A. Copetudo, K. Reuer, A. Akin, J.-C. Besse, M. Gabureac, G. J. Norris, A. Rosario, F. Martin, J. Martinez, W. Amaya, M. W. Mitchell, C. Abellan, J.-D. Bancal, N. Sangouard, B. Royer, A. Blais, and A. Wallraff, "Loophole-free Bell inequality violation with superconducting circuits," Nature **617**, 265–270 (2023).

[30] R. W. Boyd, *Nonlinear Optics* (Elsevier, 2020).

[31] S. E. Harris, M. K. Oshman, and R. L. Byer, "Observation of Tunable Optical Parametric Fluorescence," Physical Review Letters **18**, 732–734 (1967).

[32] D. Magde and H. Mahr, "Study in ammonium dihydrogen phosphate of spontaneous parametric interaction tunable from 4400 to 16 000 \AA," Physical Review Letters **18**, 905 (1967).

[33] R. L. Byer and S. E. Harris, "Power and Bandwidth of Spontaneous Parametric Emission," Phys. Rev. **168**, 1064–1068 (1968).

[34] J. A. Armstrong, N. Bloembergen, J. Ducuing, and P. S. Pershan, "Interactions between light waves in a nonlinear dielectric," Physical review **127**, 1918 (1962).

[35] J. E. Midwinter and J. Warner, "The effects of phase matching method and of uniaxial crystal symmetry on the polar distribution of second-order non-linear optical polarization," British Journal of Applied Physics **16**, 1135–1142 (1965).

[36] D. A. Kleinman, "Theory of Optical Parametric Noise," Phys. Rev. **174**, 1027–1041 (1968).

[37] C. K. Law and J. H. Eberly, "Analysis and Interpretation of High Transverse Entanglement in Optical Parametric Down Conversion," Physical Review Letters **92**, 127903 (2004).

[38] H. Vanherzeele and C. Chen, "Widely tunable parametric generation in beta barium borate," Applied Optics **27**, 2634–2636 (1988).

[39] N. Boeuf, D. Branning, I. Chaperot, E. Dauler, S. Guerin, G. Jaeger, A. Muller, and A. Migdall, "Calculating characteristics of noncollinear phase matching in uniaxial and biaxial crystals," Optical Engineering **39**, 1016 (2000).

[40] F. M. Miatto, D. Giovannini, J. Romero, S. Franke-Arnold, S. M. Barnett, and M. J. Padgett, "Bounds and optimisation of orbital angular momentum bandwidths within parametric down-conversion systems," The European Physical Journal D **66**, 178 (2012).

[41] J. Romero, D. Giovannini, S. Franke-Arnold, S. M. Barnett, and M. J. Padgett, "Increasing the dimension in high-dimensional two-photon orbital angular momentum entanglement," Physical Review A **86**, 012334 (2012).

[42] P. G. Kwiat, K. Mattle, H. Weinfurter, A. Zeilinger, A. V. Sergienko, and Y. Shih, "New high-intensity source of polarization-entangled photon pairs," Physical Review Letters **75**, 4337 (1995).

[43] O. Kwon, Y.-W. Cho, and Y.-H. Kim, "Single-mode coupling efficiencies of type-II spontaneous parametric down-conversion: Collinear, noncollinear, and beamlike phase matching," Physical Review A **78**, 053825 (2008).

[44] O. Wolley, T. Gregory, S. Beer, T. Higuchi, and M. Padgett, "Quantum imaging with a photon counting camera," Scientific Reports **12**, 8286 (2022).

[45] O. Wolley, S. Mekhail, P.-A. Moreau, T. Gregory, G. Gibson, G. Leuchs, and M. J. Padgett, "Near single-photon imaging in the shortwave infrared using homodyne detection," Proceedings of the National Academy of Sciences **120**, e2216678120 (2023).

[46] O. Wolley, T. Gregory, S. P. Mekhail, R. Archibald, and M. J. Padgett, "Low photon-number stand-off speckle holography at kHz frame rates," Optics Continuum **3**, 1732 (2024).

[47] E. Pearce, O. Wolley, S. P. Mekhail, T. Gregory, N. R. Gemmell, R. F. Oulton, A. S. Clark, C. C. Phillips, and M. J. Padgett, "Single-frame transmission and phase imaging using off-axis holography with undetected photons," Scientific Reports **14**, 16008 (2024).

[48] T. B. Pittman, Y. H. Shih, D. V. Strekalov, and A. V. Sergienko, "Optical imaging by means of two-photon quantum entanglement," Physical Review A **52**, R3429–R3432 (1995).

[49] D. V. Strekalov, A. V. Sergienko, D. N. Klyshko, and Y. H. Shih, "Observation of Two-Photon "Ghost" Interference and Diffraction," Physical Review Letters **74**, 3600–3603 (1995).

[50] T. B. Pittman, D. V. Strekalov, D. N. Klyshko, M. H. Rubin, A. V. Sergienko, and Y. H. Shih, "Two-photon geometric optics," Physical Review A **53**, 2804–2815 (1996).

[51] D. N. Klyshko, "A simple method of preparing pure states of an optical field, of implementing the Einstein–Podolsky–Rosen experiment, and of demonstrating the complementarity principle," Soviet Physics Uspekhi **31**, 74–85 (1988).

[52] R. S. Aspden, D. S. Tasca, R. W. Boyd, and M. J. Padgett, "EPR-based ghost imaging using a single-photon-sensitive camera," New Journal of Physics **15**, 073032 (2013).

[53] P. A. Morris, R. S. Aspden, J. E. C. Bell, R. W. Boyd, and M. J. Padgett, "Imaging with a small number of photons," Nature Communications **6**, 5913 (2015).

[54] P.-A. Moreau, E. Toninelli, T. Gregory, and M. J. Padgett, "Ghost Imaging Using Optical Correlations," Laser & Photonics Reviews p. 1700143 (2017).

[55] A. F. Abouraddy, B. E. A. Saleh, A. V. Sergienko, and M. C. Teich, "Role of Entanglement in Two-Photon Imaging," Physical Review Letters **87**, 123602 (2001).

[56] R. S. Bennink, S. J. Bentley, and R. W. Boyd, ""Two-photon" coincidence imaging with a classical source," Physical review letters **89**, 113601 (2002).

[57] A. Gatti, E. Brambilla, M. Bache, and L. A. Lugiato, "Ghost imaging with thermal light: Comparing entanglement and classicalcorrelation," Physical review letters **93**, 093602 (2004).

[58] A. Gatti, E. Brambilla, M. Bache, and L. A. Lugiato, "Correlated imaging, quantum and classical," Physical Review A **70**, 013802 (2004).

[59] R. S. Aspden, N. R. Gemmell, P. A. Morris, D. S. Tasca, L. Mertens, M. G. Tanner, R. A. Kirkwood, A. Ruggeri, A. Tosi, R. W. Boyd, G. S. Buller, R. H. Hadfield, and M. J. Padgett, "Photon-sparse microscopy: Visible light imaging using infrared illumination," Optica **2**, 1049–1052 (2015).

[60] J. Cheng and S. Han, "Incoherent Coincidence Imaging and Its Applicability in X-ray Diffraction," Physical Review Letters **92**, 093903 (2004).

[61] D. Pelliccia, A. Rack, M. Scheel, V. Cantelli, and D. M. Paganin, "Experimental x-ray ghost imaging," Physical Review Letters **117**, 113902 (2016).

[62] H. Yu, R. Lu, S. Han, H. Xie, G. Du, T. Xiao, and D. Zhu, "Fourier-transform ghost imaging with hard X rays," Physical Review Letters **117**, 113901 (2016).

[63] V. V. Kornienko, S. A. Savinov, Y. A. Mityagin, and G. K. Kitaeva, "Terahertz continuous wave nonlinear-optical detection without phase-locking between a source and the detector," Optics Letters **41**, 4075–4078 (2016).

[64] M. Kutas, B. Haase, P. Bickert, F. Riexinger, D. Molter, and G. von Freymann, "Terahertz quantum sensing," Science Advances **6**, eaaz8065 (2020).

[65] E. Jakeman and J. Walker, "Analysis of a method for the generation of light with sub-poissonian photon statistics," Optics Communications **55**, 219–222 (1985).

[66] E. Jakeman and J. Jefferson, "Antibunching and Sub-poissonian Statistics in Photoelectron-triggered Optical Dead-time Experiments," Optica Acta: International Journal of Optics **33**, 557–576 (1986).

[67] E. Jakeman and J. Rarity, "The use of pair production processes to reduce quantum noise in transmission measurements," Optics Communications **59**, 219–223 (1986).

[68] A. Heidmann, R. J. Horowicz, S. Reynaud, E. Giacobino, C. Fabre, and G. Camy, "Observation of quantum noise reduction on twin laser beams," Physical review letters **59**, 2555 (1987).

[69] J. Rarity, P. Tapster, and E. Jakeman, "Observation of sub-poissonian light in parametric downconversion," Optics Communications **62**, 201–206 (1987).

[70] E. Brambilla, L. Caspani, O. Jedrkiewicz, LA. Lugiato, and A. Gatti, "High-sensitivity imaging with multi-mode twin beams," Physical Review A **77**, 053807 (2008).

[71] G. Brida, M. Genovese, A. Meda, and I. R. Berchera, "Experimental quantum imaging exploiting multimode spatial correlation of twin beams," Physical Review A **83**, 033811 (2011).

[72] N. Samantaray, I. Ruo-Berchera, A. Meda, and M. Genovese, "Realization of the first sub-shot-noise wide field microscope," Light: Science & Applications **6**, e17005–e17005 (2017).

[73] P.-A. Moreau, J. Sabines-Chesterking, R. Whittaker, S. K. Joshi, P. M. Birchall, A. McMillan, J. G. Rarity, and J. C. F. Matthews, "Demonstrating an absolute quantum advantage in direct absorption measurement," Scientific Reports **7** (2017).

[74] E. Losero, I. Ruo-Berchera, A. Meda, A. Avella, and M. Genovese, "Unbiased estimation of an optical loss at the ultimate quantum limit with twin-beams," arXiv preprint arXiv:1710.09307 (2017).

[75] P. W. Shor, "Scheme for reducing decoherence in quantum computer memory," Physical Review A **52**, R2493–R2496 (1995).

[76] W.-Y. Hwang, "Quantum Key Distribution with High Loss: Toward Global Secure Communication," Physical Review Letters **91**, 057901 (2003).

[77] S. Lloyd, "Enhanced sensitivity of photodetection via quantum illumination," Science **321**, 1463–1465 (2008).

[78] S.-H. Tan, B. I. Erkmen, V. Giovannetti, S. Guha, S. Lloyd, L. Maccone, S. Pirandola, and J. H. Shapiro, "Quantum Illumination with Gaussian States," Physical Review Letters **101** (2008).

[79] J. H. Shapiro and S. Lloyd, "Quantum illumination versus coherent-state target detection," New Journal of Physics **11**, 063045 (2009).

[80] S. Barzanjeh, S. Guha, C. Weedbrook, D. Vitali, J. H. Shapiro, and S. Pirandola, "Microwave quantum illumination," Physical review letters **114**, 080503 (2015).

[81] C. W. S. Chang, A. M. Vadiraj, J. Bourassa, B. Balaji, and C. M. Wilson, "Quantum-enhanced noise radar," Applied Physics Letters **114**, 112601 (2019).

[82] E. D. Lopaeva, I. R. Berchera, I. P. Degiovanni, S. Olivares, G. Brida, and M. Genovese, "Experimental realisation of quantum illumination," Physical Review Letters **110** (2013).

[83] E. D. Lopaeva, I. Ruo Berchera, S. Olivares, G. Brida, I. P. Degiovanni, and M. Genovese, "A detailed description of the experimental realization of a quantum illumination protocol," Physica Scripta **T160**, 014026 (2014).

[84] D. G. England, B. Balaji, and B. J. Sussman, "Quantum-enhanced standoff detection using correlated photon pairs," Physical Review A **99**, 023828 (2019).

[85] T. Gregory, P.-A. Moreau, E. Toninelli, and M. J. Padgett, "Imaging through noise with quantum illumination," Science Advances **6**, eaay2652 (2020).

[86] E. Abbe, "Beiträge zur Theorie des Mikroskops und der mikrosk. Wahrnehmung," Archiv für Mikroskopische Anatomie **9**, 413–468 (1873).

[87] Rayleigh, "XV. *On the theory of optical images, with special reference to the microscope*," The London, Edinburgh, and Dublin Philosophical Magazine and Journal of Science **42**, 167–195 (1896).

[88] M. Lelek, M. T. Gyparaki, G. Beliu, F. Schueder, J. Griffié, S. Manley, R. Jungmann, M. Sauer, M. Lakadamyali, and C. Zimmer, "Single-molecule localization microscopy," Nature Reviews Methods Primers **1**, 1–27 (2021).

[89] V. Giovannetti, S. Lloyd, L. Maccone, and J. H. Shapiro, "Sub-Rayleigh-diffraction-bound quantum imaging," Physical Review A **79** (2009).

[90] E. Toninelli, T. Gregory, P.-A. Moreau, and M. J. Padgett, "Beating classical imaging limits with entangled photons," in *Optical, Opto-Atomic, and Entanglement-Enhanced Precision Metrology,* S. M. Shahriar and J. Scheuer, eds. (SPIE, San Francisco, United States, 2019), p. 59.

[91] A. N. Boto, P. Kok, D. S. Abrams, S. L. Braunstein, C. P. Williams, and J. P. Dowling, "Quantum Interferometric Optical Lithography: Exploiting Entanglement to Beat the Diffraction Limit," Physical Review Letters **85**, 2733–2736 (2000).

[92] M. D'Angelo, M. V. Chekhova, and Y. Shih, "Two-Photon Diffraction and Quantum Lithography," Physical Review Letters **87**, 013602 (2001).

[93] H. J. Chang, H. Shin, M. N. O'Sullivan-Hale, and R. W. Boyd, "Implementation of sub-Rayleigh-resolution lithography using an N -photon absorber," Journal of Modern Optics **53**, 2271–2277 (2006).

[94] M. Unternährer, B. Bessire, L. Gasparini, M. Perenzoni, and A. Stefanov, "Super-resolution quantum imaging at the Heisenberg limit," Optica **5**, 1150 (2018).

[95] H. Defienne, P. Cameron, B. Ndagano, A. Lyons, M. Reichert, J. Zhao, A. R. Harvey, E. Charbon, J. W. Fleischer, and D. Faccio, "Pixel super-resolution with spatially entangled photons," Nature Communications **13**, 3566 (2022).

[96] Z. He, Y. Zhang, X. Tong, L. Li, and L. V. Wang, "Quantum microscopy of cells at the Heisenberg limit," Nature Communications **14**, 2441 (2023).

[97] P. Cameron, B. Courme, C. Vernière, R. Pandya, D. Faccio, and H. Defienne, "Adaptive optical imaging with entangled photons," Science **383**, 1142–1148 (2024).

[98] N. P. Mauranyapin, L. S. Madsen, M. A. Taylor, M. Waleed, and W. P. Bowen, "Evanescent single-molecule biosensing with quantum-limited precision," Nature Photonics **11**, 477–481 (2017).

[99] C. A. Casacio, L. S. Madsen, A. Terrasson, M. Waleed, K. Barnscheidt, B. Hage, M. A. Taylor, and W. P. Bowen, "Quantum-enhanced nonlinear microscopy," Nature **594**, 201–206 (2021).

[100] F. Madonini, F. Severini, F. Zappa, and F. Villa, "Single Photon Avalanche Diode Arrays for Quantum Imaging and Microscopy," Advanced Quantum Technologies **4**, 2100005 (2021).

[101] F. Severini, I. Cusini, F. Madonini, D. Brescia, R. Camphausen, Á. Cuevas, S. Tisa, and F. Villa, "Spatially Resolved Event-Driven 24 $\times$ 24 Pixels SPAD Imager With 100% Duty Cycle for Low Optical Power Quantum Entanglement Detection," IEEE Journal of Solid-State Circuits **58**, 2278–2287 (2023).

[102] A. Joobeur, B. E. Saleh, and M. C. Teich, "Spatiotemporal coherence properties of entangled light beams generated by parametric down-conversion," Physical Review A **50**, 3349 (1994).

[103] J. C. Howell, R. S. Bennink, S. J. Bentley, and R. W. Boyd, "Realization of the Einstein-Podolsky-Rosen Paradox Using Momentum- and Position-Entangled Photons from Spontaneous Parametric Down Conversion," Phys. Rev. Lett. **92**, 210403 (2004).

[104] H. Di Lorenzo Pires, C. H. Monken, and M. P. van Exter, "Direct measurement of transverse-mode entanglement in two-photon states," Physical Review A **80**, 022307 (2009).

[105] D. S. Tasca, S. P. Walborn, P. H. Souto Ribeiro, F. Toscano, and P. Pellat-Finet, "Propagation of transverse intensity correlations of a two-photon state," Physical Review A **79**, 033801 (2009).

[106] E. Toninelli, P.-A. Moreau, T. Gregory, and M. J. Padgett, "A model for the detection of spatially correlated biphotons using a photon-counting camera," arXiv:1911.10562 [physics, physics:quant-ph] (2019).

[107] M. Edgar, D. Tasca, F. Izdebski, R. Warburton, J. Leach, M. Agnew, G. Buller, R. Boyd, and M. Padgett, "Imaging high-dimensional spatial entanglement with a camera," Nature Communications **3**, 984 (2012).

[108] E. Brambilla, A. Gatti, M. Bache, and L. A. Lugiato, "Simultaneous near-field and far-field spatial quantum correlations in the high-gain regime of parametric down-conversion," Physical Review A **69**, 023802 (2004).

[109] D. S. Tasca, M. P. Edgar, F. Izdebski, G. S. Buller, and M. J. Padgett, "Optimizing the use of detector arrays for measuring intensity correlations of photon pairs," Physical Review A **88** (2013).

[110] P.-A. Moreau, E. Toninelli, T. Gregory, and M. J. Padgett, "Ghost Imaging Using Optical Correlations," Laser & Photonics Reviews **12**, 1700143 (2018).

[111] D. C. Burnham and D. L. Weinberg, "Observation of Simultaneity in Parametric Production of Optical Photon Pairs," Phys. Rev. Lett. **25**, 84–87 (1970).

[112] A. A. Malygin, A. N. Penin, and A. V. Sergienko, "Spatiotemporal grouping of photons in spontaneous parametric scattering of light," Sov. Phys. Dokl. **30**, 227–229 (1985).

[113] O. Jedrkiewicz, E. Brambilla, M. Bache, A. Gatti, L. A. Lugiato, and P. D. Trapani, "Quantum spatial correlations in high-gain parametric down-conversion measured by means of a CCD camera," Journal of Modern Optics **53**, 575–595 (2006).

[114] F. Devaux, A. Mosset, F. Bassignot, and E. Lantz, "Quantum holography with biphotons of high Schmidt number," Physical Review A **99**, 033854 (2019).

[115] P. Jerram, P. J. Pool, R. Bell, D. J. Burt, S. Bowring, S. Spencer, M. Hazelwood, I. Moody, N. Catlett, and P. S. Heyes, "The LLCCD: Low-light imaging without the need for an intensifier," in *Photonics West 2001 - Electronic Imaging,* M. M. Blouke, J. Canosa, and N. Sampat, eds. (San Jose, CA, 2001), p. 178.

[116] M. Robbins and B. Hadwen, "The noise performance of electron multiplying charge-coupled devices," IEEE Transactions on Electron Devices **50**, 1227–1232 (2003).

[117] A. G. Basden, C. A. Haniff, and C. D. Mackay, "Photon Counting Strategies with Low-Light-Level CCDs," Monthly Notices of the Royal Astronomical Society **345**, 985–991 (2003).

[118] E. Lantz, J.-L. Blanchet, L. Furfaro, and F. Devaux, "Multi-imaging and Bayesian estimation for photon counting with EMCCDs," Monthly Notices of the Royal Astronomical Society **386**, 2262–2270 (2008).

[119] E. Toninelli, P.-A. Moreau, T. Gregory, A. Mihalyi, M. Edgar, N. Radwell, and M. Padgett, "Resolution-enhanced quantum imaging by centroid estimation of biphotons," Optica **6**, 347 (2019).

[120] S. Gnatiessoro, A. Mosset, E. Lantz, and F. Devaux, "Imaging Spatial Quantum Correlations through a thin Scattering Medium," OSA Continuum **2**, 3393 (2019).

[121] H. Defienne, J. Zhao, E. Charbon, and D. Faccio, "Quantum illumination imaging with a single-photon avalanche diode camera," arXiv:2007.16037 [physics, physics:quant-ph] (2020).

[122] K. Roberts, O. Wolley, T. Gregory, and M. J. Padgett, "A comparison between the measurement of quantum spatial correlations using qCMOS photon-number resolving and electron multiplying CCD camera technologies," Scientific Reports **14**, 14687 (2024).

[123] D. Gabor, "A New Microscopic Principle," Nature **161**, 777–778 (1948).

[124] E. N. Leith and J. Upatnieks, "Reconstructed Wavefronts and Communication Theory*," JOSA **52**, 1123–1130 (1962).

[125] J. W. Cooley and J. W. Tukey, "An algorithm for the machine calculation of complex Fourier series," Mathematics of Computation **19**, 297–301 (1965).

[126] B. R. Brown and A. W. Lohmann, "Complex Spatial Filtering with Binary Masks," Applied Optics **5**, 967–969 (1966).

[127] J. W. Goodman and R. W. Lawrence, "Digital image formation from electronically detected holograms," Applied Physics Letters **11**, 77–79 (1967).

[128] I. Yamaguchi and T. Zhang, "Phase-shifting digital holography," Optics Letters **22**, 1268–1270 (1997).

[129] D. Gabor, "IV Light and Information††This article is the substance of a Ritchie lecture, delivered by the author on March 2, 1951 at the University of Edinburgh. The contents of the lecture became known to a wider audience through the distribution of a limited number of mimeographed notes, which have since become widely quoted in the literature. The wish has been often expressed that a permanent record of the lecture should be made generally available. We are glad to be able to meet this wish." in *Progress in Optics,* vol. 1 E. Wolf, ed. (Elsevier, 1961), pp. 109–153.

[130] R. Leitgeb, C. Hitzenberger, and A. Fercher, "Performance of fourier domain vs time domain optical coherence tomography," Optics Express **11**, 889 (2003).

[131] M. Gross and M. Atlan, "Digital holography with ultimate sensitivity," Optics Letters **32**, 909–911 (2007).

[132] B. Kemper and G. von Bally, "Digital holographic microscopy for live cell applications and technical inspection," Applied Optics **47**, A52–A61 (2008).

[133] D. Huang, E. A. Swanson, C. P. Lin, J. S. Schuman, W. G. Stinson, W. Chang, M. R. Hee, T. Flotte, K. Gregory, C. A. Puliafito, and J. G. Fujimoto, "Optical Coherence Tomography," Science **254**, 1178–1181 (1991).

[134] F. Verpillat, F. Joud, M. Atlan, and M. Gross, "Digital Holography at Shot Noise Level," Journal of Display Technology **6**, 455–464 (2010).

[135] M. Marim, E. Angelini, J.-C. Olivo-Marin, and M. Atlan, "Off-axis compressed holographic microscopy in low-light conditions," Optics Letters **36**, 79–81 (2011).

[136] S. L. Cuozzo, P. J. Barge, N. Prajapati, N. Bhusal, H. Lee, L. Cohen, I. Novikova, and E. E. Mikhailov, "Low-Light Shadow Imaging Using Quadrature-Noise Detection with a Camera," Advanced Quantum Technologies **5**, 2100147 (2022).

[137] P. J. Barge, Z. Niu, S. L. Cuozzo, E. E. Mikhailov, I. Novikova, H. Lee, and L. Cohen, "Weak thermal state quadrature-noise shadow imaging," Optics Express **30**, 29401–29408 (2022).

[138] A. Ariyawansa, E. J. Figueroa, and T. G. Brown, "Amplitude and phase sorting of orbital angular momentum states at low light levels," Optica **8**, 147–155 (2021).

[139] F. K. Fatemi and G. Beadie, "Rapid complex mode decomposition of vector beams by common path interferometry," Optics Express **21**, 32291–32305 (2013).

[140] D. B. Lindell and G. Wetzstein, "Three-dimensional imaging through scattering media based on confocal diffuse tomography," Nature Communications **11**, 4517 (2020).

[141] A. Gröger, G. Pedrini, D. Claus, I. Alekseenko, F. Gloeckler, and S. Reichelt, "Advantages of holographic imaging through fog," Applied Optics **62**, D68–D76 (2023).

[142] M. Locatelli, E. Pugliese, M. Paturzo, V. Bianco, A. Finizio, A. Pelagotti, P. Poggi, L. Miccio, R. Meucci, and P. Ferraro, "Imaging live humans through smoke and flames using far-infrared digital holography," Optics Express **21**, 5379–5390 (2013).

[143] G. Thekkadath, D. England, and B. Sussman, "Intensity correlation holography for remote phase sensing and 3D imaging," Optics Express **31**, 43574–43582 (2023).

[144] M. Pellizzari, M. Simonutti, J. Degardin, J.-A. Sahel, M. Fink, M. Paques, and M. Atlan, "High speed optical holography of retinal blood flow," Optics Letters **41**, 3503–3506 (2016).

[145] L. Puyo, M. Paques, and M. Atlan, "Reverse contrast laser Doppler holography for lower frame rate retinal and choroidal blood flow imaging," Optics Letters **45**, 4012–4015 (2020).

[146] N. Verrier, M. Atlan, and M. Gross, *Holographic Vibrometry: Full Field Holographic Vibrometry at Ultimate Limits* (2015).

[147] Z. Zalevsky, Y. Beiderman, I. Margalit, S. Gingold, M. Teicher, V. Mico, and J. Garcia, "Simultaneous remote extraction of multiple speech sources and heart beats from secondary speckles pattern," Optics Express **17**, 21566 (2009).

[148] L. Cester, I. Starshynov, Y. Jones, P. Pellicori, J. G. F. Cleland, and D. Faccio, "Remote laser-speckle sensing of heart sounds for health assessment and biometric identification," Biomedical Optics Express **13**, 3743–3750 (2022).

[149] P. Welch, "The use of fast Fourier transform for the estimation of power spectra: A method based on time averaging over short, modified periodograms," IEEE Transactions on Audio and Electroacoustics **15**, 70–73 (1967).

[150] K. H. Wanser, "Fundamental phase noise limit in optical fibres due to temperature fluctuations," Electronics Letters **28**, 53 (1992).

[151] C. K. Hong, Z. Y. Ou, and L. Mandel, "Measurement of subpicosecond time intervals between two photons by interference," Physical Review Letters **59**, 2044–2046 (1987).

[152] Z. Y. Ou, L. J. Wang, and L. Mandel, "Vacuum effects on interference in two-photon down conversion," Physical Review A **40**, 1428–1435 (1989).

[153] X. Y. Zou, L. J. Wang, and L. Mandel, "Induced coherence and indistinguishability in optical interference," Physical review letters **67**, 318 (1991).

[154] L. J. Wang, X. Y. Zou, and L. Mandel, "Induced coherence without induced emission," Physical Review A **44**, 4614 (1991).

[155] G. B. Lemos, V. Borish, G. D. Cole, S. Ramelow, R. Lapkiewicz, and A. Zeilinger, "Quantum Imaging with Undetected Photons," Nature **512**, 409–412 (2014).

[156] I. Kviatkovsky, H. M. Chrzanowski, E. G. Avery, and S. Ramelow, "Microscopy with undetected photons in the mid-infrared," p. 22.

[157] I. Kviatkovsky, H. M. Chrzanowski, and S. Ramelow, "Mid-infrared microscopy via position correlations of undetected photons," Optics Express **30**, 5916–5925 (2022).

[158] A. V. Paterova, H. Yang, C. An, D. A. Kalashnikov, and L. A. Krivitsky, "Tunable optical coherence tomography in the infrared range using visible photons," Quantum Science and Technology **3**, 025008 (2018).

[159] G. J. Machado, G. Frascella, J. P. Torres, and M. V. Chekhova, "Optical coherence tomography with a nonlinear interferometer in the high parametric gain regime," Applied Physics Letters **117**, 094002 (2020).

[160] A. Vanselow, P. Kaufmann, I. Zorin, B. Heise, H. M. Chrzanowski, and S. Ramelow, "Frequency-domain optical coherence tomography with undetected mid-infrared photons," Optica **7**, 1729 (2020).

[161] C. Lindner, S. Wolf, J. Kiessling, and F. Kühnemann, "Fourier transform infrared spectroscopy with visible light," Optics Express **28**, 4426–4432 (2020).

[162] C. Lindner, J. Kunz, S. J. Herr, S. Wolf, J. Kießling, and F. Kühnemann, "Nonlinear interferometer for Fourier-transform mid-infrared gas spectroscopy using near-infrared detection," Optics Express **29**, 4035–4047 (2021).

[163] A. Paterova, H. Yang, C. An, D. Kalashnikov, and L. Krivitsky, "Measurement of infrared optical constants with visible photons," New Journal of Physics **20**, 043015 (2018).

[164] G. Barreto Lemos, M. Lahiri, S. Ramelow, R. Lapkiewicz, and W. N. Plick, "Quantum imaging and metrology with undetected photons: Tutorial," Journal of the Optical Society of America B **39**, 2200 (2022).

[165] N. R. Gemmell, J. Flórez, E. Pearce, O. Czerwinski, C. C. Phillips, R. F. Oulton, and A. S. Clark, "Loss-Compensated and Enhanced Midinfrared Interaction-Free Sensing with Undetected Photons," Physical Review Applied **19**, 054019 (2023).

[166] M. Gilaberte Basset, A. Hochrainer, S. Töpfer, F. Riexinger, P. Bickert, J. R. León-Torres, F. Steinlechner, and M. Gräfe, "Video-Rate Imaging with Undetected Photons," Laser & Photonics Reviews **15**, 2000327 (2021).

[167] B. E. Haase, J. Hennig, M. Kutas, E. Waller, J. Hering, G. von Freymann, and D. Molter, "Phase-quadrature quantum imaging with undetected photons," Optics Express **31**, 143 (2023).

[168] J. Dong, A. C. Cardoso, H. Zhou, J. Zhang, W. Nie, A. S. Clark, and J. G. Rarity, "Methane Sensing via Unbalanced Nonlinear Interferometry using a CMOS Camera," (2024).

[169] A. Hochrainer, M. Lahiri, R. Lapkiewicz, G. B. Lemos, and A. Zeilinger, "Interference fringes controlled by noninterfering photons," Optica **4**, 341–344 (2017).

[170] C. Yang, Z.-Y. Zhou, L.-L. Wang, Y. Li, S.-K. Liu, Z. Ge, X.-C. Zhang, Q. Tang, G.-C. Guo, and B.-S. Shi, "Interference fringes in a nonlinear Michelson interferometer based on spontaneous parametric down-conversion," Optics Express **29**, 32006 (2021).

[171] J. Fuenzalida, A. Hochrainer, G. B. Lemos, M. Lahiri, and A. Zeilinger, "Resolution in Quantum Imaging with Undetected Photons," in *Frontiers in Optics + Laser Science APS/DLS,* (OSA, Washington, DC, 2019), p. JW3A.103.

[172] J. R. León-Torres, F. Krajinić, M. Kumar, M. G. Basset, F. Setzpfandt, V. F. Gili, B. Jelenković, and M. Gräfe, "Off-axis holographic imaging with undetected light," (2024).

[173] B. Javidi, A. Carnicer, A. Anand, G. Barbastathis, W. Chen, P. Ferraro, J. W. Goodman, R. Horisaki, K. Khare, M. Kujawinska, R. A. Leitgeb, P. Marquet, T. Nomura, A. Ozcan, Y. Park, G. Pedrini, P. Picart, J. Rosen, G. Saavedra, N. T. Shaked, A. Stern, E. Tajahuerce, L. Tian, G. Wetzstein, and M. Yamaguchi, "Roadmap on digital holography [Invited]," Optics Express **29**, 35078–35118 (2021).

[174] T. Zeng, Y. Zhu, and E. Y. Lam, "Deep learning for digital holography: A review," Optics Express **29**, 40572 (2021).

[175] V. Petrov, A. Pogoda, V. Sementin, A. Sevryugin, E. Shalymov, D. Venediktov, and V. Venediktov, "Advances in Digital Holographic Interferometry," Journal of Imaging **8**, 196 (2022).

[176] K. Khare, P. T. S. Ali, and J. Joseph, "Single shot high resolution digital holography," Optics Express **21**, 2581–2591 (2013).

[177] N. T. Shaked, V. Micó, M. Trusiak, A. Kuś, and S. K. Mirsky, "Off-axis digital holographic multiplexing for rapid wavefront acquisition and processing," Advances in Optics and Photonics **12**, 556–611 (2020).

[178] L. Kastl, M. Isbach, D. Dirksen, J. Schnekenburger, and B. Kemper, "Quantitative phase imaging for cell culture quality control," Cytometry Part A **91**, 470–481 (2017).

[179] F. Zernike, "The concept of degree of coherence and its application to optical problems," Physica **5**, 785–795 (1938).

[180] "Phase Contrast Microscopy and Darkfield Microscopy," in *Fundamentals of Light Microscopy and Electronic Imaging,* (John Wiley & Sons, Ltd, 2012), chap. 7, pp. 115–133.

[181] R. Oron, N. Davidson, A. A. Friesem, and E. Hasman, "Chapter 6 - Transverse mode shaping and selection in laser resonators," in *Progress in Optics,* vol. 42 of *Progress in Optics* E. Wolf, ed. (Elsevier, 2001), pp. 325–386.

[182] S. Fürhapter, A. Jesacher, S. Bernet, and M. Ritsch-Marte, "Spiral phase contrast imaging in microscopy," Optics Express **13**, 689–694 (2005).

[183] S. Bernet, A. Jesacher, S. Fürhapter, C. Maurer, and M. Ritsch-Marte, "Quantitative imaging of complex samples by spiral phase contrast microscopy," Optics Express **14**, 3792 (2006).

[184] C. Maurer, A. Jesacher, S. Bernet, and M. Ritsch-Marte, "What spatial light modulators can do for optical microscopy," Laser & Photonics Reviews **5**, 81–101 (2011).

[185] C. Maurer, A. Jesacher, S. Fürhapter, S. Bernet, and M. Ritsch-Marte, "Tailoring of arbitrary optical vector beams," New Journal of Physics **9**, 78 (2007).

[186] A. Jesacher, S. Fürhapter, S. Bernet, and M. Ritsch-Marte, "Shadow Effects in Spiral Phase Contrast Microscopy," Physical Review Letters **94**, 233902 (2005).

[187] A. C. Cardoso, L. P. Berruezo, D. F. Ávila, G. B. Lemos, W. M. Pimenta, C. H. Monken, P. L. Saldanha, and S. Pádua, "Classical Imaging with Undetected Light," (2018).

[188] S. Töpfer, S. Tovar, J. R. L. Torres, D. Derr, E. Giese, J. Fuenzalida, and M. Gräfe, "Synthetic Quantum Holography with Undetected Light," (2024).

[189] J. Fuenzalida, A. Hochrainer, G. B. Lemos, E. A. Ortega, R. Lapkiewicz, M. Lahiri, and A. Zeilinger, "Resolution of Quantum Imaging with Undetected Photons," Quantum **6**, 646 (2022).

[190] T. Gregory, P.-A. Moreau, S. Mekhail, O. Wolley, and M. J. Padgett, "Noise rejection through an improved quantum illumination protocol," Scientific Reports **11**, 21841 (2021).

[191] T. Ono, R. Okamoto, and S. Takeuchi, "An entanglement-enhanced microscope," Nature communications **4**, 2426 (2013).

[192] R. Camphausen, Á. Cuevas, L. Duempelmann, R. A. Terborg, E. Wajs, S. Tisa, A. Ruggeri, I. Cusini, F. Steinlechner, and V. Pruneri, "A quantum-enhanced wide-field phase imager," Science Advances **7**, eabj2155 (2021).

[193] L. Puyo, M. Paques, M. Fink, J.-A. Sahel, and M. Atlan, "Choroidal vasculature imaging with laser Doppler holography," Biomedical Optics Express **10**, 995 (2019).

[194] M. Atlan, O. Martinache, Y. Blazy, Z. Bratasz, T. Aubert, M. Paques, S. Bonnin, and V. Vasseur, "Quantitative evaluation of retinal blood flow and arterial resistivity index using Doppler holography." Investigative Ophthalmology & Visual Science **65**, PP0011 (2024).

[195] R. H. Brown and R. Q. Twiss, "Correlation between Photons in two Coherent Beams of Light," Nature **177**, 27–29 (1956).